UNIVERSITÀ
DEGLI STUDI
DI PADOVA


Sede Amministrativa: Università degli Studi di Padova

Dipartimento di Scienze Chimiche


CORSO DI DOTTORATO DI RICERCA IN: Scienza e Ingegneria dei Materiali e delle Nanostrutture
XXXII CICLO

**Improving Silicon Photodetectors NIR Responsivity *via* Hybrid Opto-Plasmonic Resonances**


Tesi redatta con il contributo finanziario della Fondazione Bruno Kessler (FBK)



**Coordinatore:** Ch.mo Prof. Giovanni Mattei
**Supervisore**: Ch.mo Prof. Filippo Romanato
**Co-Supervisore**: Dr. Giovanni Paternoster

**Dottorando**: Andrea Filippi

*To my parents*

# Abstract

During the past twenty years, the photoelectronic industry has grown to incredible proportions, producing devices that have become staples of our every-day life and have completely transformed the way we live. The core technology at the heart of the photoelectronic industry is the “photodetector”. Traditional photodetectors’ performance has dramatically improved after the introduction of nanostructured materials. Among these enhancement materials, plasmonic metal structures are of particular interest due to their peculiar and useful properties, such as optical resonances, high bulk, and surface sensitivities and sub-wavelength light confinement. Plasmonic materials can lead to the development of detectors for novel applications in nano-photonics, biosensing, integrated optics, and lasers. Here, we want to propose an evolution of the common “waveguide detector” design that enables the fabrication of a plasmonic structure, capable of enhancing the absorption efficiency at any desired wavelength, on top of the active area of any kind of traditional semiconductor-based photodetector, including single-photon silicon photomultipliers (SiPMs). Our structure works in a simple tri-layer configuration, metal-dielectric-semiconductor (MIS), by coupling an optical resonance phenomenon with a traditional plasmonic resonance excited on the metal/dielectric interface by means of hole-coupling transmission through an open-slits type of grating. The resulting hybrid opto-plasmonic resonance can drastically enhance the responsivity of a photodetector.

# Riassunto

Durante i passati vent'anni, l'industria fotoelettronica è cresciuta fino a raggiungere proporzioni incredibili, producendo dispositivi che sono progressivamente diventati imprescindibili nella nostra vita di ogni giorno, cambiando il modo in cui viviamo. La tecnologia cardine dell'industria fotoelettronica è il "foto-rivelatore". Le prestazioni dei tradizionali foto-rivelatori sono migliorate drammaticamente a seguito dell'introduzione dei materiali nano-strutturati. Tra questi materiali, le strutture metalliche plasmoniche risultano essere di particolare interesse a causa delle loro peculiarità e delle loro utili proprietà, come, per esempio, la presenza di risonanze ottiche, le elevate sensibilità di "bulk" e di superficie, e la capacità di ottenere un confinamento "sub-wavelength" della luce. I materiali plasmonici possono aprire la strada verso lo sviluppo di rivelatori ottimizzati per innovative applicazioni nel campo della nano-fotonica, del "biosensing", delle ottiche integrate e dei laser. Con questo lavoro, noi vogliamo proporre un'evoluzione del tipico schema di "rivelatore a guida d'onda" che permetta la fabbricazione di una struttura plasmonica, in grado di aumentare l'efficienza d'assorbimento della luce ad una qualsiasi lunghezza d'onda desiderata, al di sopra dell'area attiva di un qualsiasi foto-rivelatore a base di semiconduttore, inclusi i fotomoltiplicatori a singolo fotone in silicio ("SiPMs"). La nostra struttura funziona sulla base di una semplice configurazione a triplo strato, metallo-dielettrico-semiconduttore ("MIS"), in cui si accoppi una risonanza ottica con una tradizionale risonanza plasmonica, eccitata sulla superficie metallo/dielettrico tramite trasmissione straordinaria della luce attraverso le fenditure della griglia metallica. La risonanza ibrida opto-plasmonica così prodotta, è in grado di accrescere enormemente la responsività di un foto-rivelatore.

# Acknowledgments

I would like to thank my supervisor, Prof. Romanato, and the other members of the BioNanoCharacterization Lab for their constant support, mentorship and invaluable scientific conversations. I would like to give special thanks to my colleague and friend Giulia Borile. I would never have made it to the end without you. I would also like to thank Albert Guerrero Barbero, Xavier Borrisè, Francesc Perez-Murano and Miguel Zabala of Institute of Microelectronics of Barcelona – *Centro Nacional de Microelectronica* – for all the nanofabrication support provided through the Transnational Access program of the Horizon2020 project: NFFA – Nanoscience Foundries and Fine Analysis (grant agreement n. 654360 from 1/9/2015 to 31/8/2020). Their help allowed us to define the best process parameters for the realization of the plasmonic arrays. I would like to thank Pierluigi Bellutti for funding my Ph.D. scholarship, Giovanni Paternoster for helping and tutoring me during my times at FBK, and Damiano Giubertoni for his invaluable contribution to the experimental development and characterization of the plasmonic arrays. This project has received funding from the ATTRACT project "PlaSiPM" funded by the EC under grant agreement n. 777222.

I would like to thank Laura Iop and Prof. Gerosa's research group for their help with the label-free analysis and preparation of bovine/porcine tissue samples. A special thanks to Eleonora Dal Sasso: your friendship and our not-always-scientific conversations allowed me to survive the neverending hours at the microscope, trying to analyze an impossibly large number of samples within an unreasonably short amount of time.

Last, but certainly not least, I would like to thank my old friends Otto Climan and Eleonora Calvi Parisetti for their unlimited patience and constant support. Putting up with me for fourteen years definitely deserves a medal.

# Index

**Chapter 1 – Introduction ....................................................................11**

**Chapter 2 – Background Knowledge ......................................................17**

2.1 – PN-junctions ........................................................................................17

2.2 – Photodetectors and Photodiodes .......................................................20

2.3 – Plasmonics Fundamentals ...................................................................29

**Chapter 3 – Simulations ...........................................................................38**

3.1 – Choosing the Right Materials ............................................................38

3.2 – The Physical Nature of the Resonances ...........................................47

3.3 – 3-D Plasmonic Model Extension .......................................................55

**Chapter 4 – Prototype Fabrication Process ..........................................57**

4.1 – Enhancement Structure Fabrication Process ....................................57

4.2 – EBL Nanofabrication ............................................................................62

4.3 – Metal Deposition and Lift-Off ............................................................70

**Chapter 5 – Device Characterization ......................................................73**

5.1 – Electro-Optical Characterization .........................................................73

5.2 – Array Structural Parameters Measurements .....................................80

5.3 – Doped Silicon versus Intrinsic Silicon ................................................84

**Chapter 6 – Nonlinear Optical Detection ..............................................87**

6.1 – Introduction and Setup Description ..................................................87

6.2 – Label-Free Analysis of Biomedical Samples ......................................93

6.3 – Materials and Methods .........................................................................98

**Chapter 7 – Conclusions .........................................................................100**

**Appendix A – Simulations on SOI Substrate ........................................103**

**Bibliography ..............................................................................................107**

# Chapter 1

# Introduction

During the past twenty years, the photoelectronic industry has grown to incredible proportions, producing devices that have become staples of our every-day life and have completely transformed the way we live, for better and for worse. The core technology at the heart of the photoelectronic industry is the "photodetector". Photodetectors can convert light into electrical signals, thus enabling many useful applications for the photoelectronic devices, and recently have been the object of very intense research activity. Developing photodetectors that can achieve a very high detection accuracy in the ultraviolet (10-400 nm), visible (400-760 nm), infrared (760 nm-1 mm) and terahertz (0.1-10 THz) regions is essential for a plethora of industrial, medical and environmental applications[1]. Benefiting from the advancements of the semiconductor industry, photodetectors working inside different spectral ranges have played very important roles as flame sensing, ozone sensing and convert communications devices[2,3], in air and water purification, environmental monitoring, video imaging and night vision[4], in materials identification[5], astronomical studies[6] and even in early detection of small tumors[7,8].

Following Moore's Law, the size of electronic devices has shrunk increasingly during the years, down to a few tens of nanometers. A new class of materials, "nanostructured materials", are emerging in order to try to overcome any limitation and technical difficulty inherently associated with such a small size. Their special properties derive from the clever exploitation of quantum-confinement effects, surface effects, non-linear optical effects and dielectric confinement effects (waveguiding)[9,10]. Moreover, nanostructured metallic (and half-metallic) materials exhibit peculiar optical properties, allowing them to concentrate, bend and manipulate light at sub-wavelength scale[11–13].

Pushed forward by the nanostructured materials, a variety of nanoscale photodetectors have been developed at a remarkable pace[14–18]. However, they still are in an early development stage and require further tuning before being applied to any practical application. On the other hand, even traditional photodetector performance has dramatically improved due to the introduction of nanostructured materials. Opportunely designed "enhanced" photodetectors with increased photoelectric conversion efficiency and optical responsivity are currently being tested for specialized, innovative applications

such as memory devices[19,20], gas detection[21–24] and optical logic gates[25]. Among the enhancement materials, plasmonic metal structures received particular attention due to their interesting and useful properties, such as optical resonances, high bulk, and surface sensitivities and sub-wavelength light confinement. Plasmonic materials can also lead to the development of detectors at least as small as the modern highly integrated electronic elements, opening the door to applications in nano-photonics[26], biosensing[27], integrated optics[28] and lasers[29].

There are several kinds of plasmonic photodetectors, ranging from the simple prims-coupled and grating-coupled detectors to the hole-coupled detectors, the nanoparticles-enhanced or nano-antennas detectors, and the waveguide detectors. The prism-coupled detectors are one of the first studied variations of plasmonic photodetectors, improving with time their geometrical layout from the so-called Kretschmann configuration[30] to the more popular Otto configuration, whose components can be fabricated independently, and the prism directly aligned to the detector in the setup[31–39]. Metal-insulator-metal (MIM)[40] and metal-organic-metal (MOM)[41–43] prism-coupled devices also exist. Prims-coupled detectors suffer from inherent size limitations and a generally complex fabrication process, thus a more compact and easier to produce iteration of coupled plasmonic detector is generally preferred: the grating-coupled detector. Metal gratings can be fabricated on top of a semiconductor layer (Schottky detector)[44–52] or even a commercial photodiode[53] in order to produce a plasmonic photodetector. Furthermore, the simple grating structure can be replaced with a more complex metal nanowires periodic array[54–58]. Hole-coupled detectors are another valid alternative. In this case, instead of a metal grating structure, the key structure is a hole (or a periodic array of holes/slits) on a metal film deposited on top of a semiconductor substrate. The light impinging on the film can be coupled inside the hole/slit and propagate, enhanced, through the metal into the substrate, leading to devices with improved signal-to-noise ratio[59-69]. Nanoparticles-enriched and nano-antennas detectors are a peculiar type of plasmonic photodetector. They exploit the localized resonances excited by light striking the nanoparticles/antennas, generating large near-field enhancements and strong scattering[13,70–79]. Due to their high degree of complexity, both in terms of fabrication and optical properties control and reproducibility, their practical use is currently quite limited, with promising future applications mostly in the photovoltaic field. Finally, in the last macro-category of plasmonic photodetectors, we find the waveguide detectors. These detectors are based on MIM or IMI (dielectric-metal-dielectric) structures designed to support modes that are low-loss but weakly confined (IMI) or highly confined but lossy (MIM)[80–83]. It is also possible to substitute one or both dielectric layers with a semiconductor material, either organic or inorganic

[84–93]. Usually, waveguide detectors exploit enhanced or localized guided modes in order to increase the performance of traditional photodetectors.

**Plasmonic photodetectors**

| | | |
|---|---|---|
| *Prism-coupled* | Kretschmann configuration | *ref.* 30 |
| | Otto configuration | *ref.* 31-39 |
| | Metal-Insulator-Metal (MIM) | *ref.* 40 |
| | Metal-Organic-Metal (MOM) | *ref.* 41-43 |
| *Grating-coupled* | Schottky detector | *ref.* 44-53 |
| | Periodic nanowires | *ref.* 54-58 |
| *Hole-coupled* | Periodic holes/slits | *ref.* 59-69 |
| *Nanoparticles-enriched* | Nanoparticles/nano-antennas | *ref.* 13,70-79 |
| *Waveguide* | Metal-Insulator-Metal (MIM) | *ref.* 80-83 |
| | Metal-Semiconductor-Metal (MSM) | *ref.* 84-93 |

**Table 1:** Summary of the main categories of plasmonic photodetectors.

All the previously described plasmonic detectors, with the sole exception of waveguide photodetectors, can enhance the responsivity of only thin detection layers, due to the strong confinement characteristics of plasmonic fields, limiting their application to specially "tailored" devices, usually very different from most commercially available photodetectors (e.g. silicon photodiodes). This limitation remains true even for typical waveguide detectors since their guiding properties can only be exploited by impinging the light perpendicularly to the multi-layer structure cross-section. Similarly to Zang et al. and their work on single-photon avalanche diodes (SPADs)[94], here, we want to propose an evolution of the common "waveguide detector" design that enables the fabrication of a plasmonic structure, capable of enhancing the absorption efficiency at any desired wavelength, on top of the active area of any kind of traditional semiconductor-based photodetector, potentially including silicon photomultipliers (SiPMs). Unlike Zang grating structure, which requires a double-SOI-substrate in order to efficiently trap the vertically-impinging light at the desired wavelength and enhance the SPAD absorption efficiency (due to a very narrow resonance of a purely optical guided mode), our structure works in a simple tri-layer configuration, metal-dielectric-semiconductor (MIS), by coupling an optical resonance phenomenon known as Rayleigh singularity with a traditional plasmonic resonance excited on the metal/dielectric interface by means of hole-coupling transmission through an open-slits type of grating. The resulting hybrid opto-plasmonic resonance, belonging to the family of Wood's anomalies, can theoretically enhance the responsivity of a device with a 2 μm thick active area up to ten times its original value, at the working wavelength of 950 nm. We

chose to work in the NIR spectral window since silicon (the most used semiconductor in the photodetector industry) has a very poor native absorption efficiency in this range, due to the proximity of its energy gap, and an increase in performance would open the way to a plethora of interesting applications, especially in the automotive industry, with its ever-growing need of improved LIDAR sensors for autonomous cars. Our work, here described, covers all the steps for developing a working prototype of enhanced photodetector based on the standard *Fondazione Bruno Kessler* (FBK) technology platform, our host research insitute and funder of this research project.

Instead of increasing the spectral responsivity, an alternative way to improve the performance of traditional photodetectors, without impacting on their fabrication process or fundamental functioning principles, is to exploit nonlinear optical phenomena that can make previously undetectable structures or materials emit a signal within the operative range of the detectors. This is very useful for applications that require a small number of detectors to simultaneously detect signals at different wavelengths without "mixing" them or being blind to a specific component of the examined sample. One of the most common applications that fall into this category is Optical Fluorescence Microscopy of biomedical samples. Usually, biomedical samples' structures of interest, either cells cultures or whole tissues' sections, must undergo a particular treatment, called "staining", in order to generate a signal (an optical signal) that can be detected by a microscope photodetector (typically photomultiplier tubes, PMTs). This procedure links photochromatic molecules (fluorophores, molecules that emits a light signal once stimulated by an appropriately tuned wavelength) to the target structures to make them detectable. After the staining, the samples can be examined by fluorescence microscopy within a limited amount of time (weeks), before the fluorophores signal degrades, and no other analysis can be performed on them, due to the considerable shift from their original conditions. Furthermore, most commercially available fluorophores have emission spectra that overlap, thus generating light signals that cannot be easily separated by the detectors in case of a multi-staining study. A possible solution to both the previous limitations is the "label-free" approach. In label-free (fluorescence) microscopy, the samples are not stained, but the endogenous fluorescent molecules are exploited, in combination with a few nonlinear optical phenomena, like Harmonic Generation and Wavelength Mixing, in order to see all the structures of interest. We developed a custom-built microscopy setup that is capable of optimizing, separately, both the intrinsic fluorescence and the Harmonic Generation signals within a wide range of excitation wavelengths (800-1200 nm) in order to achieve the best possible "multi-color" imaging conditions on a plethora of biomedical samples, using only four simple commercial PMTs covering the visible and near-UV spectrum.

We report below a short summary of the main arguments that will be discussed:

- **Chapter 2**: Basic knowledge of fundamental physics involved in our project. Brief description of a PN-junction and its electrical properties, the figures-of-merit of a photodetector and how to use them in order to characterize the performance of a device, and some basic concepts of plasmonics, including an overview on surface plasmon polaritons and how to excite them.

- **Chapter 3**: Description of all the simulations and physical considerations that must be done before fabricating our plasmonic device. How to properly choose the right materials for the plasmonic structure in order to maximize the enhancement effect within the constraints of an "integration" approach. A detailed description of the physical nature of the resonances of our system and how their peculiar hybrid essence is the central pillar of the absorption enhancement structure. How to switch from a simple 2-D grating model to a more realistic, and polarization independent, 3-D "nanodots" array, while keeping all the performance enhancement from the traditional 2-D structure.

- **Chapter 4**: Description of the entire fabrication process required in order to obtain a working prototype of our enhanced photodetector. A brief overview on the two main steps of the fabrication process, then the detailed description of the nanofabrication procedure that leads to a patterned polymeric film over the substrate that can be used as a base for the second fabrication step, the Metal Evaporation. How to obtain a prototype device with an Ag nanodots array over a standard photodiode using a combination of vacuum metal deposition and residual polymeric layer stripping.

- **Chapter 5**: Description of the characterization process of our enhanced prototypes. Electro-optical characterization of several different photodiodes with a proven increase in performance with respect to standard silicon diodes. Description of the procedures we used in order to obtain an accurate measurement or estimation of the most important structural parameters of our silver arrays. Finally, the difference between intrinsic silicon and doped silicon

used in real p-i-n diodes and how to properly estimate its dielectric permittivity.

- **Chapter 6**: Presentation of our designed multi-modal microscope. Introduction of a few key concepts for nonlinear optical microscopy and label-free microscopy, and a detailed description of our custom setup. Examination of a plethora of ex vivo samples in order to prove our microscope capabilities and the significant advantages of a multi-modal approach. Description of the materials and methods used during our experiments with the multi-modal microscope.

- **Chapter 7**: Conclusions and future perspectives. Discussion on which direction to follow in order to increase the performance enhancement towards the predicted theoretical limit.

# Chapter 2

# Background Knowledge

In this chapter, we want to provide some basic knowledge on the fundamental physics at the root of our work. In §2.1, we briefly describe what is a PN-junction and its electrical properties, as the base element of our photodetector. Then, in §2.2 we talk about the figures-of-merit of a photodetector and how to use them in order to characterize the general performance of a photodiode. Finally, in §2.3 we introduce some basic concepts of plasmonics, including an overview on surface plasmon polaritons and how to excite them in simple bi- or tri-layer structures.

## 2.1 PN-junctions

PN-junctions are the basic "building-block" of many semiconductor devices and, therefore, are of great importance both in modern applications and throughout the history of the semiconductor industry. The basic theory of the PN-junction was established by Shockley in 1949[95] and extended by Sah, Noyce, Moll and Shockley himself[96,97].

A PN-junction consists of two semiconductors regions with opposite doping (see Figure 2.1): one is acceptor-enriched (p-type), the other is donor-enriched (n-type). If the doped regions are uniformly doped and the transition between them is abrupt, the structure is called an "abrupt" PN-junction.

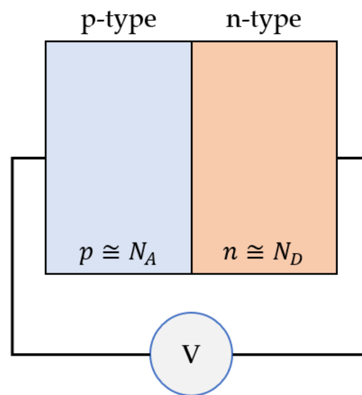


**Figure 2.1:** Schematic representation of a PN-junctions. $p$ and $N_A$ are the hole and acceptor densities inside the p-type semiconductor, $n$ and $N_D$ are the electron and donor densities inside the n-type semiconductor. If the dopants are assumed to be shallow, $p \cong N_A$ and $n \cong N_D$. $V$ is the voltage bias applied to the junction.

However, in practice, one region has usually significantly higher doping than the other: in this case, the junction is called a "one-sided abrupt" PN-junction (commonly denoted as $p^+$-n or $n^+$-p junction). A bias can be applied to a PN-junction: if a positive bias is applied to the p-type semiconductor the junction is "forward-biased", otherwise it's "reverse-biased".

Considering the thermal equilibrium condition (no applied voltage and current flow), the drift and diffusion current of electrons and holes are:

$$J_n = \mu_n n \frac{dE_F}{dx} = 0 \quad ; \quad J_p = \mu_p p \frac{dE_F}{dx} = 0 \tag{2.1}$$

where $\mu_n$ and $\mu_p$ are the electrons and holes mobilities and $E_F$ is the Fermi level energy. In order to satisfy both equations, the derivative must be zero, thus the Fermi level must be constant throughout the sample. The diffusion potential, also known as "built-in" potential, of the junction (for non-degenerate semiconductors) is equal to:

$$\psi_{bi} = \frac{kT}{q} \ln\left(\frac{N_A N_D}{n_i^2}\right) \tag{2.2}$$

where $n_i$ is the intrinsic electrons concentration of the junction. Assuming that the charges distribution inside the junction region (depletion region) has a box profile, knowing that at thermal equilibrium the electric field in the neutral regions (far from the junction) must be zero, the total charge (negative) per unit area in the p-type must be equal to the total charge (positive) per unit area in the n-type:

$$N_A W_{Dp} = N_D W_{Dn} \tag{2.3}$$

where $W_{Dp}$ and $W_{Dn}$ are the p- and n-edge of the depletion region (see Figure 2.2).

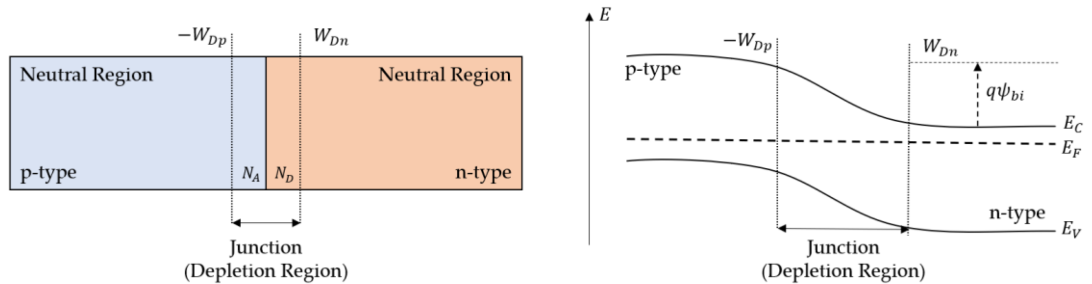


**Figure 2.2:** Extended schematic representation of a PN-junctions (left) and the corresponding energy bands diagram (right). $E_C$ and $E_V$ are the conduction and the valence band, respectively.

Using the Poisson equation[98], it's possible to obtain both the electric field and the potential distribution across the junction:

$$\mathbb{E}(x) = -\frac{qN_A(x + W_{Dp})}{\varepsilon_s} \quad p - type \tag{2.4.1}$$

$$\mathbb{E}(x) = -\frac{qN_D(W_{Dn} - x)}{\varepsilon_s} \quad n - type \tag{2.4.2}$$

$$\psi_i(x) = \frac{qN_A(x + W_{Dp})^2}{2\varepsilon_s} \quad p - type \tag{2.4.3}$$

$$\psi_i(x) = \psi_i(0) + \frac{qN_D\left(W_{Dn} - \frac{x}{2}\right)x}{\varepsilon_s} \quad n - type \tag{2.4.4}$$

where $\mathbb{E}$ is the electric field (in the $x$ direction, across the junction), $q$ is the electron charge and $\varepsilon_s$ is the dielectric function of the semiconductor (p-type or n-type). If the junction is "one-sided abrupt" ($p^+$-n or $n^+$-p), from the "built-in" potential equation and the Poisson equation emerges that most of the potential variation (as well as most of the depletion region) is inside the less doped semiconductor[94]. Therefore, in this case, the low-doped region primarily determines the characteristics of the semiconductor device.

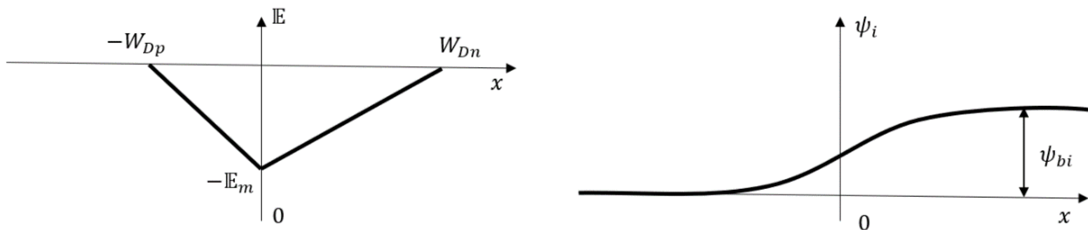


**Figure 2.3:** Electric field distribution (left) and potential distribution (right) of an "abrupt" PN-junction. $\mathbb{E}_m$ is the maximum field that exists at $x = 0$.

Applying a voltage $V$ to a PN-junction changes the total potential variation to $(\psi_{bi} - V)$, where the sign of $V$ is positive if there is a "forward" bias, negative for "reverse" bias, and the depletion region width becomes a function of $V$ (see Figure 2.4).

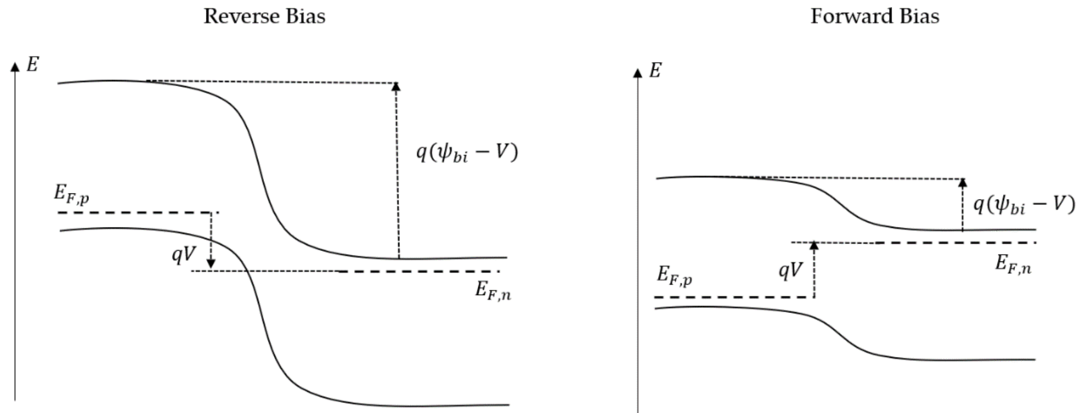


**Figure 2.4:** Energy bands diagram of a PN-junction under "reverse" bias (left) or "forward" bias (right).

The depletion region has a specific capacitance per unit area that is defined as

$$C_D = \frac{dQ_D}{dV} = \frac{\varepsilon_s}{W_D} \tag{2.5}$$

where $Q_D$ is the incremental depletion charge on each side of the junction (the total charge must be zero) upon an incremental change of the applied bias $dV$, and $W_D$ is the depletion region width.

## 2.2 Photodetectors and Photodiodes

Photodetectors are semiconductor devices that can detect optical signals *via* electronic processes. They generally operate following three base steps: (1) carrier generation, (2) carrier transport and/or multiplication (if a gain mechanism is present in the device) and (3) extraction of carriers to provide the output signal. Photodetectors are critical devices for several different applications, ranging from the telecom industry to the cutting-edge biomedical research, and, therefore, require a high-speed response and minimal noise while keeping the biasing voltage and current low, as well as a compact size.

There are many different types of photodetectors, although, they mainly fall into two categories: thermal detectors and photon detectors. Thermal detectors detect light through the rise in temperature of their surface when the light is absorbed and are ideal for far-infrared wavelengths detection. On the other hand, photon detectors can detect light signals due to the photoelectric effect (photocurrent produced by carrier excitation from photons absorption). Silicon photodiodes belong to the photon detectors family, thus, using photons in order to generate a current.

The maximum detectable wavelength (in μm) is given by the following equation:

$$\lambda = \frac{hc}{\Delta E} = \frac{1.24}{\Delta E(in\ eV)} \tag{2.6}$$

where $\Delta E$ is the energy gap of the semiconductor used for the device, which is chosen in order to optimize the detection of the wavelength of interest. In fact, the absorption efficiency of a particular wavelength in a semiconductor is determined by its absorption coefficient $\alpha$: a high value of $\alpha$ means that most of the incident light is absorbed near the surface of the semiconductor, a low value of $\alpha$ means, instead, that light penetrates much longer inside the semiconductor, which can also be transparent to a specific range of wavelengths[98]. Figure 2.5 shows the measured intrinsic absorption coefficients of some of the most commonly used semiconductors.

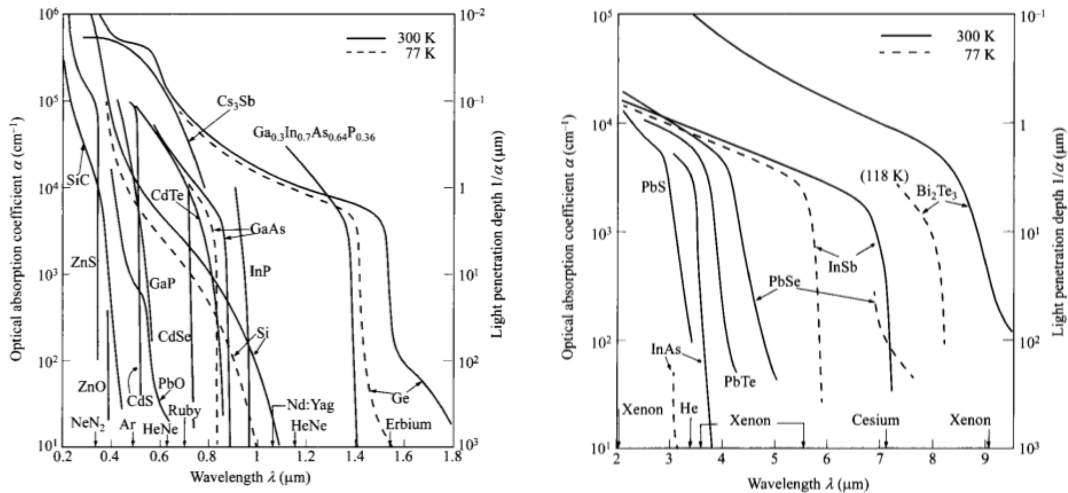


**Figure 2.5:** Measured absorption coefficients of several semiconductors used in the photodetector industry, from visible (left) to infrared (right) light. Solid curves are for 300 K measurements, dashed curves for 77 K. Most of the semiconductors show a red-shift of their absorption coefficients with an increase in temperature. Some IV-VI compounds (e.g. PbSe), however, have bandgaps that increase with the temperature and, thus, decrease their wavelength detection limit. Adapted from "Physics of Semiconductor Devices" (Wiley & Sons, 2006).

The main figure of merit of any photodetector is the quantum efficiency, defined as the number of carriers produced per photon:

$$\eta = \frac{I_{ph}}{q\Phi} = \frac{I_{ph}}{q}\left(\frac{h\nu}{P_{opt}}\right) \tag{2.7}$$

where $I_{ph}$ is the photocurrent, $\Phi$ is the photon flux and $P_{opt}$ is the average incident optical power. Ideally, $\eta = 1$, however, in practice, its always less than the unity due to recombination losses, incomplete absorption, reflections, etc. Another fundamental performance parameter is the responsivity, defined as the ratio between the photocurrent and the incident optical power:

$$\mathcal{R} = \frac{I_{ph}}{P_{opt}} = \frac{\eta q}{h\nu} = \frac{\eta\lambda}{1.24} \tag{2.8}$$

The responsivity increases linearly with the wavelength.

The third important metric of any photodetector is the signal-to-noise ratio (S/N), which is strongly related the sensitivity of the device (a high signal detected, in combination with a low minimum detectable signal strength, translates into a high sensitivity of the photodetector). There are many possible sources of noise, and therefore an increased minimum detectable signal, for a photodetector: dark current, which is the leakage current of a biased photodetector not exposed to a light source, background radiation (e.g. additional light sources, black-body radiation), internal thermal noise, due to the random carriers thermal agitation, shot noise, related to the statistical nature of the discrete single photoelectric events, "flicker" noise (random effects associated with surface traps) and fluctuations in the generation-recombination events. All noise sources are independent of each other and can be simply added together in order to estimate the total noise of a device. The figure of merit associated with the total noise of a photodetector is called noise-equivalent power (NEP)[99] and corresponds to the root mean square of the incident optical power required to produce a $S/N = 1$ inside a 1 Hz bandwidth. From the NEP comes the detectivity of the photodetector:

$$D^* = \frac{\sqrt{AB}}{NEP} \tag{2.9}$$

where $A$ is the detector active area and $B$ is the bandwidth. The detectivity is normalized to the area due to the noise proportionality to the square root of the detector area.

As previously stated, photodiodes belong to the photon detector category. Their peculiar characteristic is a moderate electric field inside the depletion region that allows separating photogenerated electron-hole pairs. The size of the depletion region of a photodiode is directly connected to its operational speed and quantum efficiency: the thinner the depletion region, the higher the speed of the devices and the lower the quantum efficiency (because only a small fraction of the incident light can be absorbed). All photodiodes (except for the special case of the avalanche photodiode, which will not be discussed here) have a maximum gain of one, thus they do not have an internal multiplicative amplification of the signal (see Figure 2.6).

| Photodetector | | Gain | Response time (s) |
|---|---|---|---|
| Photoconductor | | $1–10^6$ | $10^{-8}–10^{-3}$ |
| Photodiodes | *p-n* junction | 1 | $10^{-11}$ |
| | *p-i-n* junction | 1 | $10^{-10}–10^{-8}$ |
| | Metal-semiconductor diode | 1 | $10^{-11}$ |
| CCD | | 1 | $10^{-11}–10^{-4}$* |
| Avalanche photodiode | | $10^2–10^4$ | $10^{-10}$ |
| Phototransistor | | $\approx 10^2$ | $10^{-6}$ |

* Limited by charge transfer. Large integration time is an advantage for CCD for high sensitivity.

**Figure 2.6:** Typical values of internal gain and response time of common photodetectors. As can be seen, all devices falling inside the "photodiodes" category have no internal multiplicative mechanism implemented. Adapted from "Physics of Semiconductor Devices" (Wiley & Sons, 2006).

Figure 2.6 shows that the photodiodes family mainly comprise three types of photodetectors: the simple PN-junction photodiodes, the p-i-n photodiodes, and the metal-semiconductor diodes. A fourth, less common, photodiode is the heterojunction photodiode. Here, we will focus our attention to the PN-junction and p-i-n photodiodes, briefly describing their typical quantum efficiency, response time and device noise (considering a "reverse" bias operational mode, as is common for applications in the visible and near-infrared).

For the basic PN-junction photodiode, the quantum efficiency is simply given by Eq. 2.7 and the responsivity of the device by Eq. 2.8. As previously discussed in §2.2, the maximum detectable wavelength (or long-wavelength cutoff) is determined by the energy gap of the device semiconductor due to the absorption coefficient being extremely small above the gap. The lower limit of the detection range (short-wavelength cutoff), instead, is given by large absorption coefficients ($\geq 10^5\ \mathrm{cm}^{-1}$) that drastically increase the absorption of the incident light near the surface, where recombination phenomena are more common. Therefore, carriers tend to recombine before reaching the depletion region, effectively causing a signal loss.

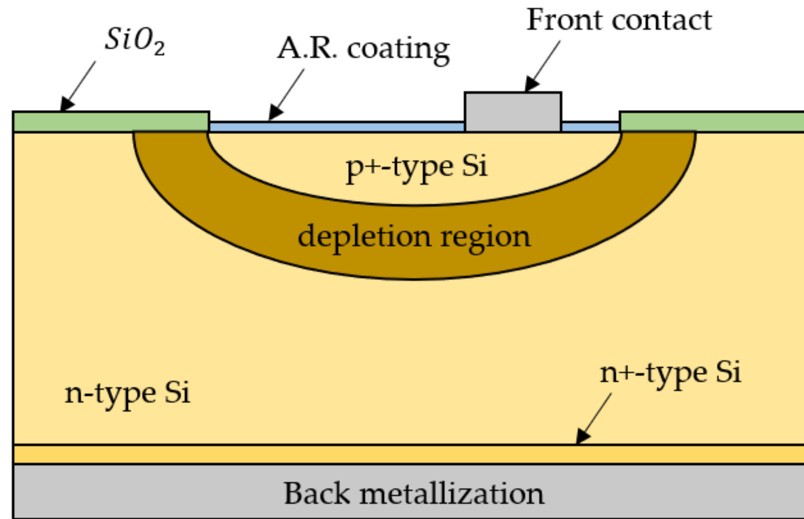


**Figure 2.7:** Schematic representation of a typical Silicon $p^+$-n junction photodiode. The $p^+$-type Si is used as the detector active area (where the incident photons are absorbed and detected) while the $n^+$-type Si thin layer is used as a diffusion layer. The front and back metallization serve as contacts (respectively anode and cathode). The silica on top, typically thermally grown, serves as a passivation/protection layer for the device. The active are is capped with an anti-reflection coating (which can be multi-layered) in order to minimize the reflection losses at the interface.

The response speed of a PN-junction photodiode is limited by the drift time of the carriers inside the depletion region, their diffusion inside the semiconductor (carriers generated outside of the depletion region must travel to it before being detected, thus causing a time delay) and the capacitance of the depletion region. Usually, to maximize the operational speed of a photodiode, the junction is formed near the surface (to minimize the diffusion effect) and the depletion region width is kept around a few micrometers, in order to do not increase the carriers transit-times too much but also to do not have an excessive depletion region capacitance (due to a too thin layer). Most incident light can already be absorbed with a depletion width of $\sim 1/\alpha$.

The device noise of a PN-junction photodiode can be studied considering the generalized photodetection process flow reported in Figure 2.8. An optical signal (and possibly background radiation) is absorbed by the device and electron-hole pairs are generated. These pairs are separated by the electric field and electrons/holes drift to the opposite contacts of the photodiode, producing a photocurrent inside the external load resistor. Considering an intensity-modulated input signal:

$$P(\omega) = P_{opt}[1 + m * \exp(i\omega t)] \tag{2.10}$$

where $m$ is the modulation index and ω the modulation frequency, and an average photocurrent:

$$I_p = q\left(\eta \frac{P_{opt}}{h\nu}\right) \tag{2.11}$$

the root mean square of the signal power is given by:

$$p_{opt} = \frac{mP_{opt}}{\sqrt{2}} \tag{2.12}$$

and the root mean square of the signal current (for an internal gain equal to one) is[98]:

$$i_p = \frac{q\eta mP_{opt}}{\sqrt{2}h\nu} \tag{2.13}$$

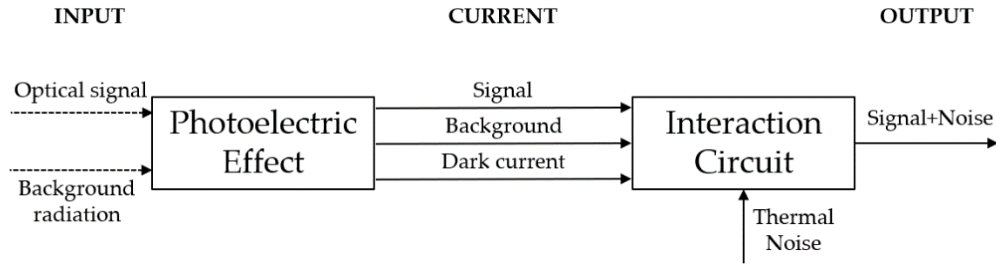


**Figure 2.8:** Diagram of a generalized photodetection process.

All currents inside the photodiode (the photocurrent and the noise-generated currents) are randomly generated and, therefore, contribute to the total shot noise of the device:

$$\langle i_s^2 \rangle = 2q\left(I_p + I_B + I_D\right)B \tag{2.14}$$

where $I_B$ is the current generated by the background radiation, $I_D$ is the dark current and $B$ is the bandwidth. The thermal noise, instead, is given by:

$$\langle i_T^2 \rangle = \frac{4kTB}{R_{eq}} \tag{2.15}$$

where

$$\frac{1}{R_{eq}} = \frac{1}{R_j} + \frac{1}{R_L} + \frac{1}{R_i} \tag{2.16}$$

is the total resistance of the equivalent circuit of a photodiode, given by the junction resistance $R_j$, the eternal load resistor resistance $R_L$ and the input resistance of the amplifier $R_i$ (see Figure 2.9)[100,101].

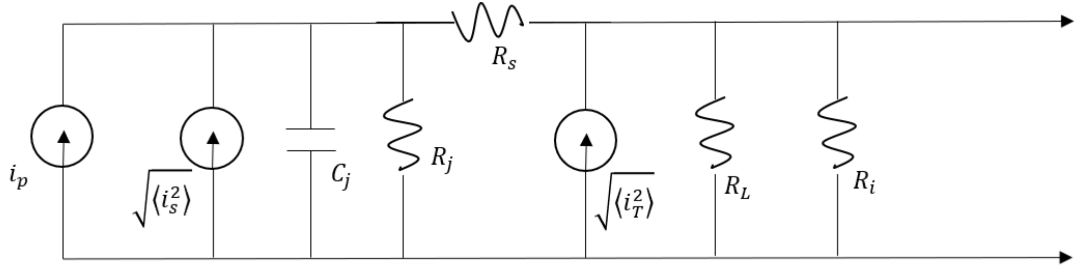


**Figure 2.9:** Diagram of the equivalent circuit of a photodiode. $C_j$ is the junction capacitance and $R_s$ is the series resistance, usually much smaller than the other resistances, thus negligible.

For a completely modulated signal ($m = 1$), the signal-to-noise ratio is[98]

$$\frac{S}{N} = \frac{i_p^2}{\langle i_S^2 \rangle + \langle i_T^2 \rangle} = \frac{(1/2)\left(q\eta P_{opt}/h\nu\right)^2}{2q\left(I_p + I_B + I_D\right)B + 4kTB/R_{eq}} \tag{2.17}$$

The noise-equivalent power is (S/N = 1 , B = 1 Hz)

$$NEP = \left(\frac{h\nu}{\eta}\right)\sqrt{\frac{2\left(I_B + I_D + \frac{2kT}{qR_{eq}}\right)}{q}} \tag{2.18}$$

The previous noise equations show that to increase the sensitivity of a PN-junction photodetector, both the quantum efficiency and the equivalent resistance should be increased, while the background and dark current should be minimized.

A p-i-n photodiode is a special case of PN-junction device where an intrinsic region (i-type) is interposed between the p-type and n-type regions in order to optimize the quantum efficiency and operational speed *via* precise tailoring of the depletion region width. In practice, the i-type region is usually approximated with a highly resistive p-type or n-type layer. P-i-n photodiodes are among the most-used photodetectors across all industry and research fields.

Assuming steady-state conditions and a “reverse” bias operational mode, the total photocurrent density generated by the separation of the electron-hole pairs is[102]

$$J_{tot} = J_{dr} + J_{diff} \tag{2.19}$$

where $J_{dr}$ is the drift contribution to the current, due to carriers generated inside the depletion region, while $J_{diff}$ is the diffusion contribution, due to carriers generated outside the depletion region that diffuse into the junction. If the carriers' thermal generation current is negligible and the p-type layer is much thinner than $1/\alpha$, then the pairs generation rate can be described as:

$$G_e(x) = \Phi_0 \alpha \exp(-\alpha x) = P_{opt} \frac{(1-R)}{Ah\nu} \alpha \exp(-\alpha x) \tag{2.20}$$

where $\Phi_0$ is the incident photon flux per unit area, $R$ is the reflection coefficient, and $A$ is the detector active area.

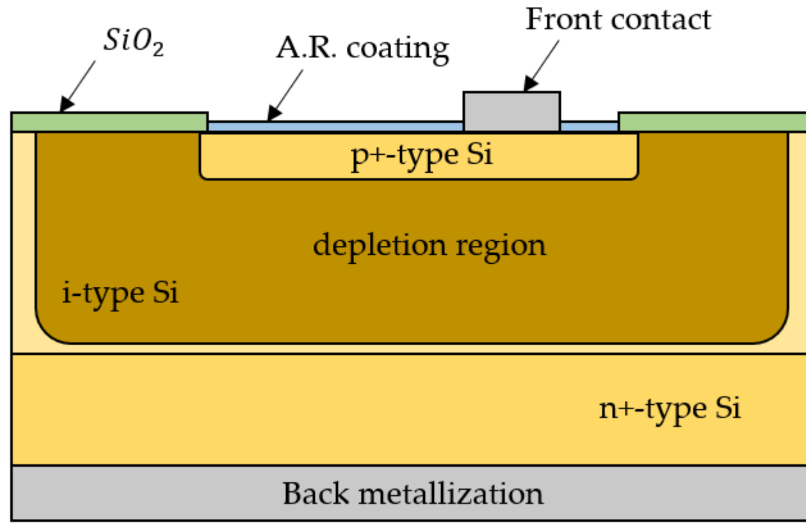


**Figure 2.10:** Schematic representation of a Silicon p-i-n photodiode. The depletion region is entirely inside the intrinsic semiconductor.

From Eq. 2.20, the drift current becomes:

$$J_{dr} = -q \int_0^{W_D} G_e(x) dx = q\Phi_0[1 - \exp(-\alpha W_D)] \tag{2.21}$$

where a quantum efficiency of one is assumed inside the depletion region (of $W_D$ width). Outside of the depletion region, inside the n-type quasi-neutral region, the major current contribution is given by the diffusion current from the minority carriers (holes). The holes density is determined by the diffusion equation (considering only Shockley-Read-Hall recombination):

$$D_p \frac{\partial^2 p_n}{\partial x^2} - \frac{p_n - p_{no}}{\tau_p} + G_e(x) = 0 \tag{2.22}$$

where $D_p$ is the diffusion coefficient of the holes, $\tau_p$ the lifetime of excess carriers, and $p_{no}$ the hole density at equilibrium. Solving Eq. 2.22 imposing $p_n = p_{no}$ for $x = \infty$ and $p_n = 0$ for $x = W_D$, gives:

$$p_n = p_{no} - [p_{no} + C_l \exp(-\alpha W_D)] \exp\left(\frac{W_D - x}{L_p}\right) + C_l \exp(-\alpha x) \qquad (2.23)$$

with

$$C_l = \left(\frac{\Phi_0}{D_p}\right) \frac{\alpha L_p^2}{1 - \alpha^2 L_p^2} \qquad (2.24.1)$$

$$L_p = \sqrt{D_p \tau_p} \qquad (2.24.2)$$

From Eq. 2.22, 2.23, 2.24.1 and 2.24.2, the diffusion current density becomes:

$$J_{diff} = -qD_p \frac{\partial p_n}{dx}\{x = W_D\} = q\Phi_0 \frac{\alpha L_p}{1 + \alpha L_p} \exp(-\alpha W_D) + \frac{q p_{no} D_p}{L_p} \qquad (2.25)$$

The total current density, then, is the sum of Eq. 2.21 and Eq. 2.25:

$$J_{tot} = q\Phi_0 \left[1 - \frac{\exp(-\alpha W_D)}{1 + \alpha L_p}\right] + \frac{q p_{no} D_p}{L_p} \qquad (2.26)$$

Finally, the quantum efficiency of the device can be obtained from Eq. 2.7, 2.20 and 2.26:

$$\eta = \frac{A J_{tot}/q}{P_{opt}/h\nu} = (1 - R)\left[1 - \frac{\exp(-\alpha W_D)}{1 + \alpha L_p}\right] \qquad (2.27)$$

In order to increase the efficiency of a p-i-n (or PN-junction) photodiode, the reflections must be minimized, as well as the percentage of light absorbed out of the depletion region (diffusion contribution). Furthermore, while it is desirable to have $\alpha W_D \gg 1$, it must be kept in mind that this condition tends to increase the transit-delay time, thus decreasing the operational speed of the device. Eq. 2.27 is strictly valid only for a photodiode with negligible depletion region recombination and surface recombination, however, in many cases, these approximations don't properly describe the behavior of real devices, in which these kinds of phenomena are often predominant. In general, p-i-n photodiodes are faster and more efficient than PN-photodiodes, mainly due to the increased width of the depletion region (see Figure 2.7 and Figure 2.10), which minimizes out-of-region light absorption losses and the carriers diffusion contribution (much slower than the drift process). However, since p-i-n diodes have an i-type region that increases the series resistance in the

equivalent circuit (see Figure 2.9), they show a slightly higher level of noise with respect to the PN-junction diodes.

## 2.3 Plasmonics Fundamentals

Surface Plasmon Polaritons (SPPs) are electromagnetic surface waves that propagate at the interface between a dielectric and a conductor and are strictly confined in the perpendicular direction. SPPs arise from the constructive interaction between an electromagnetic field and the collective electron oscillations (electron plasma oscillations) of a conductor. To understand the nature of SPPs and their fundamental characteristics, the starting point is to apply Maxwell's equations[103] to a flat interface between a dielectric and conductor materials. If there are no external charge or current density, the equations yield:

$$\nabla \times \nabla \times \mathbb{E} = -\mu_0 \frac{\partial^2 \mathbb{D}}{\partial t^2} \tag{2.28}$$

where $\mu_0$ is the vacuum permeability and $\mathbb{D}$ the displacement field. Eq. 2.28 can be rewritten as[103]:

$$\nabla\left(-\frac{1}{\varepsilon}\mathbb{E} \cdot \nabla\varepsilon\right) - \nabla^2\mathbb{E} = -\mu_0 \varepsilon_0 \varepsilon \frac{\partial^2 \mathbb{E}}{\partial t^2} \tag{2.29}$$

where $\varepsilon$ and $\varepsilon_0$ are the dielectric permittivity of the medium and the vacuum dielectric constant. For negligible changes in the dielectric profile over distances in the order of one optical wavelength, Eq. 2.29 simplifies to the so called "wave equation":

$$\nabla^2\mathbb{E} - \frac{\varepsilon}{c^2}\frac{\partial^2 \mathbb{E}}{\partial t^2} = 0 \tag{2.30}$$

where $c$ is the speed of light constant. If the electric field evolves in time with a harmonic profile, Eq. 2.30 becomes the "Helmholtz equation":

$$\nabla^2\mathbb{E} + k_0^2 \varepsilon \mathbb{E} = 0 \tag{2.31}$$

where $k_0$ is the wave vector of the propagating wave, equal to $\omega/c = 2\pi/\lambda$. Considering a one-dimensional propagation geometry (see Figure 2.11), the "Helmholtz equation" becomes:

$$\frac{\partial^2 \mathbb{E}}{\partial z^2} + (k_0^2\varepsilon - \beta^2)\mathbb{E} = 0 \tag{2.32}$$

where $\beta = k_x$ is the propagation constant of the wave. An analogous equation can be found for the magnetic field $\mathbb{H}$.

In order to study the spatial profile and dispersion trend of a propagating wave at the interface, it is necessary to find the explicit equations for the field components of both the electric and magnetic fields.

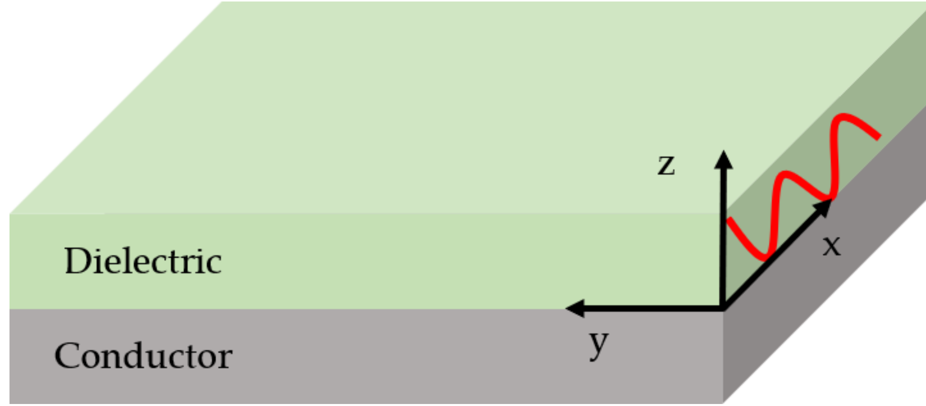


**Figure 2.11:** Schematic representation of a one-dimensional propagation geometry at the interface between a dielectric and a conductor. The wave (red curve) propagates along the x-axis and no spatial variation is present along the perpendicular y-axis. $z = 0$ is set at the interface between the two materials.

These equations can be found *via* Maxwell's equations[103], considering a harmonic time dependence of the wave a one-dimensional propagation geometry (as previously done):

$$\frac{\partial E_y}{\partial z} = -i\omega\mu_0 H_x \tag{2.33.1}$$

$$\frac{\partial E_x}{\partial z} - i\beta E_z = i\omega\mu_0 H_y \tag{2.33.2}$$

$$i\beta E_y = i\omega\mu_0 H_z \tag{2.33.3}$$

$$\frac{\partial H_y}{\partial z} = i\omega\varepsilon_0\varepsilon E_x \tag{2.33.4}$$

$$\frac{\partial H_x}{\partial z} - i\beta H_z = -i\omega\varepsilon_0\varepsilon E_y \tag{2.33.5}$$

$$i\beta H_y = -i\omega\varepsilon_0\varepsilon E_z \tag{2.33.6}$$

Two sets of solutions can be found for the previous equations, one set for each type of polarization that the propagating waves can possess. The first set, associated with a polarization state that leaves only the $E_x$, $E_z$ and $H_z$ field

components nonzero, comprises the Transverse Magnetic (TM) modes, while the other set, leaving the $H_x$, $H_z$ and $E_z$ field components nonzero, comprises the Transverse Electric (TE) modes. TM modes are governed by the following equations:

$$\frac{\partial^2 H_y}{\partial z^2} + (k_0^2\varepsilon - \beta^2)H_y = 0 \tag{2.34.1}$$

$$E_x = -i\frac{1}{\omega\varepsilon_0\varepsilon}\frac{\partial H_y}{\partial z} \tag{2.34.2}$$

$$E_z = -\frac{\beta}{\omega\varepsilon_0\varepsilon}H_y \tag{2.34.3}$$

TE modes follow these equations, instead:

$$\frac{\partial^2 E_y}{\partial z^2} + (k_0^2\varepsilon - \beta^2)E_y = 0 \tag{2.35.1}$$

$$H_x = i\frac{1}{\omega\mu_0}\frac{\partial E_y}{\partial z} \tag{2.35.2}$$

$$H_z = \frac{\beta}{\omega\mu_0}E_y \tag{2.35.3}$$

The simplest geometry that can sustain SPPs is a single interface between a non-absorbing dielectric and a metal (see Figure 2.12).

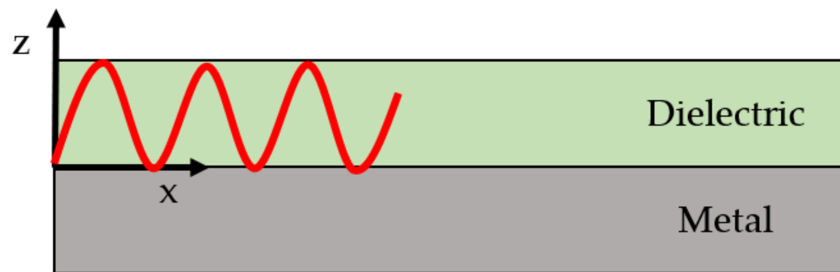


**Figure 2.12:** Schematic representation of the simplest geometry that can support SPPs: a flat interface between a dielectric and a metal.

Solving the TM modes equations for both the half-spaces ($z > 0$ dielectric, $z < 0$ metal) leads to:

$$H_y(z) = A_d \exp(i\beta x)\exp(-k_d z) \tag{2.36.1}$$

$$E_x(z) = -iA_d \frac{1}{\omega\varepsilon_0\varepsilon_d} k_d \exp(i\beta x)\exp(-k_d z) \quad (2.36.2)$$

$$E_z(z) = -A_m \frac{\beta}{\omega\varepsilon_0\varepsilon_d} \exp(i\beta x)\exp(-k_d z) \quad (2.36.3)$$

for $z > 0$, and:

$$H_y(z) = A_m \exp(i\beta x)\exp(k_m z) \quad (2.37.1)$$

$$E_x(z) = -iA_m \frac{1}{\omega\varepsilon_0\varepsilon_m} k_m \exp(i\beta x)\exp(k_m z) \quad (2.37.2)$$

$$E_z(z) = -A_m \frac{\beta}{\omega\varepsilon_0\varepsilon_m} \exp(i\beta x)\exp(k_m z) \quad (2.37.3)$$

for $z < 0$. $A_m$ and $A_d$ are the areas of the metal and dielectric, $\varepsilon_m$ and $\varepsilon_d$ are their dielectric functions, $k_m$ and $k_d$ are the components of the wave vector of the propagating wave perpendicular to the interface, considered into the two media. The reciprocal values of the perpendicular components give the evanescent decay length of the wave field inside the two materials and quantifies its confinement. Continuity conditions of the fields across the interface requires that $A_m = A_d$ and

$$\frac{k_d}{k_m} = -\frac{\varepsilon_d}{\varepsilon_m} \quad (2.38)$$

If $\varepsilon_d > 0$ (most of the cases), Eq. 2.38 is satisfied only when $Re[\varepsilon_m] < 0$. Therefore, the surface wave can only exist at the interface between to material with dielectric functions of the opposite sign (a conductor and a dielectric, precisely). For a metal, $Re[\varepsilon_m] < 0$ is a condition that is satisfied for frequencies below the bulk plasmon frequency $\omega_p$[103]. The expression for $H_y$ must also satisfy the "wave equation" in Eq. 2.34.1, leading to:

$$k_m^2 = \beta^2 - k_0^2\varepsilon_m \quad (2.39.1)$$

$$k_d^2 = \beta^2 - k_0^2\varepsilon_d \quad (2.39.2)$$

Combining these two equations with Eq. 2.38 yield the dispersion relation of SPPs on flat interfaces in a bi-layer geometry:

$$\beta = k_0\sqrt{\frac{\varepsilon_m\varepsilon_d}{\varepsilon_m + \varepsilon_d}} \quad (2.40)$$

The same procedure can also be applied to the TE modes of propagation, however, in this case, it is found that it is not possible to satisfy the continuity conditions of the fields at the interface, and, thus, no SPPs are supported by TE modes[103].

Figure 2.13 shows an example of a dispersion relation profile of an SPP propagating at the interface between a metal with negligible absorption (its dielectric function is entirely real) and air or silica. Due to its bound nature, the SPP for both interfaces always lies at greater wave vectors than the corresponding light lines, approaching them asymptotically. This means that specific wave vector-matching techniques are necessary in order to excite an SPP using, for example, a light beam. The most common approaches for exciting an SPP will be briefly discussed in a later paragraph.

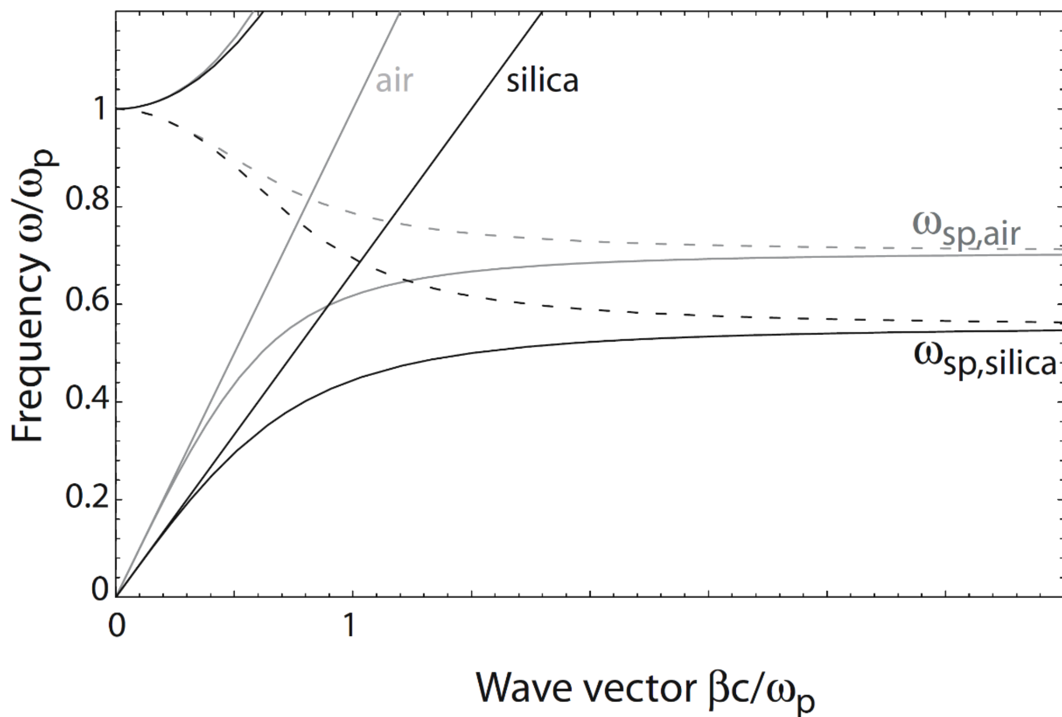


**Figure 2.13:** Dispersion relation of SPPs propagating at the interface between an ideal metal and air (grey curves) or silica (black curves). The axes' scales are normalized to the bulk plasma frequency of the metal. The plot shows both real (continuous curves) and imaginary (dashed curves) parts of the wave vector $\beta$. Adapted from "Plasmonics: Fundamentals and applications" (Springer, 2007).

In real metals, free-electron and inter-band damping are non-negligible, therefore the dielectric function is complex. A complex $\varepsilon_m$ means that the SPPs are damped while propagating, with a finite propagation length $L = (2Im[\beta])^{-1}$ typically of the order of 10-100 μm (in the visible and near-infrared range). Limiting the propagation length implies that both the supported

wavelengths and the amount of confinement along the z-axis are being limited. A "quasibound" leaky mode of propagation is now allowed, in contrast to the ideal metal case. A typical trade-off of real SPPs is that between localization and energy losses: the better the confinement, the more losses the SPPs suffer (the shorter their propagation length).

Increasing the complexity of the system geometry increases the number of supported SPPs. If we consider a metal slab immersed in a dielectric environment (a tri-layer system), we can support up to two SPPs, one for each interface (see Figure 2.14). It has also been demonstrated that if the thickness of the metal slab is of the order of the SPPs penetration depth, the plasmons wave can also strongly interact with each other[104–107].

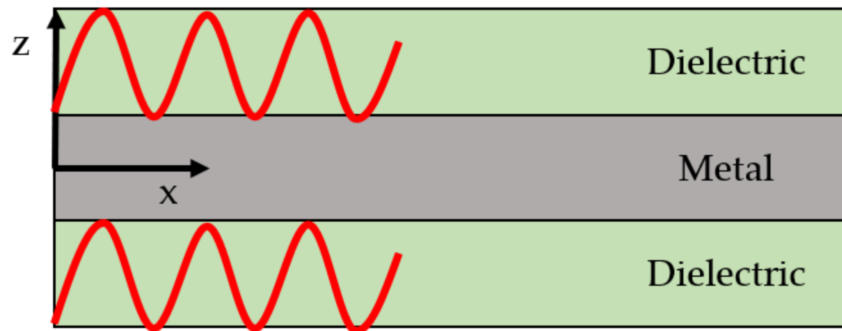


**Figure 2.14:** Schematic representation of a tri-layer geometry that can support two SPPs propagating along the two metal/dielectric interfaces.

Using the same procedure previously used for deriving the TM modes fundamental equations and the dispersion relation in the bi-layer geometry, an implicit dispersion relation for the SPPs of this system can also be found[103]:

$$\exp(-4k_m a) = \frac{k_m/\varepsilon_m + k_{d1}/\varepsilon_{d1}}{k_m/\varepsilon_m - k_{d1}/\varepsilon_{d1}} \frac{k_m/\varepsilon_m + k_{d2}/\varepsilon_{d2}}{k_m/\varepsilon_m - k_{d2}/\varepsilon_{d2}} \tag{2.41}$$

where *d1* is the lower dielectric semi-space, *d2* the upper dielectric semi-space and $a$ is the half-thickness of the metal slab. In general, Eq. 2.41 has four solutions, two "bounded" modes (like regular SPPs) and two "leaky wave" modes, with much higher propagation lengths and a lower degree of confinement[12].

As previously stated, it is not possible to excite an SPP on a flat interface unless k-matching techniques are employed. The two most common techniques are called "prism coupling" and "grating coupling". In prism coupling, a dielectric prism is usually put in contact with a thin metal layer with another (lower $\varepsilon$) dielectric on the other side. A beam reaching the interface between the prism and the metal at an incidente angle $\theta$, will have

an in-plane wave vector component $k_x = k\sqrt{\varepsilon}\sin(\theta)$ that is sufficient to excite the SPP on the opposite interface (usually air/metal), see Figure 2.15. In practice, the excitation of the SPP manifests itself as a dip in the reflection spectrum of the incident beam. The prism/metal/lower-$\varepsilon$ dielectric configuration is known as the Kretschmann configuration[108].

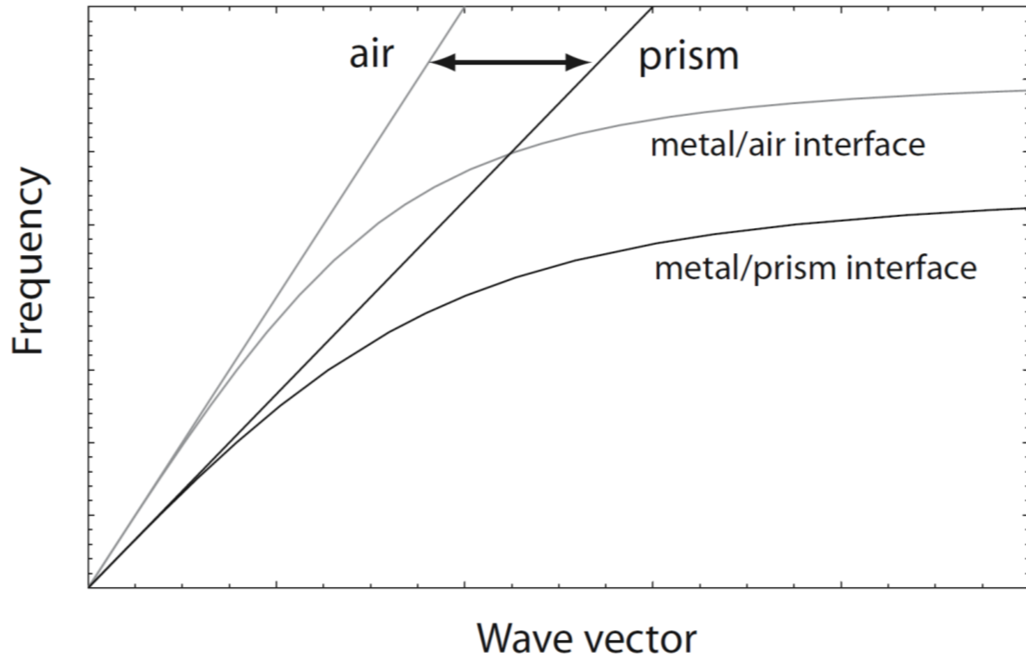


**Figure 2.15:** Example of dispersion relation after prism coupling. Note that, while the metal/air SPP curve crosses the prism light line, thus becoming excitable, the metal/prism SPP curve continues to be always on the right side of the light line. Adapted from "Plasmonics: Fundamentals and applications" (Springer, 2007).

Another possible configuration for prism coupling is the Otto configuration, in which the prism is slightly separated from the metal slab by a thin air layer[109]. Due to total internal reflection at the prism/air interface, an SPP on the metal/air surface can be excited via tunneling. This setup is preferred when direct contact between the prism and the metal must be avoided (e.g. surface quality studies). For a schematic representation of the two prism coupling configurations, see Figure 2.16.

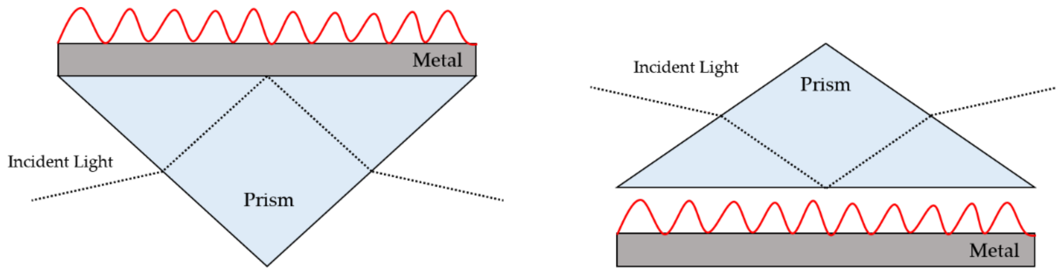


**Figure 2.16:** Schematic representation of the Kretschmann (left) and Otto (right) configuration, for prism coupling wave vector-matching.

Both prism coupling techniques are also suitable to excite SPPs in tri-layer systems ("bounded" and "leaky waves"), using index-matching oils as one of the dielectric layers[110].

An alternative method to provide the required wave vector-matching for the excitation of SPPs is given by the grating-coupled technique. A grating is a periodic pattern (usually mono-dimensional) fabricated on the metal/dielectric interface where you want to excite an SPP, with a periodicity $p$ of the same order of magnitude of the incident wavelength[111–113]. See Figure 2.17 for an example of grating coupling.

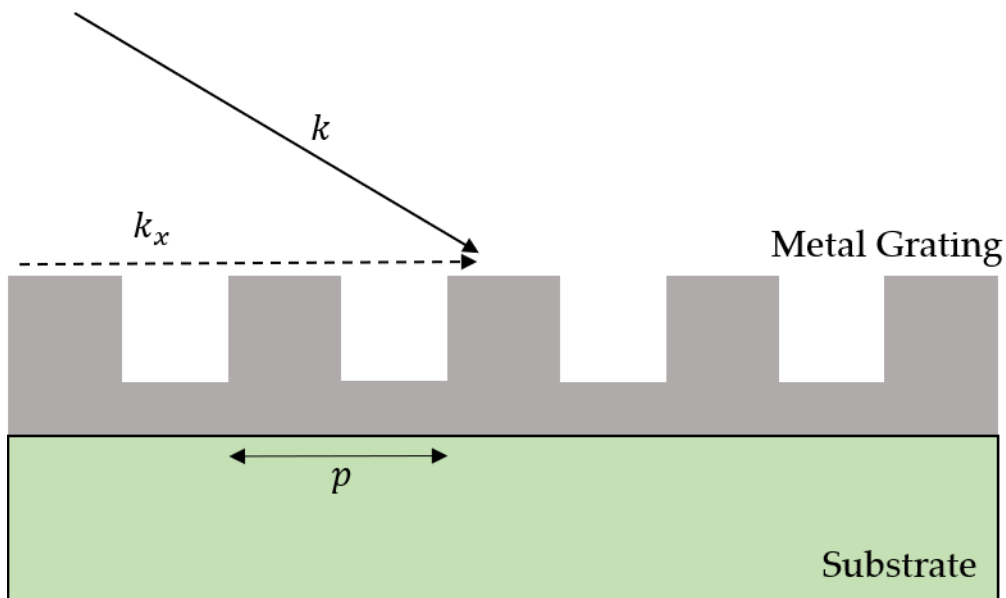


**Figure 2.17:** Schematic representation of a grating structure for wave vector-matching.

When the incident light is diffracted by a grating structure, the grating momentum, given by the Bragg vector modulus $G = 2\pi/p$, can be added to the light in-plane momentum $k_x = k\sin(\theta)$ in order to achieve the wave vector-matching conditions[114,115]. The SPP propagation constant than becomes:

$$\beta = k \sin(\theta) \pm nG \tag{2.42}$$

where $n$ is an integer number associated with the diffraction order responsible for the matching (usually the first order of diffraction). Again, the SPP excitation can be detected as a dip in the reflection spectrum of the incident light. The granting can also be fabricated on a dielectric substrate, instead of directly on metal[116], and by carefully tailoring its shape and other structural properties it is possible to influence the SPPs propagation direction, even achieving focusing[117–120].

# Chapter 3

# Simulations

In this chapter, we describe all the structures' simulations and physical considerations that must be done before fabricating any plasmonic device. In §3.1 we talk about how to properly choose the right materials for the plasmonic structure in order to maximize the enhancement effect within the constraints of an "integration" approach. In §3.2 we describe in detail the physical nature of the resonances of our system and how their peculiar hybrid essence is the central pillar of our absorption enhancement structure. Finally, in §3.3 we briefly show how to switch from a simple 2-D grating model to a more realistic, and polarization independent, 3-D "nanodots" array, while keeping all the performance enhancement from the traditional 2-D structure.

## 3.1 Choosing the Right Materials

Unlike many other research cases, our substrate, on top of which the plasmonic structure will be built, cannot be chosen at our discretion: it is a p-i-n photodiode fabricated in batch by the FBK micro-fabrication laboratories, following a precise and already optimized procedure. Therefore, our choice of materials (and fabrication techniques, see Chapter 4) is significantly more limited than usual, due to the "integration" nature of our work. For our purposes, the active area of the photodiode can be schematized by a bi-layer comprising relatively thick silicon (Si) slab of ~2 μm and a thin film of dielectric on top that serves both as a passivation layer and a protective coating for the active silicon region. Using silicon as the active area material brings several advantages over other possible choices (e.g. germanium): it's a relatively cheap semiconductor, its available on the market with a very high degree of purity and well-controlled optical/electrical properties, it is fully compatible with the CMOS fabrication process, and it can be processed into thin active layers, perfectly fitted for fast devices with small pixels (ideal for NIR photons detection). The dielectric layer cannot be neglected when simulating the plasmonic structure and is usually made of silica ($SiO_2$) or silicon nitride ($Si_3N_4$). Furthermore, an effort should be made in order to try to effectively use aluminum (Al), instead of the much more common and performant silver (Ag), as the plasmonic metal, because of its higher compatibility with the photodiode fabrication process-flow (silver and gold are considered silicon

contaminants in the semiconductor industry, thus preventing any use in the same production line as the photodiodes), in light of a possible future switch to serial production of the enhanced device.

As our starting point for simulating the plasmonic grating, we choose to use Al as plasmonic metal and $SiO_2$ as dielectric layer. The simulations are carried out using COMSOL Multiphysics™ as the go-to software. COMSOL uses the Finite Elements Method (FEM) in order to find the (approximated) description of the electro-magnetic field in our system[121]. The FEM simulation workflow can be schematized as follow:

1. Computer Aided Design (CAD) modeling of the system.

2. Discretization of the CAD model into a grid (mesh) made by primitives (e.g. triangles, squares, tetrahedrons, hexahedrons, etc.).

3. Solving the differential equations of the electromagnetic field inside each primitive domain by approximating them as a linear combination of "form functions" (polynomials).

4. Combine all the primitive solutions in order to find the total (approximated) electromagnetic field of the system.

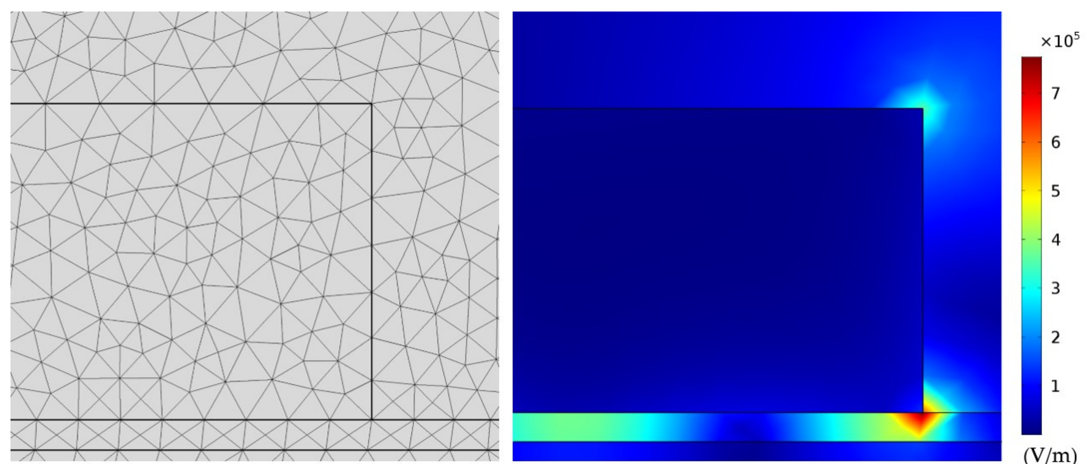


**Figure 3.1:** Example of a mesh-discretized CAD model in COMSOL (left) and its calculated electric field norm (right), expressed in terms of a color scale.

A quick COMSOL simulation for a base monolayer of Si (dielectric constant taken from the M. Green set[122]) gives us the native absorption of 2 μm of silicon at our design wavelength ($\lambda = 950$ nm, normal incidence, 1 W incident power *via* a COMSOL Periodic Port input). Due to the proximity to the silicon bandgap, only ~2% of the incident light power is absorbed inside the active

area of the photodiode, approximately estimated by COMSOL *via* integration of the total dissipated power density ("emw.Qh" calculated variable) over the Si active area (see Figure 3.2). This is in line with the absorption coefficient of Si from literature[122].

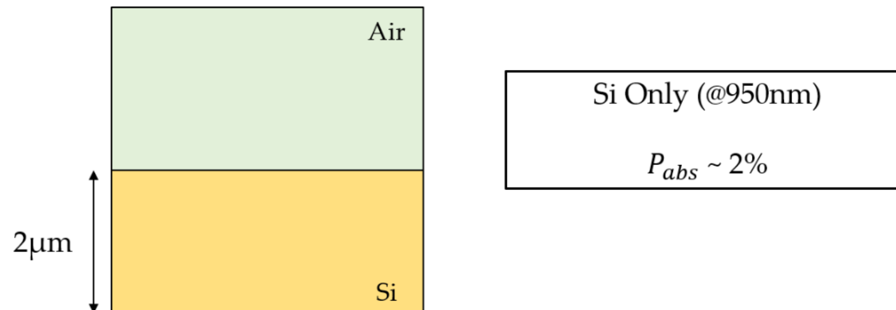


**Figure 3.2:** Incident light power absorbed by 2 μm of Si ($\lambda$ = 950 nm). The light comes from the top and travel downward.

If we add a layer of $SiO_2$ to our model and we calculate the percentage of incident power absorbed by the active Si, we find that there is already some degree of improvement from the "naked" Si situation ($P_{abs}$ ~2.8%).

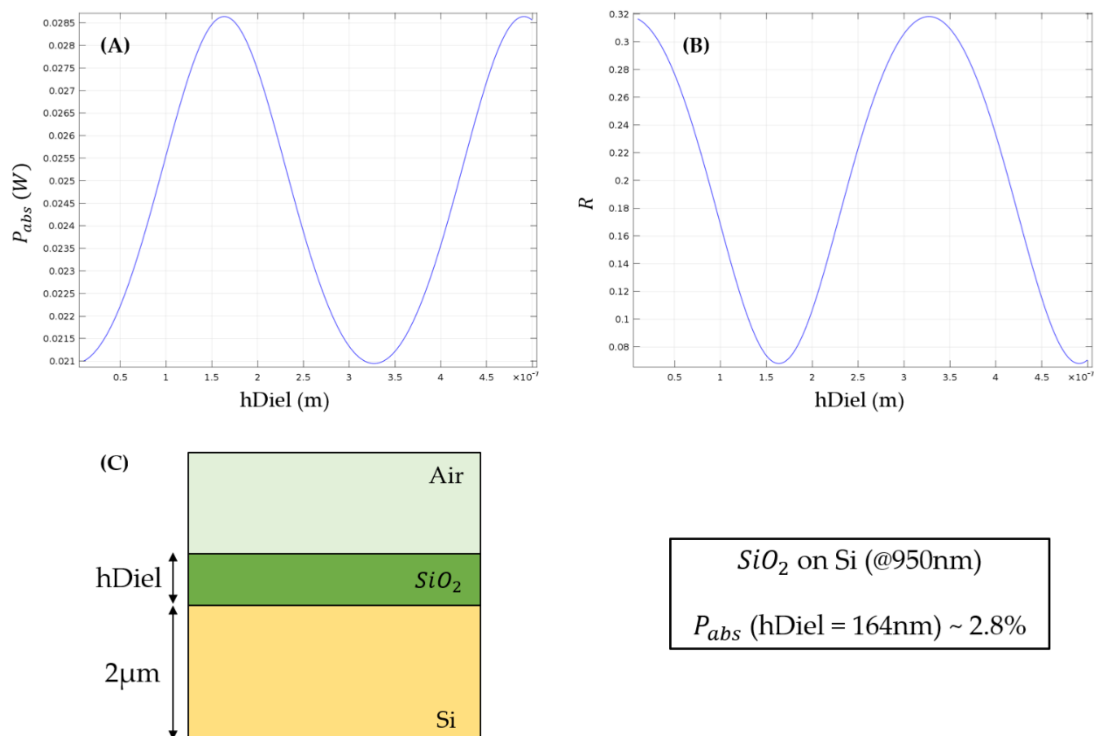


**Figure 3.3:** (A) Incident light power absorbed by 2 μm of Si ($\lambda$ = 950 nm) in a Air/$SiO_2$/Si system, as a function of $SiO_2$ thickness. (B) Reflectance spectrum of the same system, as a function of $SiO_2$ thickness. It is clearly visible that minima in the reflectance corresponds to maxima in the power absorbed, the typical behavior of an anti-reflection coating. (C) The maximum absorbed light is increased with respect to the "naked" Si model. The light comes from the top and travel downward.

This increase in absorbed light comes from a simple anti-reflection effect of the thin silica layer that only strictly works for normal incidence[123].

In order to try to increase further the absorption at 950 nm, we introduce a plasmonic grating into the system. The first plasmonic COMSOL model we consider is an "open" 2-D Al grating made of slits with a periodic interval $p$ along the x-axis and supposed "infinitely" long along the z-axis (see Figure 3.4). This simplified geometry allows us to consider only the TM polarization modes for the incident light (TE modes do not support SPPs) and to minimize the percentage of light absorbed by the metal (lost, in terms of photodetection performance), which has a significantly high absorption coefficient at 950 nm[124].

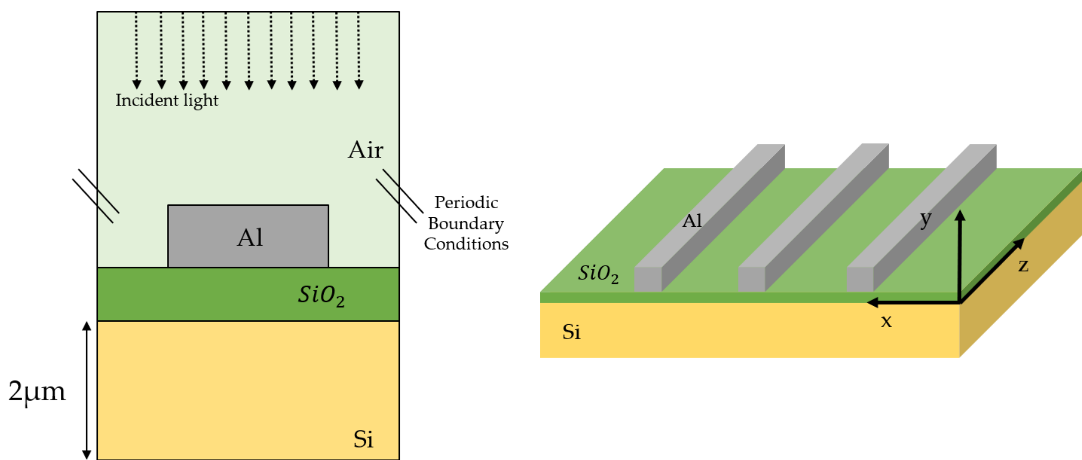


**Figure 3.4:** Schematic representation of the 2D "open" grating model used as the base COMSOL plasmonic geometry for our studies. The isolated Al slits minimize the $SiO_2$/Si surface area covered by the metal, thus reducing the "lost" light power absorbed directly by the aluminum. Periodic Boundary Conditions at both edges of the periodic cell drastically reduce the computational load and speed-up the calculations.

In order to reduce the computational power required by COMSOL to simulate this structure, we design only the fundamental periodic cell (the minimum repeating unit) of the grating and, then, set Periodic Boundary Conditions at the edges (with a Floquet periodic vector given by the wave vector of the incident light), mimicking an infinite number of cells in both directions along the x-axis. A quick initial $p$-scan at fixed $SiO_2$ thickness (10 nm), Al thickness (100 nm) and Duty Cycle (DC = 50%, the ratio of the slit x-width to the period of the grating) yields interesting results.

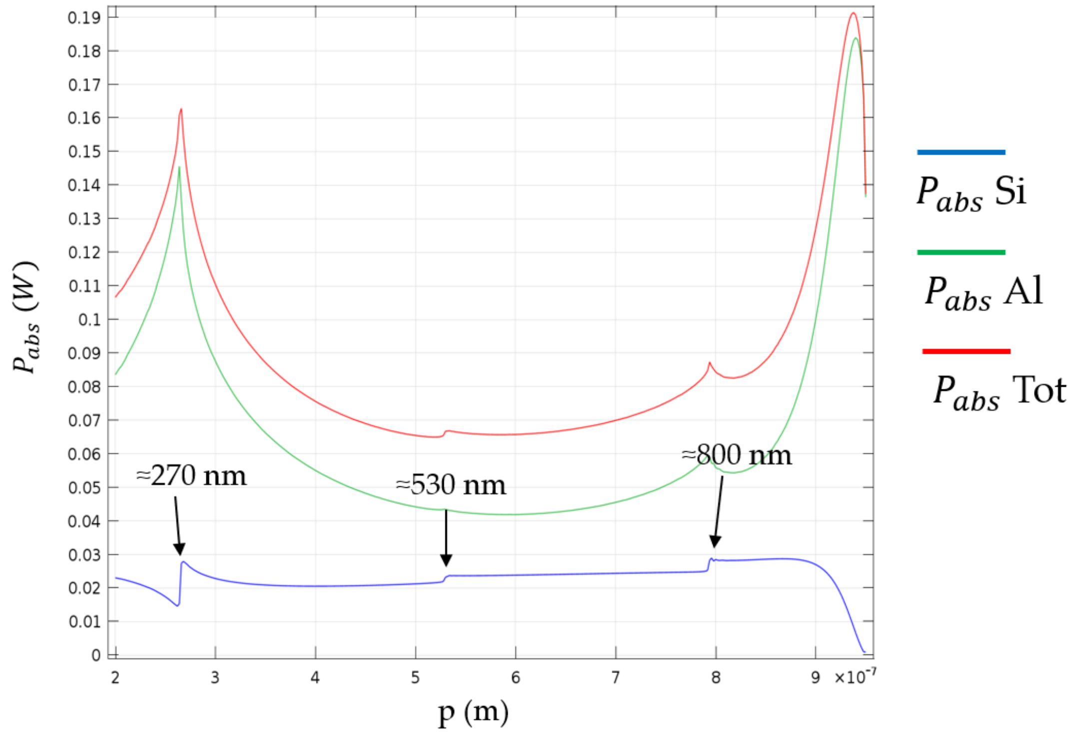


**Figure 3.5:** Incident light power absorbed by 2 μm of Si ($\lambda$ = 950 nm) in a Air/Al/$SiO_2$/Si system, as a function of the grating period. The largest contribution to the total absorbed power (red curve) is given by the light absorbed by the metal (green curve), however, three small resonance peaks can be seen at specific values of $p$ in the absorption curve of the active silicon (blue curve).

Looking at the Si light power absorbed curve, we can clearly distinguish three small resonance peaks at precise values of $p$ (270 nm, 530 nm, 800 nm). These promising resonances are obviously unoptimized, therefore we must proceed to systematically change all the grating parameters (dielectric and metal thickness, and DC) and study their effect on the absorption of the active area. This procedure must be repeated iteratively, due to the interconnections between the effect of each parameter, until a "convergence" to the maximum value of absorbed power is reached. The optimization can be easily and reliably performed by the COMSOL Optimization Module, using a Coordinate Search (derivative-free) Optimization algorithm set to explore a relatively large parameters space (±50% of the starting values). The CSO algorithm starts with an evaluation of the "objective function" (the power absorbed inside the active Si, in our case) at the initial coordinates set in the parameter space. Then, it proceeds to a small environmental search, selecting one point in each parameter axis to check for an improvement of the objective function (the search distance from the current location can be tuned by the user). If an improvement is found, the new coordinates are selected as the new base location for the next environmental search, otherwise the search distance is

halved, and the step repeated. Being a derivative-free optimization algorithm, CSO is ideal to use whenever a model optimization involves design parameters, such as parameters which control the model's geometry. The best set of grating parameters that (approximately) maximize all the resonances are: $SiO_2$ thickness = 4 nm, Al thickness = 180 nm and DC = 87%. The optimized $p$-scan can be seen in Figure 3.6. For all three values of $p$, the resonance peaks increase the power absorbed by the silicon by four times the original "intrinsic" Si absorption ($P_{abs}$ ~8% versus $P_{abs}$ ~2%).

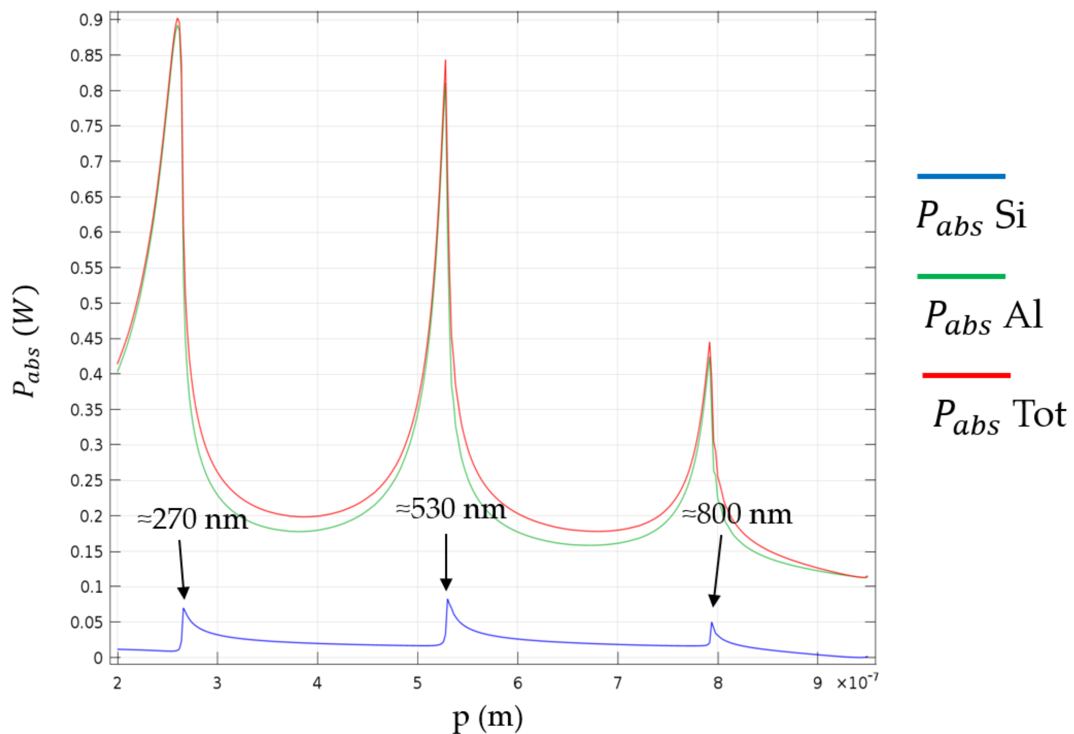


**Figure 3.6:** Incident light power absorbed by 2 μm of Si ($\lambda$ = 950 nm) in a Air/Al/$SiO_2$/Si system, as a function of the grating period, with optimized grating parameters.

The second resonance peak ($p$ ~530 nm) seems to be slightly higher than the other two, thus becoming the favored candidate for further studies.

In order to be sure of the physical "reality" of these resonances, avoiding any possible artifact due to the specific calculation method used by COMSOL, we can perform the same simulation (with identical parameters) using a custom MatLab script that makes use of the Transfer Matrix Method (TMM), originally developed for spheroids and other simple geometric shapes (like our case of a metal slab)[125–127], but eventually extended to more complex, anisotropic and layered systems[128]. From the side-by-side comparison of the two methods (see Figure 3.7) any possible doubt of software artifacts is erased: both FEM and TMM show resonance peaks at the exact same periodicities, with height differences within a few percentages.

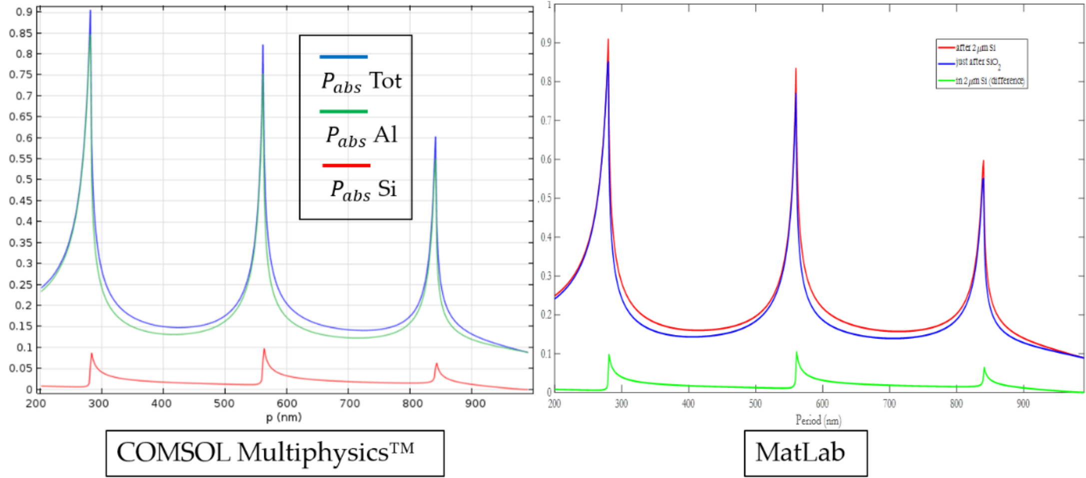


**Figure 3.7:** Example of a comparison between simulations performed with COMSOL (FEM) and MatLab (TMM). There are no significant differences between the results.

As previously mentioned, the addition of an Al grating on top of the photodetector active area increases the percentage of light power absorbed by the silicon (at 950 nm) by five times its original value. However, from a practical point of view, the simulations highlight a couple of limitations of this system. First, the required silica thickness for a maximized resonance effect is ~4 nm, which is very thin and difficult to produce in a controlled and reproducible way with the standard thermal growth process (part of the FBK production workflow). Furthermore, a dielectric layer so thin does not properly work as a passivation/protection layer for the photodiode, compromising the performance of the whole device. Second, an 8% light absorption efficiency in the near-infrared is significant, however, the same result could be achieved more easily by simply increasing the thickness of the silicon depletion region to 6-8 μm, which is still feasible (from a micro-fabrication point of view) without compromising much the overall performance of the photodiode. In order to address these problems, two materials could be changed: the dielectric of the passivation layer and the plasmonic metal. We choose to switch from $SiO_2$ to $Si_3N_4$ (another CMOS-compatible dielectric) and from aluminum to silver (much lower absorption coefficient, better plasmonic performance in the NIR). Using Ag as the plasmonic metal is tricky because it tends to tarnish relatively quickly when exposed to air, which makes difficult both to preserve the long-term performance of the grating and to use an adequate set of optical parameters that let us simulate its real behavior as a plasmonic metal. Usually, the oxidation problem is solved by capping the Ag grating with a layer of $SiO_2$ that prevents the air from reaching the metal surface. However, there is still

much debate around what is the best measured Ag dielectric function available in the literature.

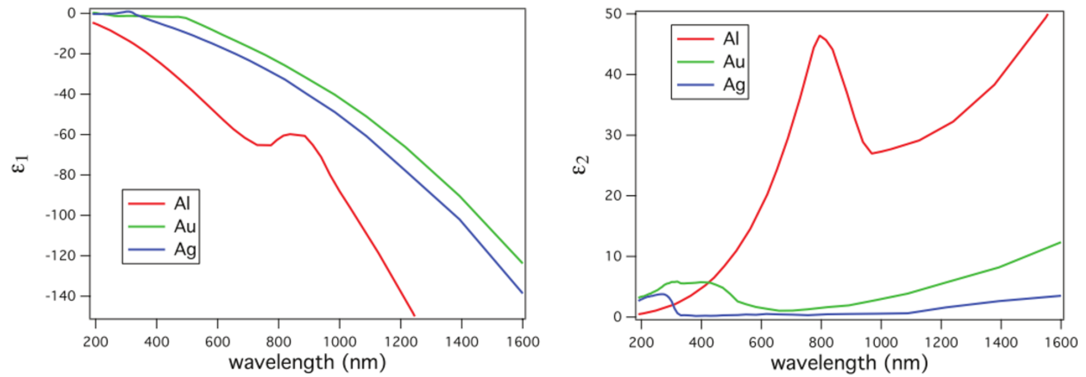


**Figure 3.8:** Real part (left) and imaginary part (right) of the dielectric functions for Al (red curve), Au (green curve) and Ag (blue curve). Ag has the lowest imaginary part of the three plasmonic metals. The peaks at ~800nm in the Al curves are associated with an inter-band transition. Adapted from Gérard, D. & Gray, S. K. Aluminium plasmonics. *J. Phys. D. Appl. Phys.* **48**, 184001 (2015).

The two most common sources for Ag optical data are Palik's 1985 handbook[129] and Johnson and Christy (J&C) tabulation[130]. However, they are inconsistent and proved to give significantly different results (J&C tends to under-estimate the absorption behavior of the metal, while Palik is prone to over-estimation)[131,132]. Recently, M. Green et al.[133] published a new set of data claiming to have solved any inconsistency and oxidation-related problem associated with the Ag dielectric function measurement. We choose to perform an in-house measurement of the optical properties of our Ag and to compare the results with the classical J&C set and the new Green set. A ion-beam evaporated Ag layer of known thickness (measured by Secondary Ion Mass Spectrometry, SIMS) on top of a silicon wafer substrate is measured using a variable wavelength ellipsometer situated inside a clean-room at FBK laboratory, in order to minimize any possible contamination, within minutes from the deposition. The refractive index $n$ and the imaginary part $k$ are derived from the amplitude ratio and the phase variation between the incident radiation and the reflected light, measured by the ellipsometer at different wavelengths[134]. The results are shown in Figure 3.9.

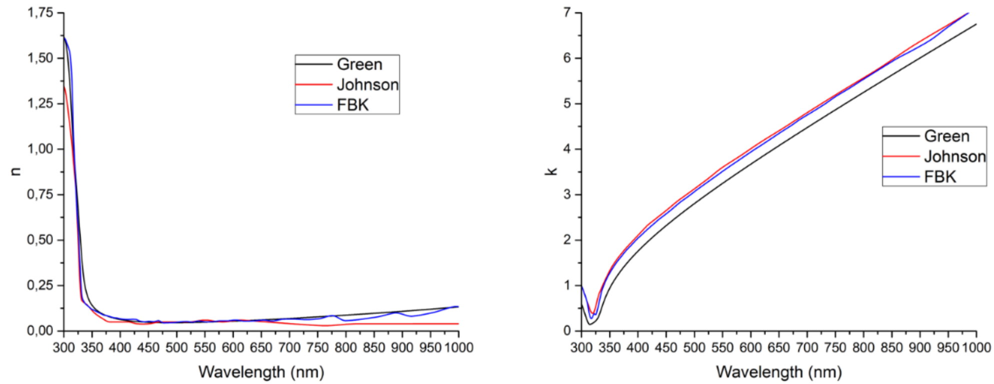


**Figure 3.9:** Comparison between the refractive index (left) and imaginary part (right) of a silver film measured at FBK with the tabulated data from Green et al. and J&C.

The measured refractive index *n* behavior follows closely the tabulated data from Green et al., while *k* seems to match J&C data (probably due to some minimal degree of Ag oxidation). Following these results, we use the "mixed" Green-J&C (real-imaginary) set of optical properties as our base for simulating the plasmonic properties of the Ag grating. After repeating the same optimization process as previously performed for the Al grating (but introducing the silica capping height as another structural parameter to be optimized), the new Ag grating on silicon nitride seems to perform even better, with the dielectric height increasing from 4nm to 11nm (much more feasible and useful as a passivation layer for the photodiode) and the power absorbed inside the active area thickness increasing by three times, from ~8% to ~25%, mostly due to the drastic decrease of the metal absorption coefficient.

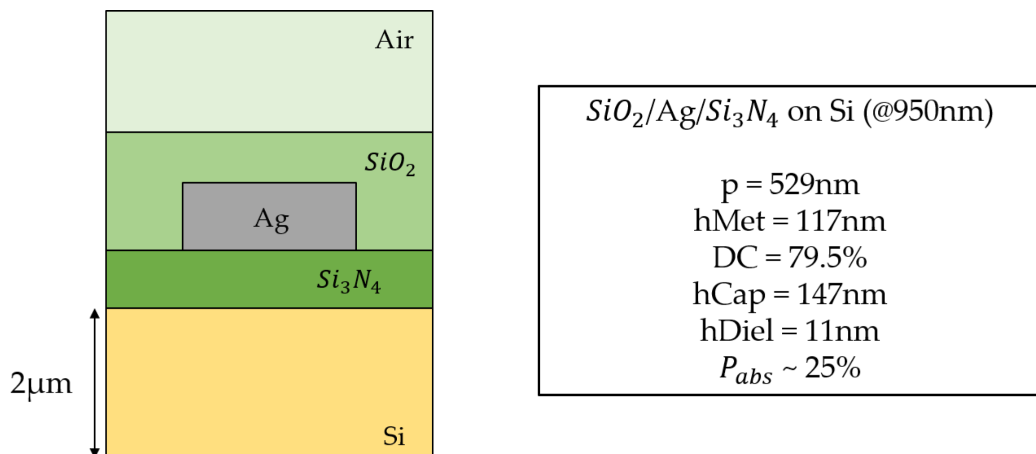


**Figure 3.10:** Schematic representation of the Ag grating on silicon nitride, protected by a silica capping layer.

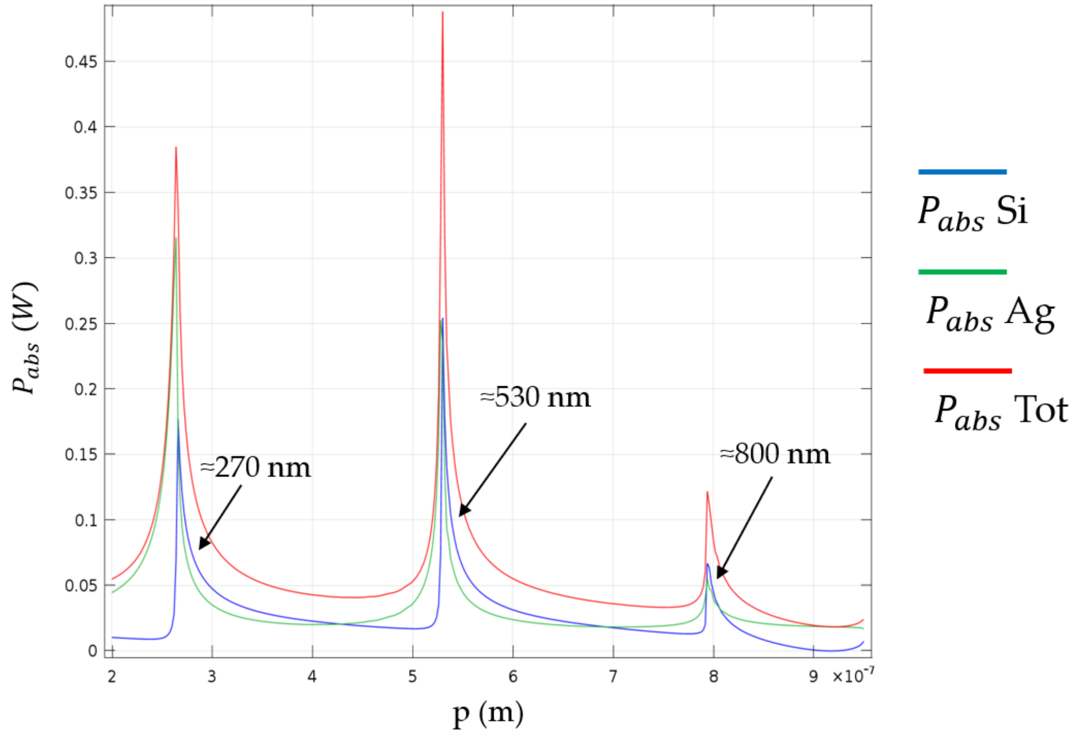


**Figure 3.11:** Incident light power absorbed by 2 μm of Si ($\lambda$ = 950 nm) in a Air/ $SiO_2$/Ag/$Si_3N_4$/Si system, as a function of the grating periodicity, with optimized grating parameters. Note that the reduced absorption coefficient of Ag with respect to Al allows for a much higher Si absorption peak at the resonance periodicity (blue curve), comparable to the power dissipated by the metal grating (green curve). Changing metal for the plasmonic grating does not shift the position of any resonance (but changes the required structural parameters).

## 3.2 The Physical Nature of the Resonances

Figure 3.12 shows a comparison between the shape of a typical plasmonic resonance peak and the shape of our resonance peak at $p$ = 530 nm. As can be seen, our resonance peak is much more asymmetric than a regular plasmonic peak. These marked differences in shape suggest a different (at least in part) nature for our resonances. A quick comparison of the electromagnetic fields simulated by COMSOL of a reference plasmonic resonance and our peak further reinforces this idea (see Figure 3.13). Studying the field of our resonance peak is a good starting point for trying to better understand its physical nature. From the COMSOL simulation, three different contributions to the total field can be identified. On the upper interface $SiO_2$/Ag, the double-lobe field profile visible in the $E_y$-component plot undoubtedly identifies a plasmonic resonance (dipole) mode.

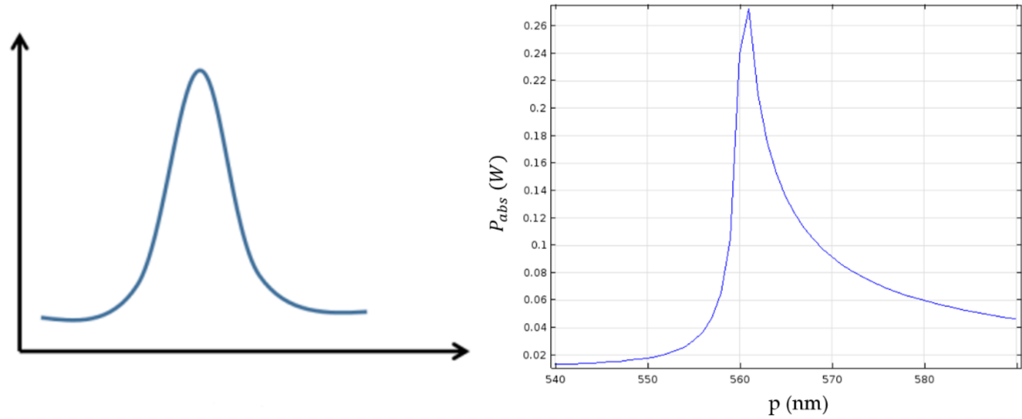


**Figure 3.12:** Comparison between a reference (generic) plasmonic peak profile (left) and our $p$ = 530 nm resonance peak profile (right). The differences in shape are clearly visible.

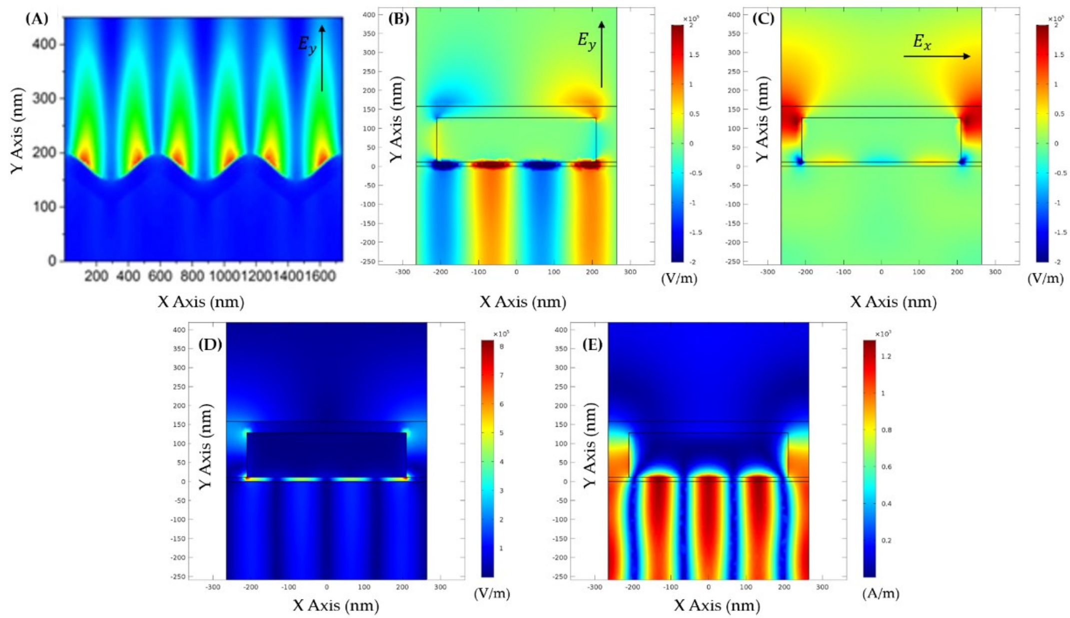


**Figure 3.13:** (A) y-component electric field plot of a reference pure plasmonic resonance (adapted from Byrne et al., "Controlled surface plasmon enhanced fluorescence from 1D gold gratings via azimuth rotations", 2017). (B) y-component electric field plot of the $p$ = 530 nm resonance of our system. (C) x-component electric field plot of the $p$ = 530 nm resonance of our system. (D) electric field norm plot of the $p$ = 530 nm resonance of our system. (E) magnetic field norm plot of the $p$ = 530 nm resonance of our system.

The multi-lobe profile at the lower interface Ag/$Si_3N_4$, visible in both the $E_y$-component and $E_x$-component plots, similarly identifies another (higher order) plasmonic mode. Instead, the reverse cone profile visible in the $E_y$-component plot, which seems to channel the incident light through the

apertures between the metal slits, is characteristic of a different kind of plasmonic effect, named Extraordinary Optical Transmission (EOT)[135].

Light transmitting through a single or multiple apertures is accompanied by diffraction, due to the wave nature of the radiation. This process can be described using several kinds of approximations[136], but in general, light impinging onto an aperture with radius $r \gg \lambda$ (Fraunhofer diffraction) produce a transmitted intensity per unit solid angle in the far field equal to[135]:

$$I(\theta) \cong I_0 \frac{k^2 r^2}{4\pi} \left| \frac{2J_1(kr\sin(\theta))}{kr\sin(\theta)} \right|^2 \tag{3.1}$$

where $I_0$ is the total incident light intensity, $\theta$ the angle between the aperture normal and the direction of the transmitted light, and $J_1(kr\sin(\theta)$ the Bessel function of the first kind. Eq. 3.1 describe the usual Airy pattern of a central bright spot surrounded by concentric rings of decreasing intensity (caused by the constructive and destructive interference between the transmitted rays). The ratio of transmitted intensity to incident intensity (transmission coefficient) is given by:

$$T = \frac{\int I(\theta)d\Omega}{I_0} \tag{3.2}$$

In the Fraunhofer regime, $T \sim 1$. However, when the aperture radius becomes very small, $r \ll \lambda$, near-field effects start to dominate the response and the Fraunhofer description of the transmitted light is no longer viable. Bethe and Bouwkamp arrived at an exact analytical solution to this problem, assuming that the incident light impinges at normal incidence and its intensity remains constant over the whole sub-wavelength aperture area (supposed perfectly opaque and infinitely thin)[137–139]. Following their approach, the new transmission coefficient is:

$$T = \frac{64}{27\pi^2}(kr)^4 \propto \left(\frac{r}{\lambda}\right)^4 \tag{3.3}$$

Eq. 3.3 implies a very weak, almost zero, total transmission intensity. Relaxing all the Bethe and Bouwkamp approximations lead to similar results but require numerical simulations for solving the problem. The transmitted intensity through sub-wavelength apertures can be dramatically enhanced by periodic metal gratings. This structures can support SPPs that significantly increase the electromagnetic field above the apertures if properly coupled, leading to a transmission coefficient that peaks at the plasmonic excitation wavelength a can become even greater than one, meaning that more light passes through the holes than impinges on their total area. This phenomenon is commonly called Extraordinary Optical Transmission[140–142].

Therefore, the resonance peak we are considering in our system seems to comprise an upper interface dipole SPP coupled to an EOT mode inside the apertures between the metal slits that significantly increases the amount of light intensity passing through the grating, enabling the efficient excitation of another lower interface quadrupole SPP. This triple matching configuration is a well-known phenomenon and is exploited in another type of detector in order to increase its performance[143]. However, this description still does not include all the features that can be identified observing the electromagnetic field plots. In fact, looking at the magnetic field norm plot in Figure 3.13, none of the previously cited effects can be associated with the long tails that stretch inside the Si active area, effectively causing the drastic increase in the absorption efficiency at 950 nm. A simple SPP would confine the light inside a much tighter region (a few hundreds of nanometers), while in our case the simulations tell us that the tails extend into the semiconductor up to a hypothetical thickness of 5 μm. See Figure 3.14 for a visual comparison of the difference in confinement between a common (triple-matched) SPP (without the nitride layer) and our case.

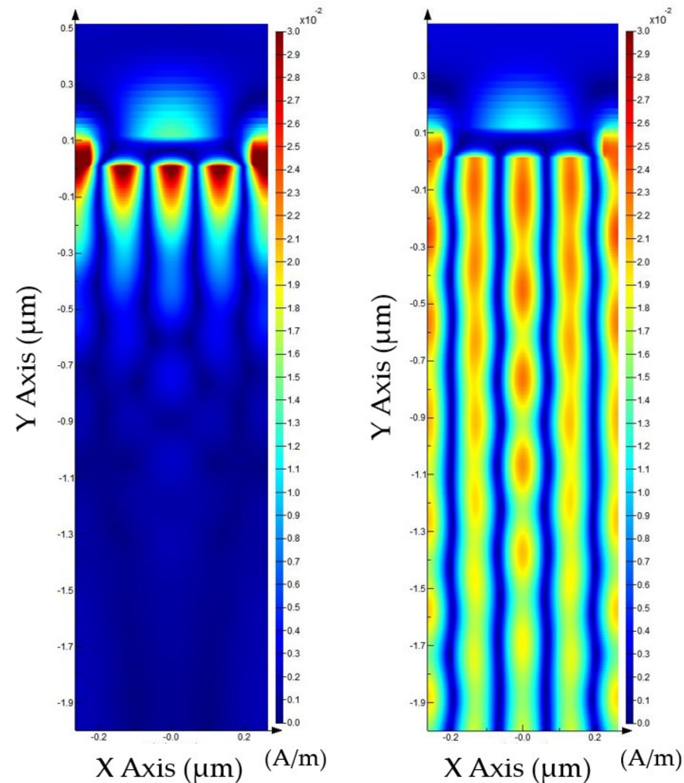


**Figure 3.14:** Comparison between the magnetic field norm plot of a triple-matched SPP (left) and the peculiar resonance of our system (right).

In order to identify the last contribution to our resonance peak, we perform a systematic study of absorbed power and reflectance as a function of both periodicity and incident wavelength, while also varying the thickness of the silicon nitride layer, which seems to be somewhat connected to the "tails effect". The absorption and reflectance maps produced by this study can be seen in Figure 3.15. The first information that the maps give us is that the dispersion relation (from Eq. 2.40, the relation between the propagation constant $\beta$, which depends on the period for grating coupling excitation, and the dielectric function of the metal/dielectric, which depends on the incident wavelength) of the lower interface SPP changes with varying nitride layer thickness. This suggests that even very thin passivation layers affect the lower interface SPP propagation. The effect is particularly visible in the $P_{abs}$ Ag maps for increasing $Si_3N_4$ thickness. The second fundamental information that can be extrapolated from the maps, especially the $P_{abs}$ Si and R maps, is that there is some sort of "light line" that does not change or shift by varying the nitride thickness, thus must be independent from it, and that causes the SPP to "vanish" once crossed, while also increasing the power absorbed by the active area. From the behavior of the SPP at varying nitride thickness, we can approximate the dispersion relation equation that governs the lower interface plasmon. We know from Chapter 2 that the general form of a dispersion relation is given by Eq. 2.40. Combining Eq. 2.40 with Eq. 2.42 for the propagation constant in a grating coupling configuration, we obtain:

$$p = \frac{n2\pi}{\frac{2\pi}{\lambda}\sqrt{\frac{\varepsilon_d \varepsilon_m}{\varepsilon_d + \varepsilon_m}} - k_{inc}\sin(\theta_n)} \tag{3.4}$$

As previously mentioned, the SPP is affected by the thin dissipation layer, therefore $\varepsilon_d$ must include also a (variable) contribution from the $Si_3N_4$ optical properties. This contribution can be calculated using the Effective Medium Approximation (EMA). EMA treats the underlying layers as an effective medium whose effective dielectric function $\varepsilon_{EMA}$ is determined by the sum of all contributions from the layers weighed by their distance from the interface, using the exponential decay of the SPP field[144,145]. For a system made of N layers, each of thickness $d_i$ and permittivity $\varepsilon_i$, the effective dielectric function can be described as:

$$\varepsilon_{EMA} = \frac{2}{\delta_d}\sum_{i=1}^{N}\int_{d_{i-1}}^{d_{i-1}+d_i} \varepsilon_i \exp\left(-2\frac{y}{\delta_d}\right) dy \tag{3.5}$$

where $\delta_d$ is the SPP penetration depth into the dielectric multi-layer and $y$ is the direction perpendicular to the multi-layer system. Since also the penetration depth depends on $\varepsilon_{EMA}$, according to:

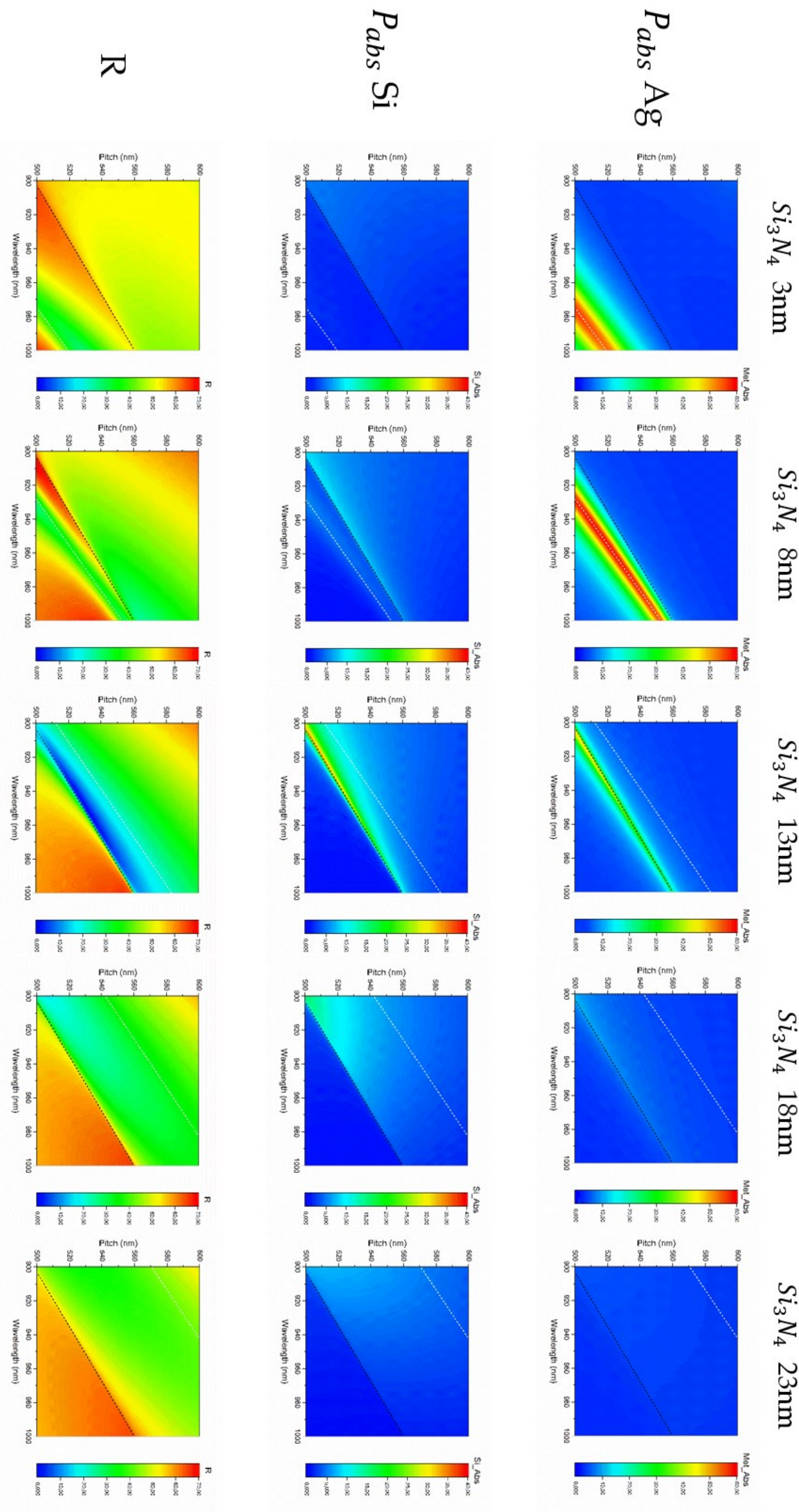


**Figure 3.15:** Absorption and reflectance maps for different values of $Si_3N_4$ thickness (rows). The dotted curves represent the calculated lower interface SPP dispersion relation profile (white dots) and the Rayleigh singularity profile for the second order of diffraction (black dots).

$$\delta_d = \frac{\lambda}{2\pi}\sqrt{\frac{\varepsilon_{EMA} + \varepsilon_m}{-\varepsilon_{EMA}^2}} \tag{3.6}$$

an iterative calculation carried out until convergence is reached must be performed in order to solve Eq. 3.5. We used a custom MatLab script in order to iterative calculate the $\varepsilon_{EMA}$ of our $Si_3N_4$/Si dielectric bi-layer. The lower interface SPP is excited by some order of diffraction of the transmitted light coming out from the apertures between the metal slits (*via* EOT coupling), therefore, $k_{inc}$ is given by:

$$k_{inc} = \frac{2\pi}{\lambda} n_{Si_3N_4}(\lambda) \tag{3.7}$$

where $n_{Si_3N_4}(\lambda)$ is the refractive index of the nitride layer. The last two parameters of Eq. 3.4 that must be considered are the order of diffraction that excite the SPP ($n$) and the angle of propagation of this order ($\theta_n$). The angle of propagation is difficult to evaluate *a priori* because it depends from the exiting angle of the transmitted light passing through the apertures thanks to the EOT effect, as can be seen using the grating equation[146]:

$$n_{EMA}(\lambda)\sin(\theta_n) = n_{SiO_2}(\lambda)\sin(\theta_{ext}) - \frac{n\lambda}{p}\sin(\phi) \tag{3.8}$$

where $n_{EMA}(\lambda)$ is the refractive index of the effective medium, $\theta_{ext}$ is the angle at which the light exists the apertures an $\phi$ is the grating in-plane orientation ($\sin(\phi) = 1$ for TM mode incident light).

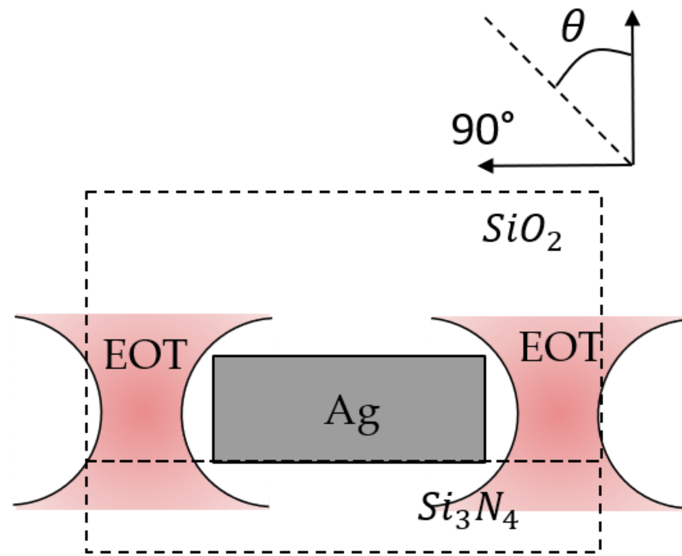


**Figure 3.16:** Schematic representation of the light passing through the apertures between the metal slits *via* Extraordinary Optical Transmission.

However, it can be fitted *a posteriori* to the profile seen on the maps if it is the only unknown parameter. The number of the diffraction order $n$ can be deducted considering the other interesting phenomenon previously mentioned, the "light line". A description of a phenomenon produced by the diffraction from a periodic grating that depends only from the period and the incident wavelength can be found in the literature examining the work of Robert W. Wood on the so-called Wood's anomalies[112]. In general, Wood's anomalies are abrupt variations in the transmitted (diffracted) spectrum of light passing through a grating (not necessarily of plasmonic nature). There are two types of anomalies. The Type 1 is known as Rayleigh singularities[112] and corresponds to variations in the spectrum due to the intensity modulation of diffracted orders by the onset or disappearance of other diffracted orders. The inequation that governs the singularities is:

$$p > \frac{n\lambda}{n_{sub}} \tag{3.9}$$

where $n$ is, again, the number of the order of diffraction that starts to propagate if Eq. 3.9 is satisfied and $n_{sub}$ is the refractive index of the substrate into which the diffracted light propagates. Plotting the trend of Eq. 3.9 onto the absorption and reflectance maps (using $n_{sub} = n_{Si}$, as it appears to be independent from the nitride layer) shows that the "light line" is actually the Rayleigh singularity for the second order of diffraction of the light passing through the apertures ($n = 2$, see black curves in Figure 3.15). Following this consideration, substituting $n = 2$ in Eq. 3.4 and combining it with Eq. 3.5 and Eq. 3.7 we find that the SPP on the maps can be described by a dispersion relation which implies a $Si_3N_4$-"confined" second order of diffraction (capable of propagating into the nitride thin layer but not into the silicon underneath) that excite the plasmon by impinging on the lower interface of the grating with an average (fitted) angle of 5-10° (see Figure 3.16 for $\theta$ orientation, see white curves in Figure 3.15). This order can start the propagation of the SPP only while is "confined" into the passivation layer. When the dispersion curve crosses the singularity line (increasing the nitride thickness), the $n = 2$ starts to propagate into the Si active area and the SPP vanishes. In the special conditions when the SPP dispersion curve "couples" with the Rayleigh singularity, our resonance peak appears, and the Si absorption is enhanced. These conditions are met when the SPP lays slightly above the singularity line in the maps, but it does not vanish yet (becoming a "leaky wave"). It can be shown that all three resonances ($p = 270$ , $p = 530$ and $p = 800$) derive from the "coupling" between an SPP dispersion curve and a Rayleigh singularity ($n = 1$, $n = 2$ and $n = 3$, respectively). These "hybrid" opto-plasmonic resonances fall into the Type 2 category of Wood's anomalies, which comprises resonance conditions arising from "leaky waves" modes (the "tails" on the maps) supported by the

grating (see Chapter 2, §2.3)[147]. Type 2 resonances belong to the family of the Fano resonances, which are described by:

$$I \propto \frac{(F\gamma + \omega - \omega_0)^2}{(\omega - \omega_0)^2 + \gamma^2} \tag{3.10}$$

where $\omega_0$ and $\gamma$ are parameters that denotes the position and width of the resonance, and $F$ is the Fano parameter, which determines the degree of asymmetry of the profile. In general, Fano resonances arise from the constructive and destructive interference between a narrow bandwidth resonance (the diffracted order, in our case) and a broad spectrum or continuum resonance (the SPP, in our case)[148].

## 3.3 3-D Plasmonic Model Extension

Real-life applications of photodiodes sometimes require an unpolarized or circularly polarized incident light. As previously stated, 2-D gratings are very useful for understanding the optical and plasmonic phenomena that their use introduces in an already complex system, like a photodetector, mainly because only TM modes need to be considered. However, for any practical application, an extension to a 3-D model is usually a significant improvement toward a real understating of how a device would really perform, if not even a necessary step. In our specific case, a 3-D plasmonic structure would need to perform equally well (support Wood's anomalies) for any kind of incident light polarization, thus becoming polarization-independent. Assuming that the light impinges on the device along the y-axis, a 3-D "grating" that works for both x and z linear polarizations should be effectively polarization independent[146].

A simple way to achieve this condition is to consider the intersection of two distinct 2-D gratings, perpendicular to each other, into a single 3-D resulting structure made of "nanodots" (see Figure 3.17)[149–153].

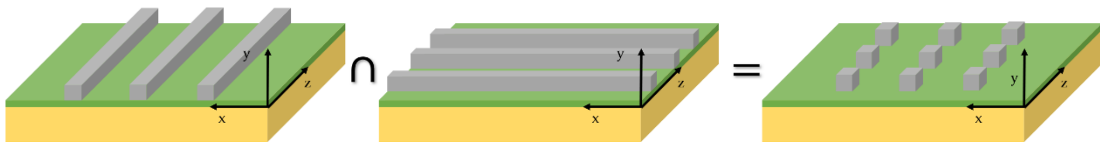


**Figure 3.17:** Schematic representation of the "intersection" of two perpendicular 2-D gratings in order to produce a 3-D "nanodots" array that is polarization independent.

The nanodots 3-D array can be simulated in COMSOL using the same workflow of design and optimization previously described for the 2-D grating in §3.2. The optimized structure has the same parameters as the 2-D grating, the resonances appear for the same set of period/wavelength but the absorption enhancement is evenly split between the two perpendicular directions (using TM and TE light) instead of entirely concentrated into a single direction, perpendicular to the 2-D grating (only TM modes).

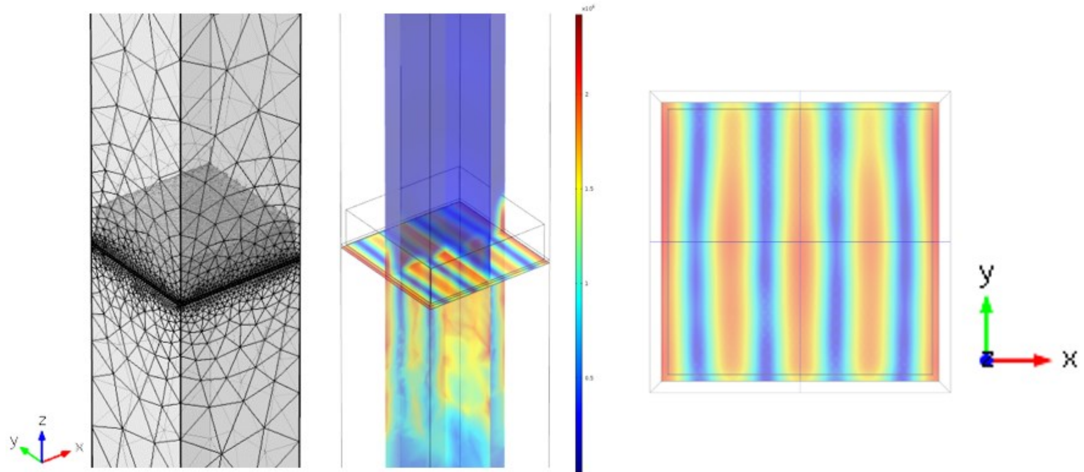


**Figure 3.18:** 3D CAD model (already with a mesh applied to it) of the periodic cell of the nanodots array (left), an example of simulated magnetic field norm for the structure (middle) and the same field simulation seen along the z-axis (right).

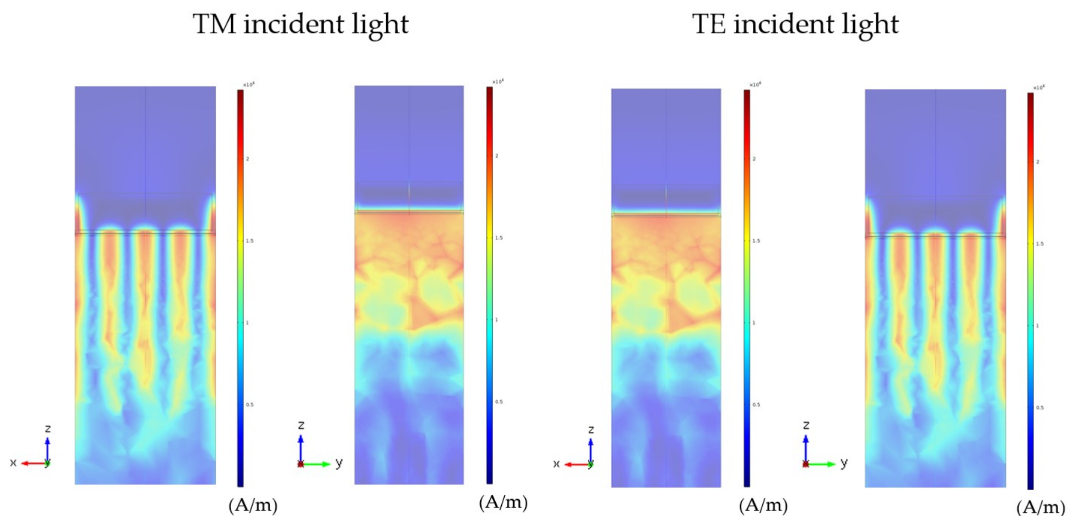


**Figure 3.19:** Magnetic field norm from a COMSOL simulation perform with "TM" incident light (left) and "TE" incident light (right). The same field patterns appear in both cases, but their orientation is switched. The absorption enhancement results to be evenly split between the two perpendicular directions (considering "TM" and "TE" together). Due to the computational load of a 3D model, a compromise on the mesh elements size must be done, which gives less precise results and the "noisy" look to the calculated fields plots.

# Chapter 4

# Prototype Fabrication Process

In this chapter, we describe the entire fabrication process that is required in order to obtain a working prototype of our enhanced photodetector. In §4.1, we make a brief overview of the two main steps of the fabrication process. Then, in §4.2 we describe the nanofabrication procedure that leads to a patterned polymeric film over the substrate that can be used as a base for the second fabrication step, the Metal Evaporation. Finally, in §4.3 we show how to obtain a prototype device with an Ag nanodots array over a standard photodiode using a combination of vacuum metal deposition and residual polymeric layer stripping.

## 4.1 Enhancement Structure Fabrication Process

In order to fabricate our metal structures on top of FBK silicon photodiodes, a two-step process is required. In the first step, we draw the structure reverse-pattern into a polymeric layer (called "resist") deposited on top of the substrate (photodiode) *via* a direct-writing technique known as Electron Beam Lithography (EBL). Then, in the second step, we transfer the pattern (inverting it, thus obtaining the desired structure) *via* Metal Evaporation (ME) directly on top of the active area of the detector. Before going into the details of the first step of the fabrication process, we will now briefly describe the EBL patterning technique and the ME, in order to highlight their advantages and limitations.

The Electron Beam Lithography was used for the first time in 1985 by a Stanford University graduate student, Tom Newman, to win a challenge issued in 1959 by Richard Feynman in his famous talk "There's Plenty of Room at the Bottom"[154]. Newman claimed the prize by writing the first page of Charles Dickens "A Tale of Two Cities" inside a 6 $\mu m^2$ area[155]. EBL uses similar hardware to the Scanning Electron Microscope (SEM) to guide a focused beam of electrons inside a thin "resist" layer to draw the desired pattern (generated by a simple CAD file). Electrons used by EBL are particularly useful to us: they are very light charged particles; thus, they can be tightly focused by weak electric and magnetic fields, and, due to their light mass, they can penetrate relatively thick layers of material without displacing any heavier particles. Because of their small wavelength (~4 pm), electrons do not generate any diffractive artifact. Overall, electrons allow us to achieve a high degree of

precision and high resolution in patterning our structures (EBL typically uses 20-100 KeV electrons). However, there are also some disadvantages in using electrons: EBL requires the entire system to be kept under vacuum, in order to prevent electrons collisions with gas molecules, and the absolute absence of any residual charging, which would deflect the beam in undesirable directions. In order to satisfy both these conditions, the complexity (and cost) of the lithographic system turns out to be very high. Furthermore, electrons undergo both small-angle and large-angle scattering events (inelastic and elastic, respectively) inside the polymer layer and in the substrate, which give rise to unwanted exposure in areas surrounding the pattern features, a phenomenon called “proximity effect”. We will address how to properly treat the “proximity effect” in the next paragraph.

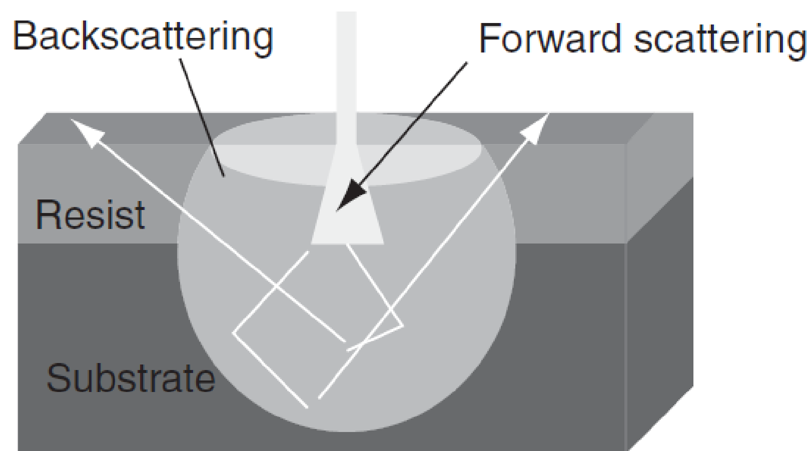


**Figure 4.1:** Schematic representation of the forward-scatter and back-scatter interaction of electrons with a resist-coated substrate. Adapted from “Handbook of Nanofabrication” (Elsevier, 2009).

Figure 4.2 shows a schematic representation of a modern EBL system. The main component of an EBL column is the electron source, also called a “gun”, which usually is a field emission source. As soon as the beam leaves the source, it encounters the gun alignment system, consisting of electrodes that bend and steer the beam along the colum axis. Then, a zoom condenser allows the user to change the beam current (thus its diameter) without appreciably changing its focal plane. Further below, the stigmator helps make the beam round, to produce equal linewidths along various scanned directions, whereas the dynamic focus and stigmation components allow correcting in real-time the possible height variations that the system detects during the exposure. The deflector consists of two different stages: the sub-deflector, which enables high-speed scanning through digital-to-analog (DAC) electronics, and the main-deflector, whose scanning is achieved by tilting together the sub-

deflector with a high-precision. The maximum sub-field size is typically ~4 μm, while the maximum main field is ~1 mm. These values can be increased up to a maximum writing field of ~2 $mm^2$. Given this limitation, large patterns must be "stitched" together by precisely moving the specimen stage (with the help of reference marks). The stage fine control is tracked by a laser interferometer that can resolve position changes in the 0.3-0.6 nm range.

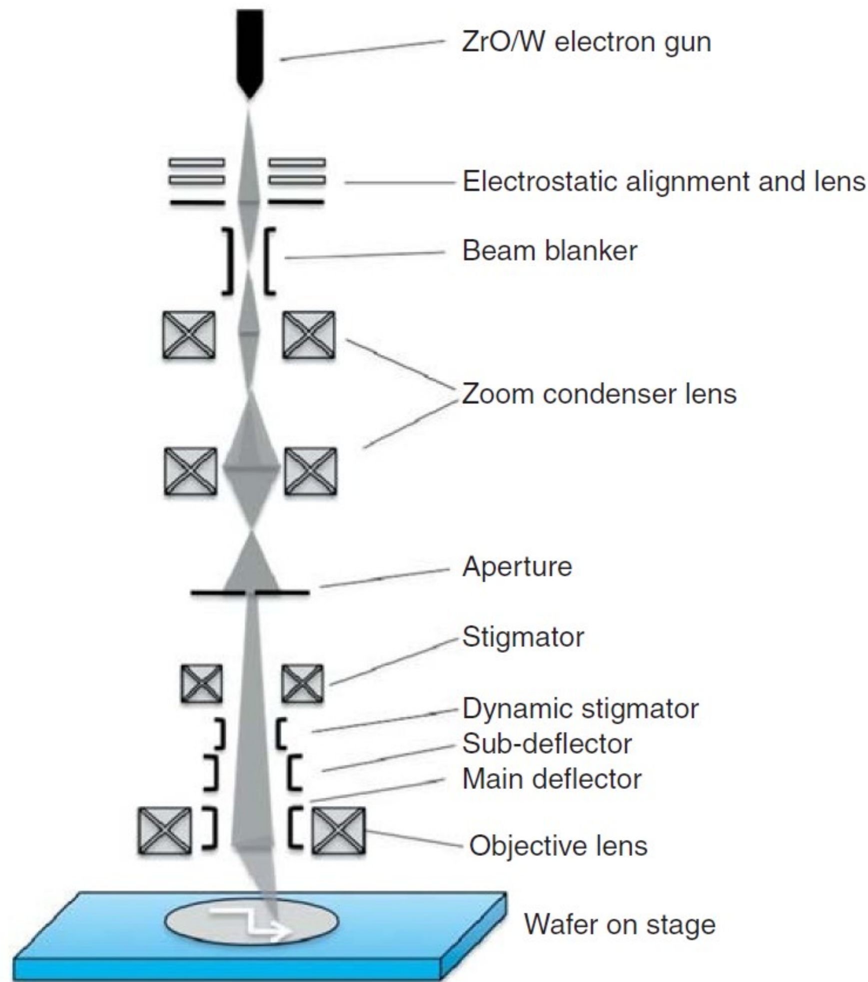


**Figure 4.2:** Schematic representation of a modern EBL system. Adapted from "Handbook of Nanofabrication" (Elsevier, 2009).

Writing a pattern with an EBL system involves several working steps. The first step consists in coating the chosen substrate with a polymeric layer called "resist". Actually, the resist is a solution consisting of a polymeric compound that changes its chemical properties when exposed to appropriate radiation (in our case, electrons), a sensitizer, which enhances the chemical properties of the polymer, and a solvent. The substrate is coated *via* spin-coating, a technique that produces a polymer film through the high-speed rotation of a

deposited resist drop, driving off the edge the excess material until only a thin layer remains, retained by surface tension and viscous forces. The final resist film thickness is given by[156]:

$$h = k\frac{C^{\beta}\eta^{\gamma}}{\omega^{\alpha}} \tag{4.1}$$

where *C* is the resist concentration, $\eta$ the viscosity of the resist, $\omega$ the angular velocity and $k, \alpha, \beta, \gamma$ calibration constants (experimentally determined). This step is usually followed by a thermal treatment of the sample, in order to evaporate the residual solvent from the polymeric film ("pre-bake"). The next step is the "exposure" of the resist film, where we use the EBL electron beam to change the polymer solubility. The amount of charge absorbed per square centimeter ($\mu C/cm^2$) by the polymer is known as the "dose". A higher dose on a certain area means a higher local solubility change, thus the possibility to modulate the film profile through variations of the local dose. In general, the resists can be divided into "positive" and "negative" resists, depending on whether the exposure increase or decreases the polymer solubility. The third step is the "development": the exposed polymer is selectively removed by an appropriate solution (the developer). The result will be the desired pattern on the resist residual layer. A resist that undergoes very little changes in non-exposed areas, while being completely removed in regions where the dose exceeds a threshold value (if it is positive, otherwise, for negative resists the opposite is true), is said having a high-contrast ($\gamma$) value. The contrast is defined as[157]:

$$\gamma = (log_{10}(D_{100}/D_0))^{-1} \tag{4.2}$$

where $D_{100}$ is the "clearing" dose (complete resist removal) and $D_0$ is the dose below which no resist is removed after development (if the resist is positive, otherwise, for negative resist the opposite is true). An optional fourth step consisting of another thermal treatment of the sample ("post-bake") can be performed after the development in order to remove any residual developer and moisture from the patterned resist layer or to increase its etching resistance (for fabrication process involving an etching step).

The other major technique that is required to fabricate our enhanced photodiodes is the Metal Evaporation. The ME process belongs to the Vacuum Depositions family and, therefore, is a Physical Vapor Deposition (PVD) method in which the (metal) atoms from a vaporization source reach the substrate without collisions with residual gas molecules inside the deposition chamber. In order to start any evaporation process, the vapor pressure must be increased above its saturation value, defined as the vapor pressure at which a material is in equilibrium with its solid or liquid surface inside a closed container. In Vacuum Depositions, this condition is achieved thanks to a

thermal source that heats the "target" material to a temperature where the vapor pressure becomes appreciable and atoms start to escape from the target surface into the vacuum. The minimum required vapor pressure for a reasonable deposition rate is set at $10^{-2}$ Torr. However, usually, Vacuum Depositions are performed with a vacuum better than $10^{-4}$ Torr[158]. The most common heating technique is resistive heating, but there is also the possibility of using high/low energy electron beams/ion beams and inductive heating. In the case of resistive heating, the increase in temperature of the target is achieved by contact to a hot surface that is heated by passing a current through it[159]. Usually, the heated surface is in the form of a crucible, which contains the target material (a metal for ME), and is made of tungsten (W), tantalum (Ta), molybdenum (Mo), graphite (C) or BN/$TiB_2$ composite ceramics. Radiation shields, made of several separated refractory metal sheet, can be positioned surrounding the vaporization source in order to reduce the power requirements and radiant heating, allowing the source to reach higher temperatures, and achieve more uniform heating. Due to the vacuum environment, atoms travel from the target to the substrate in a straight line ("line-of-sight" travel), therefore the deposition occurs with a very low degree of conformality (the target material does not deposit onto substrate surfaces that are not directly into the line-of-sight of the target). This peculiar characteristic can be exploited, in our case, in order to keep the lateral surfaces of the patterned resist "clean" from the metal, thus enabling the "stripping" of the residual polymeric layer after the evaporation, in a process called Lift-Off.

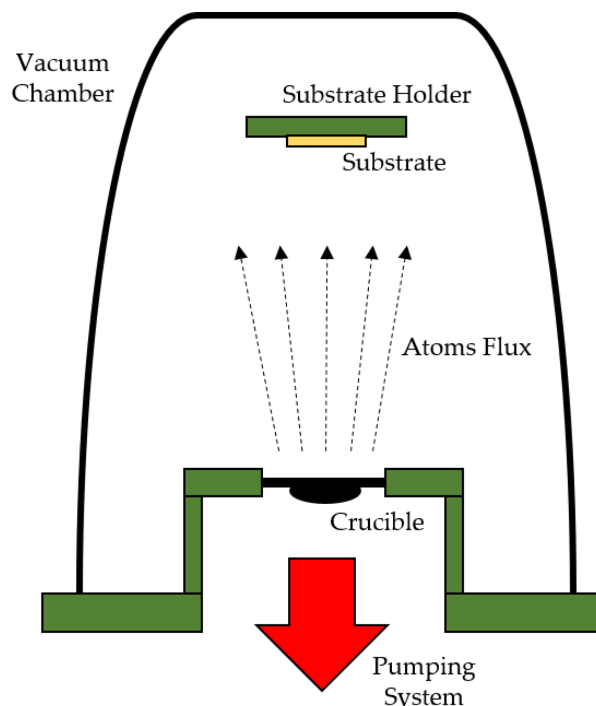


**Figure 4.3:** Schematic representation of a Metal Evaporation chamber.

## 4.2 EBL Nanofabrication

As previously mentioned, the first step of our fabrication process is to perform direct writing of the desired pattern into a polymeric layer deposited on the substrate provided by FBK. Keeping in mind that the next step (ME) will transfer the "negative image" of the EBL written pattern onto the substrate, here we want to design and expose the inverted pattern, thus obtaining the corrected one at the end of the fabrication flow. From the simulation studies, we know that our optimal pattern must have a DC of ~80% and a (final) Ag height of ~150 nm. Usually, in order to have a successful Lift-Off, the patterned resist should be at least three times higher than the desired metal height, therefore we need to draw a pattern with features at least ~450 nm tall and ~100nm wide (the pattern must be inverted, therefore the DC becomes ~20%, with a desired period of 529 nm). Features with an aspect ratio (ratio between their height and width) greater than three are extremely difficult to fabricate *via* EBL, because most positive resists tend to collapse due to the inherent "under-cutting" (the electron beam passing through the polymeric layer tends to expose a cone-shaped volume, thus producing features with a narrower base the higher they are). This problem is further exacerbated by the 2-D grating structure, which would require an EBL pattern of very long and very thin lines. One possible solution is to choose a negative resist, completely removing the under-cutting problem. However, besides intrinsic difficulties in working with negative resists, this choice would significantly increase the complexity of the fabrication process because it would require the addition of another EBL step with a positive resist on top of the patterned negative resist (before the metal evaporation) in order to be able to perform the final Lift-Off step, otherwise the substrate would be completely coated with silver[160–162]. Another solution would be using a bi-layer strategy, adding a PMGI thin layer before the resist layer, which has high resistance to under-cutting[163–166]. Again, however, this would increase the fabrication process complexity. After some preliminary tests, we choose to slightly reduce the target DC to 75% and to switch to the 3-D nanodots array from the start. The reverse-pattern of the nanodot array is a "grid", auto-sustaining its features very efficiently. Therefore, this configuration can survive an aspect ratio up to six while using a common, high resolution, PMMA-based positive resist (A7, MicroChem).

A schematic representation of the substrate provided by FBK can be seen in Figure 4.4. It is a highly non-uniform substrate comprising several photodiodes with different sized active areas (from 2x2 $mm^2$ to 100x100 $\mu m^2$) occupying a total surface area of 1x1$cm^2$. This heterogeneous topography, especially in terms of height variance, could raise some problems with the resist thickness homogeneity during the spin coating resist deposition.

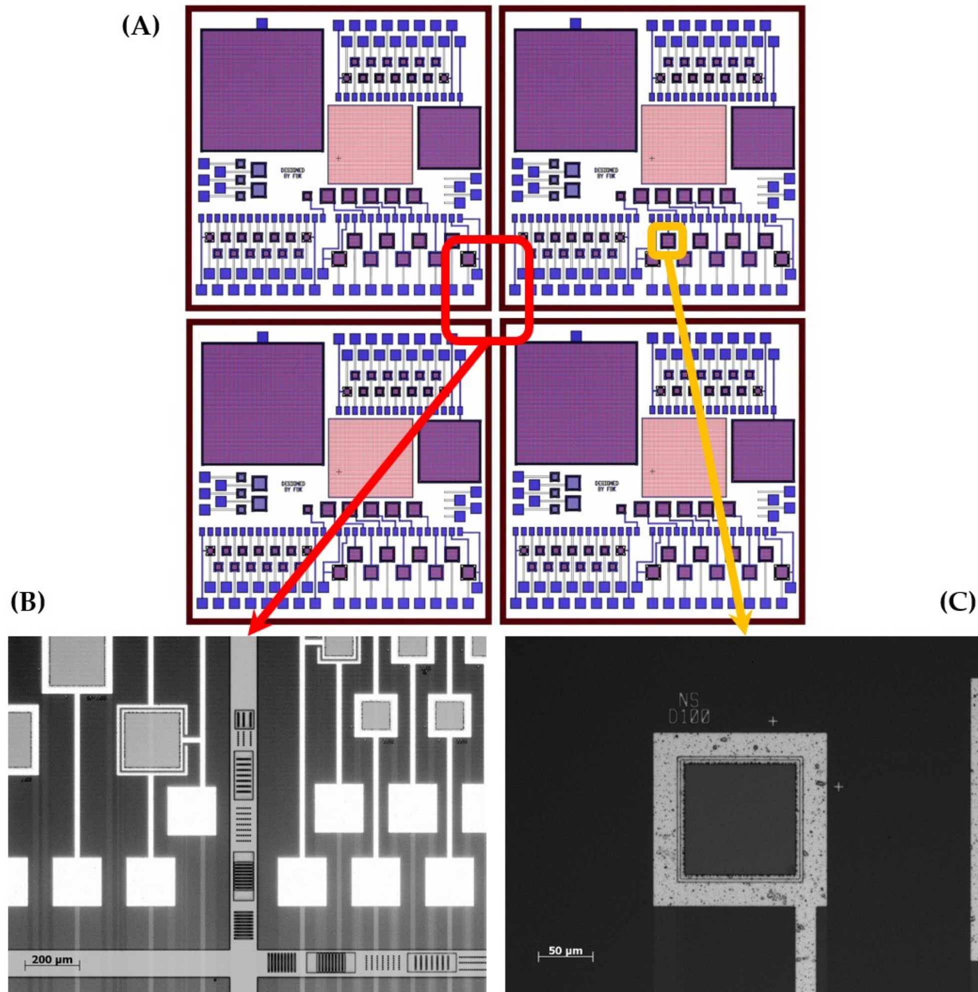


**Figure 4.4:** (A) Schematic representation of a substrate sample provided by FBK. Each sample can be divided into four identical "chips". (B) Optical microscope magnification of the central scribe lines (red area). (C) Optical microscope magnification of a 100x100 $\mu m^2$ photodiode (yellow area).

In order to measure the resist thickness homogeneity inside the active area of a photodiode, we use an Atomic Force Microscope (AFM) to image the largest photodiode active area of a sample substrate (2x2 $mm^2$) before and after spin-coating it with nominal ~600 nm of A7 (at 5000 rpm for 60 s).

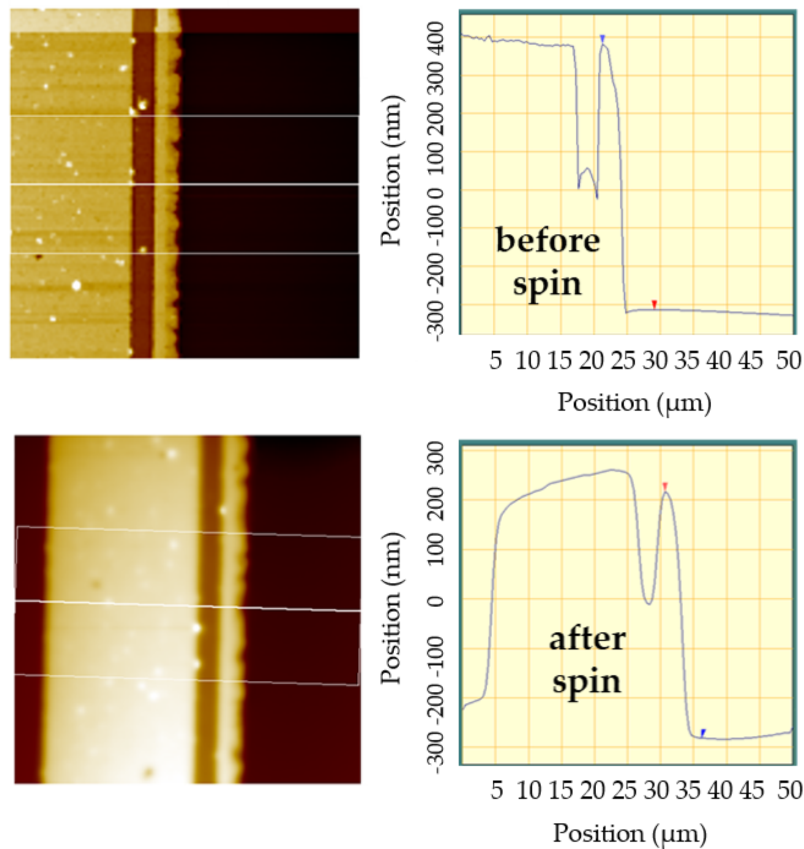


**Figure 4.5:** AFM images of a portion of the 2x2 mm$^2$ active area of a photodetector before (top) and after (bottom) spin-coating with ~600 nm of A7. The white rectangles delimit the measured regions.

As can be seen from Figure 4.5, inside the active area, near the border, where the height variance is the steepest due to the ~8µm thickness of the metal contacts surrounding the detectors, there are no significant differences between the surface homogeneity measured before and after the spin-coating process (both appear almost equally flat within the AFM resolution). Furthermore, there is no appreciable increase in resist thickness near the border that could have compromised the correct EBL patterning of the layer. On the other hand, on top of the metal contact, there is significant heterogeneity of the film thickness, which appears to progressively decrease going further from the active area. This could suggest a "protective" role of the tall metal contacts during the spin-coating process: the film inside the "protected" active area results more homogeneous than the "exposed" top region film. The effective film thickness inside the active area is measured by EBL over-exposition of a small 100x100 µm$^2$ square area (using an extremely high dose in order to remove all traces of A7 and exposing the active area at the bottom) and AFM imaging.

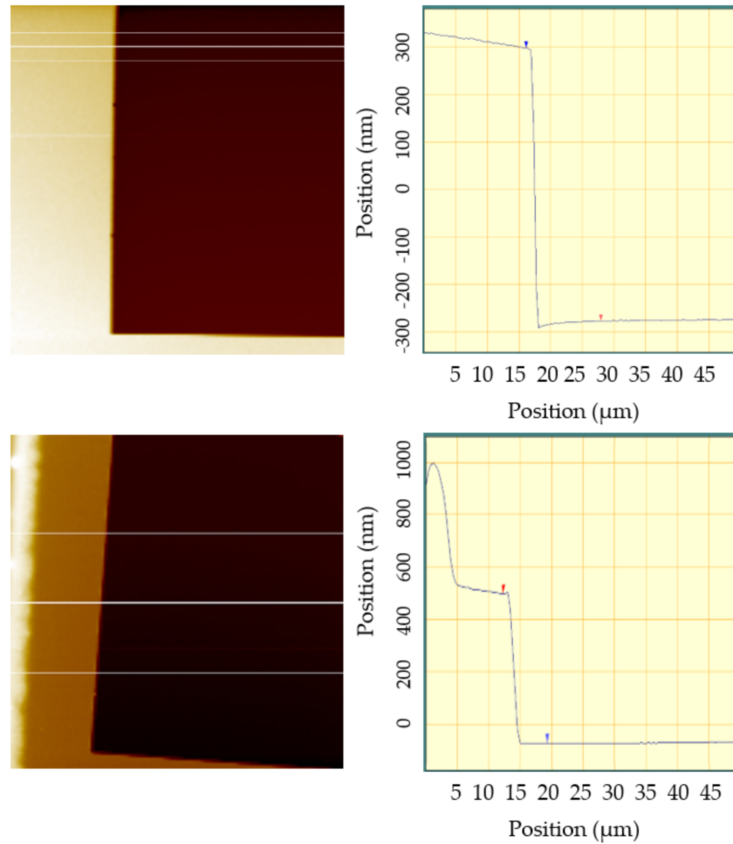


**Figure 4.6:** AFM images of an over-exposed 100x100 μm² area inside an active area spin-coated at 5000 rpm (top) and 6000 rpm (bottom). The white rectangles delimit the measured regions.

The resist layer thickness seems to be 580 nm for both typical spin-coating rotation speed of 5000 rpm and 6000 rpm. This is in complete agreement with the official A7 spreadsheet from MicroChem, which reports a ~600 nm thickness for a rotation speed higher than 4000 rpm (due to the plateauing of the A7 spin-speed curve). Since at 6000 rpm there is a higher chance that small debris on the surface of the photodetector and bubbles trapped inside the resist drop are removed, we choose this speed as our go-to spin-coating setting.

Before proceeding to the EBL exposition, the substrate must be carefully cleaned. This step is extremely important for maximizing the resist adhesion to the substrate and, especially, to avoid the detachment of the final silver nanodots array after the Lift-Off process. In fact, the adhesion strength of Ag onto silicon nitride (the passivation layer on top of the photodiodes' active areas) is greater than the average metal/dielectric adhesion strength but only if the surface is clean[167], otherwise the Ag tends to detach very easily without an adhesion layer (which we cannot use if we want to preserve the hybrid opt-plasmonic resonances and not lose too much light impinging on the active area silicon)[168–170]. The cleaning procedure starts with a 5 min bath in acetone, followed by a quick $N_2$ drying and another 5 min bath in isopropyl alcohol

(IPA) plus drying. The baths remove most of the organic residues accumulated on the surface of the substrates, as well as all residual debris left over from the cutting of the wafer. Finally, 5min on a hot plate at 200 °C desorbs most of the water vapor from the substrates surface, which compromises the adhesion of both the resist layer and the silver array. After 2-3 min of cooling back down at room temperature, the substrates are ready for being spin-coated. As previously mentioned, we spin-coat A7 for 60 s at 6000 rpm, in order to obtain a 580 nm film on top of the substrates. Then, before being loaded inside the EBL machine, the substrates are pre-baked at 180 °C for 60 s on a hot plate (to remove any residual solvent from the resist layer). The substrates are exposed with a 100 KeV (100 pA) beam for 3-12 h, depending on the size of the exposed area. The samples are then developed in a 3:7 solution of water/IPA for 60 s and rinsed for 30 s in pure deionized water (a 1:3 MBK/IPA solution can be a valid developer alternative, however, our tests found that, in this case, the development is less controllable/reproducible). A final post-bake at 100 °C for 60 s on a hot plate (the A7 will reflow at a temperature above 125 °C, destroying the pattern) completes the nanofabrication procedure.

The first pattern that must be drawn with the EBL is the so-called "Dose Matrix" (DM). A DM let us experimentally determine the correct dose that produces a pattern with features of the desired size (height and width). In our specific case, the DM is a 6x6 square array of grid patterns exposed with 36 different doses, ranging from 350 $\mu C/cm^2$ to 700 $\mu C/cm^2$, with a 10 $\mu C/cm^2$ step. The pattern CAD is designed with features 10% larger than the desired values (e.g. the lines are 146 nm wide, instead of 133 nm). This design let us use a higher dose in order to draw the pattern with features of the correct size, thus ensuring the complete clearing of the resist within the holes of the grid pattern and the exposure of the photodiode active area below.

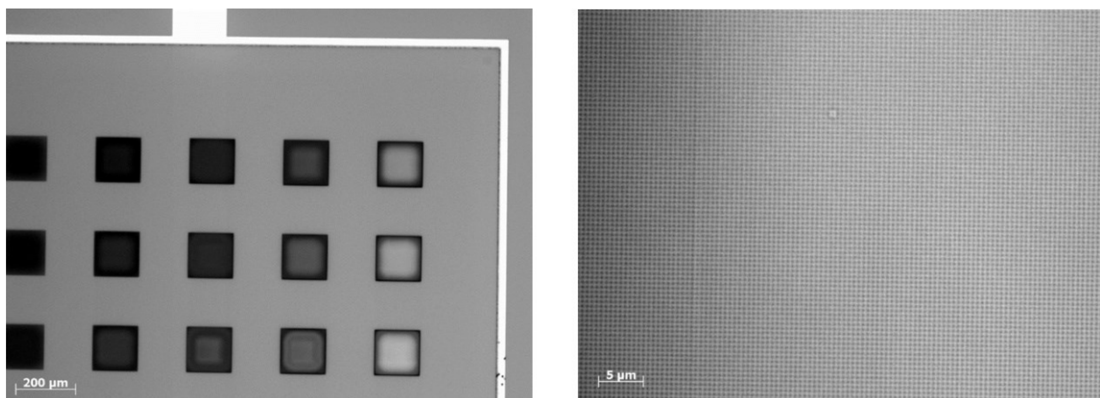


**Figure 4.7:** Example of optical microscope images of a DM. The 6x6 square array is patterned inside the active area of a 2x2 $mm^2$ photodiode (left), each square being a grid pattern exposed with a different dose (right). The "shades" inside each square are due to the lack of correction for the proximity effect.

Since we want to know precisely the dose given to each grid pattern, no proximity effect correction is applied to the DM. This leads to a variable dose within each pattern, which assumes the "correct" value at the center of the pattern and progressively decreases going towards the edges. Therefore, any measurement must be performed only inside the central area of the grids. In order to study the patterns of the DM, we use a sputtering machine to coat the samples with 3 nm of gold (Au) and then we use an SEM microscope to analyze them. The Au coating ensures that there is enough contrast to see the details of the patterns with the SEM microscope (the PMMA does not scatter much the electrons coming from the SEM beam) while also increasing their electrons exposure resistance (a "naked" pattern would deteriorate too quickly to perform any analysis). Figure 4.8 shows some examples of patterned substrates examined by SEM.

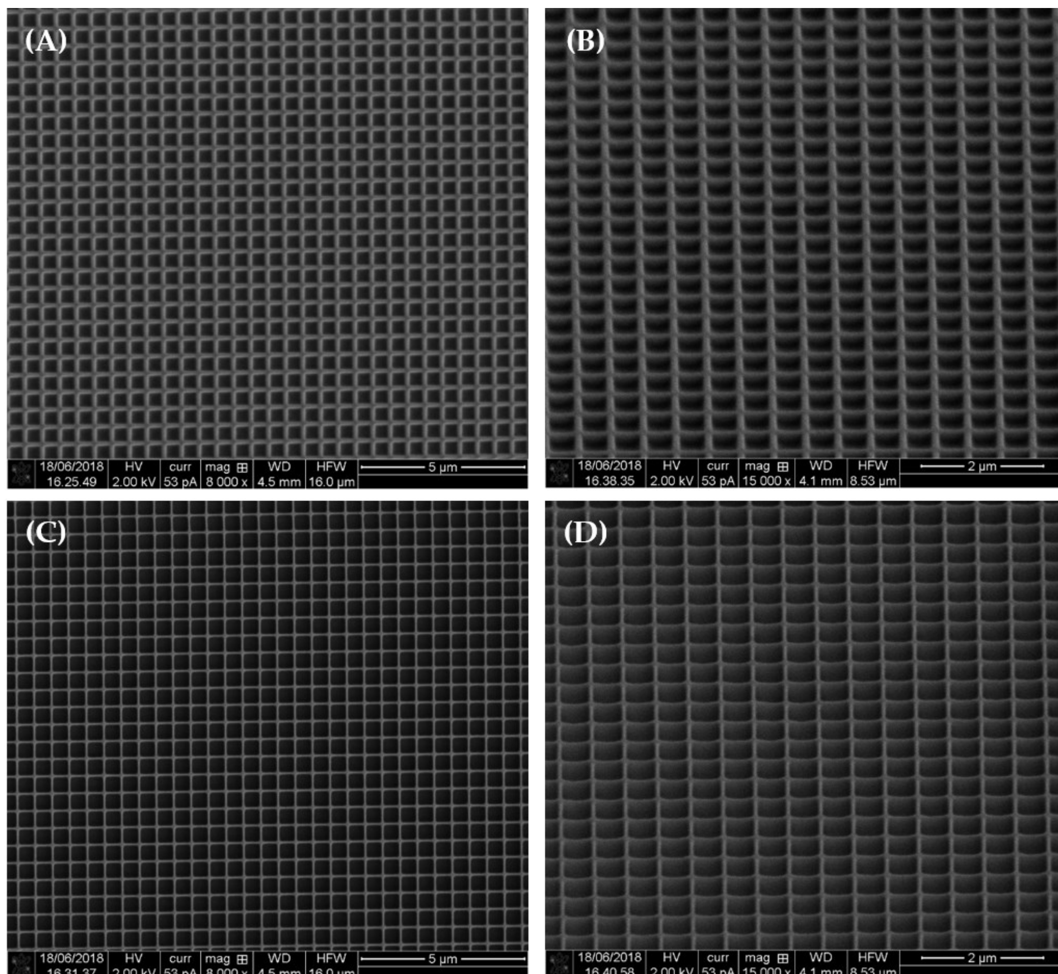


**Figure 4.8:** (A) SEM image of the grid pattern exposed with a dose of 350 µC/cm². (B) SEM image of the same grid pattern, but with a 45° inclination. (C) SEM image of the grid pattern exposed with a dose of 650 µC/cm². (B) SEM image of the same grid pattern, but with a 45° inclination.

From the SEM analysis, we find that the correct dose range for obtaining a grid pattern with a 25% DC and an aspect ratio of four is 650-660 $\mu C/cm^2$. As previously mentioned, we also confirm, that the grid pattern can sustain itself, without collapsing, even with an aspect ratio greater than three.

Established the working dose of 655 $\mu C/cm^2$, we follow the same procedure to nanofabricate some samples that will continue to the next fabrication step, the metal deposition and Lift-Off. However, since these samples will be our enhanced photodetectors prototypes, we cannot neglect the proximity effect. As mentioned in the previous paragraph, back- and forward-scattering can contribute significantly to the absorbed energy in a resist area that is far from the initial point of exposure, leading to increased energy absorption for large, closely spaced features and relatively lower absorption in small, isolated features. This means that, for a given dose, some structures are over-exposed or are larger than they should, while some others are under-exposed. This is known as "proximity effect"[171,172] and must be corrected with an *a priori* dose correction (before the exposure). The easiest way to correct for the proximity effect is to assign different doses to different features, depending on their size and proximity to other features[173]. However, this correction requires some trial and error before achieving good enough results and is mostly useful for large, complex patterns. Better results can be obtained by thinking about the correction as an inverse problem, setting the desired absorbed energy for each feature and then determining the operations (e.g. modulation of the dose assigned to each feature, change in size or shape of the pattern) on the initial data that give the best approximation (this process is often fully automated). Usually, the approximation parameters are calculated by inversion of the convolution model of the exposure[174]. Assuming the Point Spread Function (PSF, the distribution of the energy deposited inside the resist from a single point of incidence) invariant along the z-axis, the energy absorbed in a plane is given by the convolution:

$$\mathbb{E}(x, y) = D(x, y) \otimes f(r) \tag{4.3}$$

where $D$ is the given dose and $f(r)$ is the proximity function at half the depth of the resist, which can be used in a 2-dimensional calculation to simplify the problem when the resist layer is thin or the energy of the electron is high (as in our case). The PSF can be accurately modeled using a sum of two Gaussian functions, one with standard deviation $\alpha$ that represents the forward scattering broadening, and one with standard deviation $\beta$ that represents the backscattering effect[168,170]. Setting the desired pattern $\mathbb{E}_{desired}(x,y)$ and calculating the proximity-corrected dose $D_{corrected}(x,y)$, it is possible to solve Eq. 4.3 for $D$ using the fundamental property of Fourier transforms for which the transform of a convolution between two functions is equal to the product of the transforms of the two functions:

$$D_{corrected}(x,y) = F^{-1}\left\{\frac{F\{\mathbb{E}_{desired}(x,y)\}}{F\{f(x,y)\}}\right\} \quad (4.4)$$

Using software that can calculate Eq. 4.4 from the CAD file with the grid pattern design and the starting dose of 655 $\mu C/cm^2$, we successfully correct the proximity effect (see Figure 4.9).

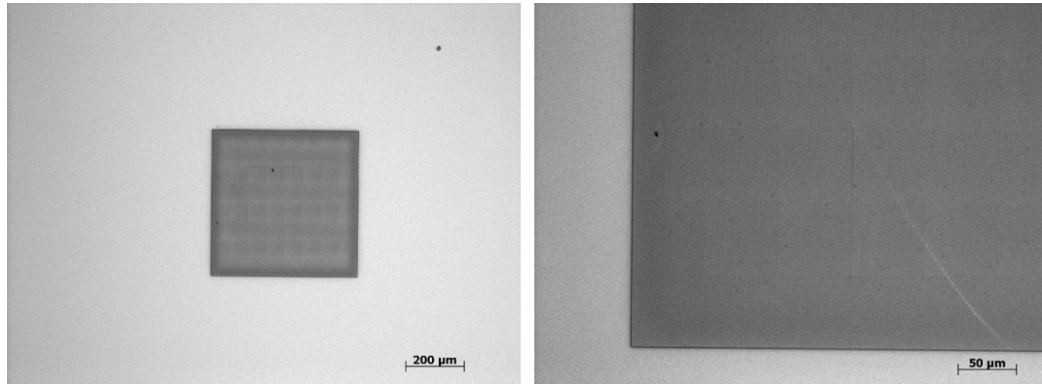


**Figure 4.9:** optical microscope images of a 655 $\mu C/cm^2$ grid pattern corrected for the proximity effect. The dose remains constant up to the edges of the pattern and no over-exposition(under-exposition) can be seen.

Having corrected for the proximity effect, we proceed to nanofabricate a few samples of grid patterns on top of several 200x200 $\mu m^2$ that will be the base for the metal deposition/Lift-Off step. Since our EBL machine does only have a back-scattered electrons detector and the FBK substrate shows poor scattering properties (including the aluminum metal contacts), the alignment between the grid pattern exposure areas and the active area of the detectors must be "manually" made with the aid of a SEM module included inside the EBL and a (temporarily) current of 700 pA (because the Al markers can't be automatically recognized by the machine, due to the extremely low scattering signal). Some examples of the final patterned active areas can be seen in Figure 4.10. Inevitably, a small misalignment between the patterns and the active areas is present (~3-7 µm). However, a misalignment of less than 3% of the total area cannot compromise the functioning of the future prototype.

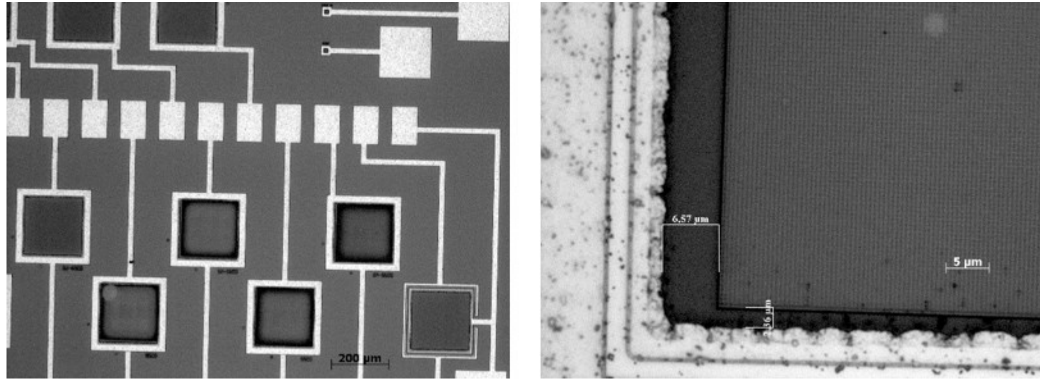


**Figure 4.10:** optical microscope images of four grid patterns (ranging from 625 μC/cm² to 715 μC/cm²) on top of four different 200x200 μm² photodetectors. The misalignment is very small with respect to the total covered area.

## 4.3 Metal Deposition and Lift-Off

We use a vacuum deposition chamber to evaporate 115 nm of Ag on top of our patterned photodiodes (deposition rate of 1.5 nm/s). The sample holder inside the chamber is kept stationary because the standard planetary motion would increase too much the degree of conformity of the deposition and we would have problems to strip the residual resist layer. After the evaporation, the samples are kept in an acetone bath at 40 °C for 40-90 min in order to completely remove the resist layer (and the Ag deposited on top of it) and reveal the final nanodots array pattern (Lift-Off).

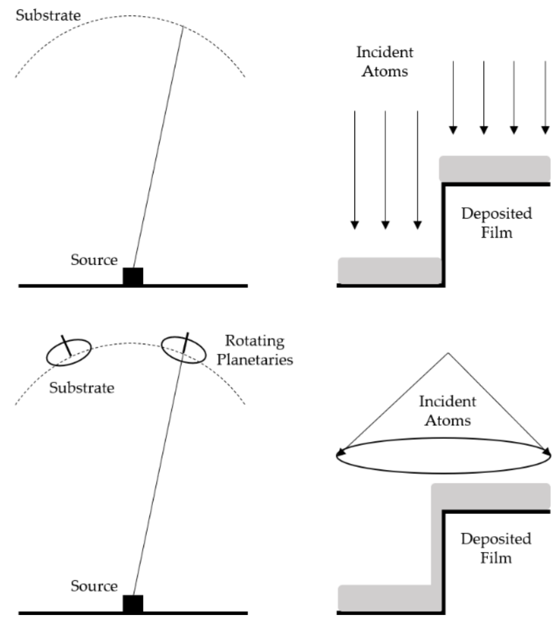


**Figure 4.11:** Schematic representation of the metal evaporation process with and without the planetary rotation of the substrate holder.

After the Lift-Off, we examine the resulting arrays with a SEM microscope, finding that we can achieve up to 85% DC without any pattern degradation, except for a slight (~10 nm) asymmetry of the dots along the x and y perpendicular directions (which can be associated with a slight difference in the exposure times across the two directions during the EBL processing step, due to the beam scanning method).

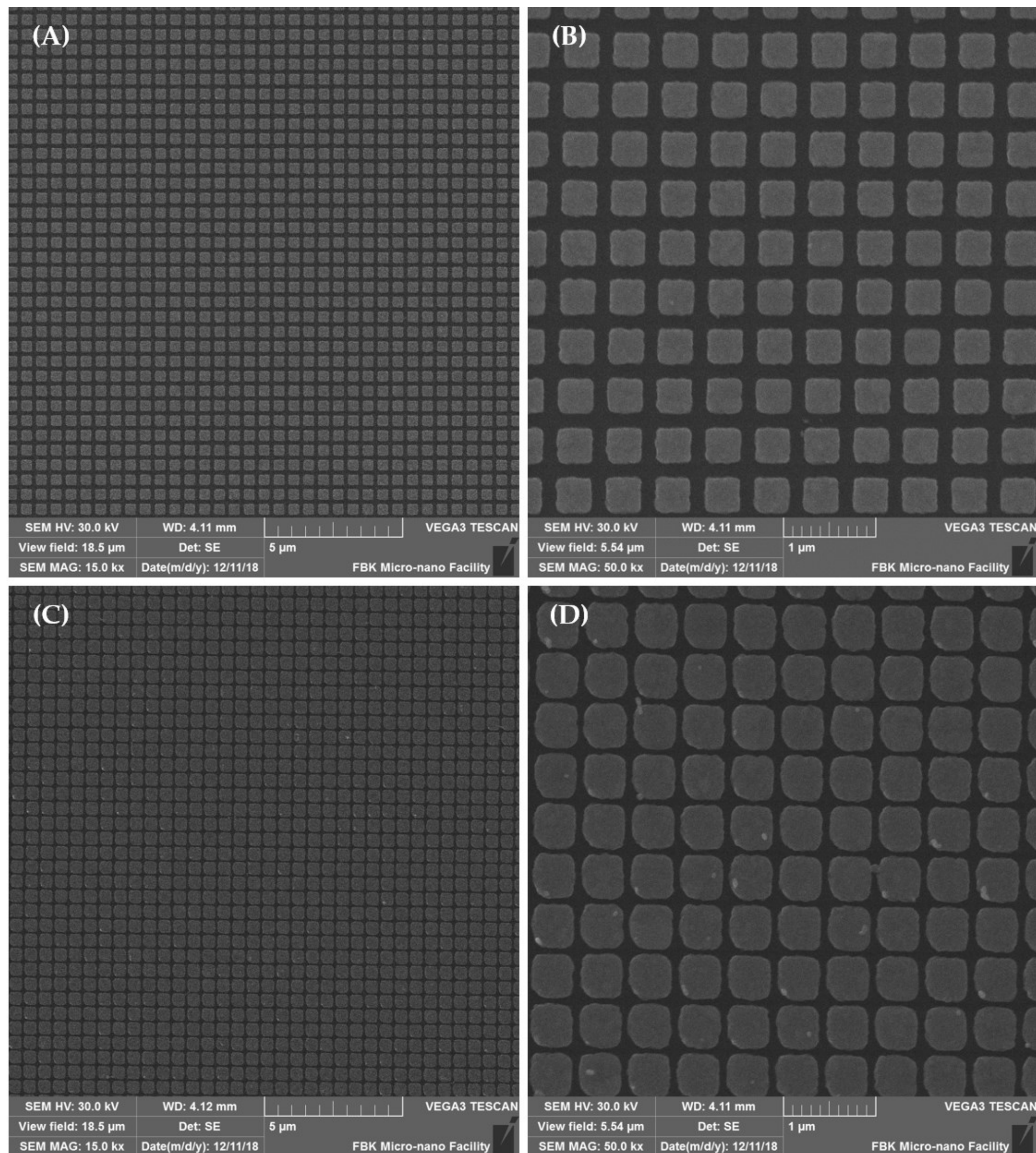


**Figure 4.12:** (A) SEM image of an Ag nanodots array with 75% DC. (B) SEM image of a detail of the same array. (C) SEM image of an Ag nanodots array with 85% DC. (D) SEM image of a detail of the same array.

Achieved a good result after the metal deposition/Lift-Off process, we proceed to the capping of some devices with a 200 nm PMMA layer (instead of the more common silica capping) in order to prepare them for the electro-optical characterization. A $SiO_2$ capping layer would require a complex, multi-step

procedure in order to open the metal contact pads of the photodiodes to perform any kind of electrical characterization (another spin-coated resist layer and EBL patterning over the pads areas plus an etching step). On the other hand, a PMMA cap only requires a spin-coating plus EBL patterning in order to expose the metal pads. Obviously, the protection efficiency of the PMMA must be carefully tested in order to prove it as a valid alternative to the $SiO_2$, as we did not find any previous example of this application in literature. The required thickness of PMMA is determined by COMSOL simulations and obtained by mixing A7 and A2 into a 1:1 ratio solution and spinning it at 4500 rpm for 60 s. Before the spin-coating, another "de-gassing" step at 200 °C for 5 min (plus 3 min of cooling down) can be performed in order to remove the water vapor from the Ag/substrate surface.

# Chapter 5

# Device Characterization

In this chapter, we want to describe the characterization process of our enhanced prototypes. In §5.1 we describe the electro-optical characterization of several different photodiodes and we show that we actually achieved an increase in performance with respect to standard silicon diodes. Then, in §5.2 we describe the procedures we used in order to obtain an accurate measurement or estimation of the most important structural parameters of our silver arrays. Finally, in §5.3 we talk about the difference between intrinsic silicon and doped silicon used in real p-i-n diodes and how to properly estimate its dielectric permittivity.

## 5.1 Electro-Optical Characterization

We characterize the performance of our prototype using a custom developed optical setup (see Figure 5.1). This setup uses a halogen lamp as the (unpolarized) light source and a grating monochromator to choose the light wavelength impinging on the samples. The light exiting the monochromator passes through a variable aperture slit, which is set to select a bandwidth of 3 nm around the desired wavelength. This defines the wavelength resolution of the characterization setup. The samples are mounted on a 3D moving holder that grants a precise positioning of the prototypes with respect to the incident light beam. In order to perform any kind of electro-optical characterization, the FBK enhanced photodiodes must be packaged on an appropriate PCB (printed circuit board). These supports have 24 pins that can be connected to the moving holder and bonded to up to 20 photodiode metal contacts per sample. The remaining 4 pins are "reference" pins that are used as the second electrode for the electrical measurements. The bonding between the metal pads and the PCB pins is made *via* thin gold filaments. The substrates are glued to the PCB using epoxy glue and a thermal curing process at 80 °C. Once the PCB pins are connected to the holder, the responsivity (as well as the quantum efficiency) of each individual prototype (as well as one "naked" photodiode per substrate) can be calculated connecting two copper filaments (one for the prototype pin and one for the reference pin) to an oscilloscope and using an in-house developed acquisition software written in LabView. No bias is applied to the photodiodes. Responsivity spectra are acquired as a function

of the incident wavelength, within the 450-1100 nm range. These spectra can be compared to the expected simulated results calculated by COMSOL.

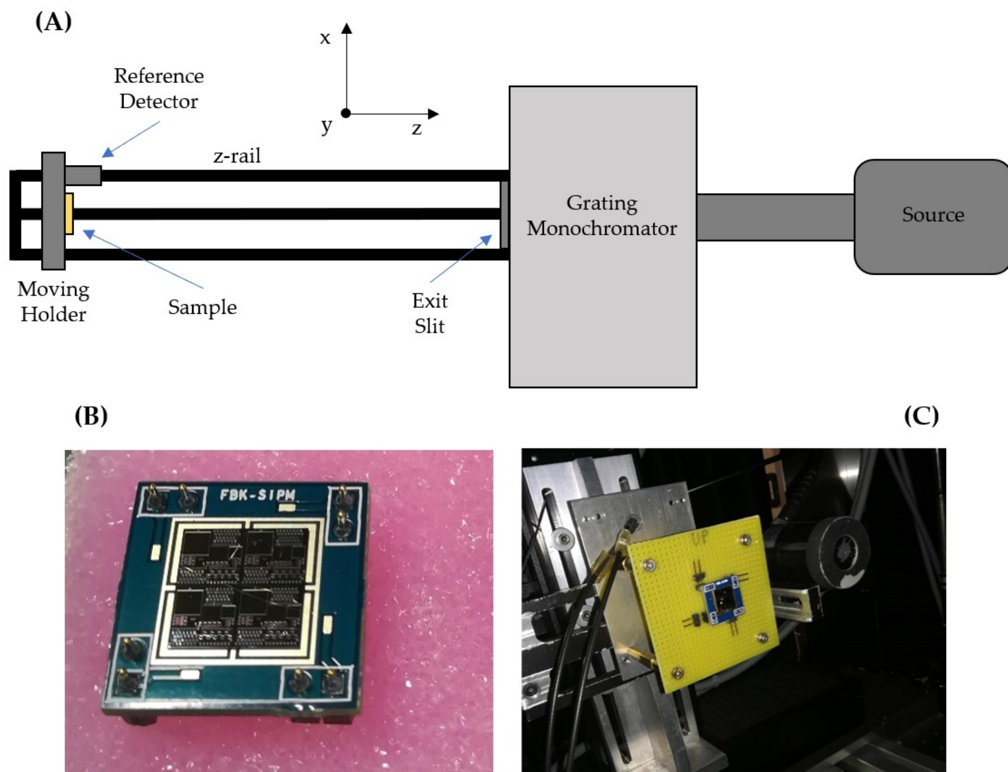


**Figure 5.1:** (A) Schematic representation of the electro-optical characterization setup. The reference detector, of known quantum efficiency and responsivity, is used for calculating the efficiency and responsivity of the samples. (B) Photo of a packaged FBK patterned substrate. (C) Photo of a sample positioned on the sample holder.

After characterizing several enhanced photodetectors, we report in Figure 5.2 three different cases of measured performance. The photodiodes reported in Figure 5.2 have these characteristics:

1. **W5.02** → p = 530 nm (nominal), DC = 75%, hAg = 115 nm (nominal), $hSi_3N_4$ = 11 nm, hCap = 200 nm (nominal).

2. **W6.01** → p = 530 nm (nominal), DC = 68%, hAg = 115 nm (nominal), $hSi_3N_4$ = 6.6 nm, hCap = 200 nm (nominal).

3. **W8D** → p = 530 nm (nominal), DC = 75%, hAg = 115 nm (nominal), $hSi_3N_4$ = 11 nm, No PMMA capping.

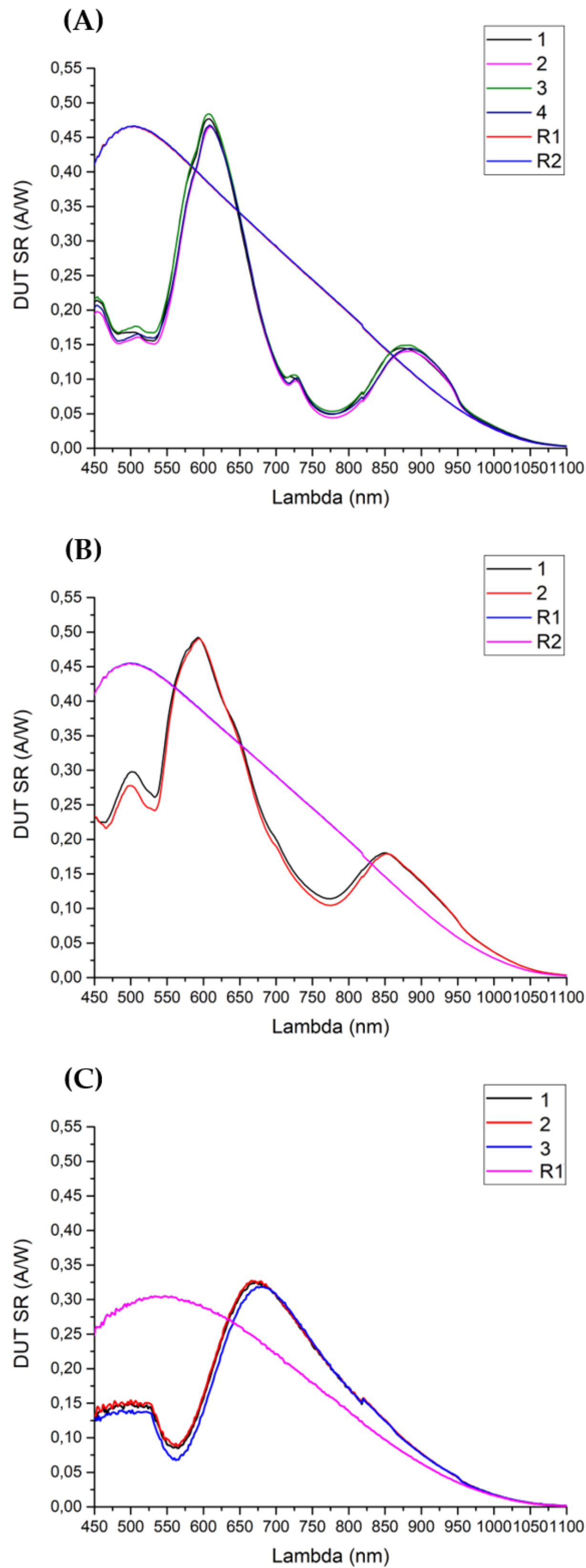


**Figure 5.2:** (A) Measured responsivity of W5.02 photodiodes. (B) Measured responsivity of W6.01 photodiodes. (C) Measured responsivity of W8D photodiodes. R1 and R2 are un-patterned FBK photodiodes for reference performance.

Enhanced photodiodes in W5.02 and W6.01 show an increase in performance at 950 nm of ~50% with respect to the "naked" reference photodiodes, while the photodiodes of W8D without the PMMA protective cap show no significant increase in performance due to a complete lack of resonance at 950 nm (as expected from the quick Ag oxidation and tarnishing in atmosphere). The polarization independence of the enhanced devices can be verified rotating by 90° in-plane the samples and repeating the responsivity measurements.

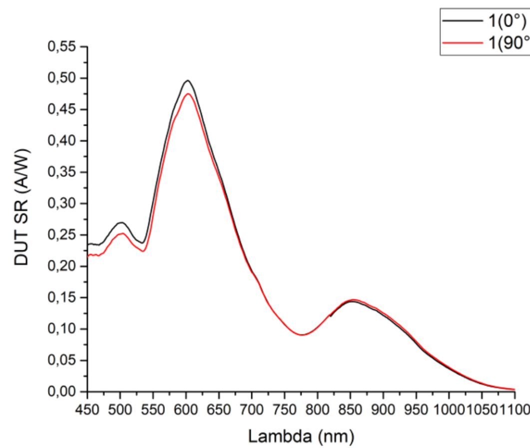


**Figure 5.3:** Responsivity measurement of W5.02 photodetector n°1 with two perpendicular in-plane orientations.

As can be seen from the example of Figure 5.3, there are no significant differences between the responsivities measured with the two perpendicular orientations, thus confirming the complete polarization independence of the devices (see Chapter 3 for the description of unpolarized light). Furthermore, repeating the responsivity measurements after four months can validate the PMMA efficiency as a protecting capping layer for the Ag arrays.

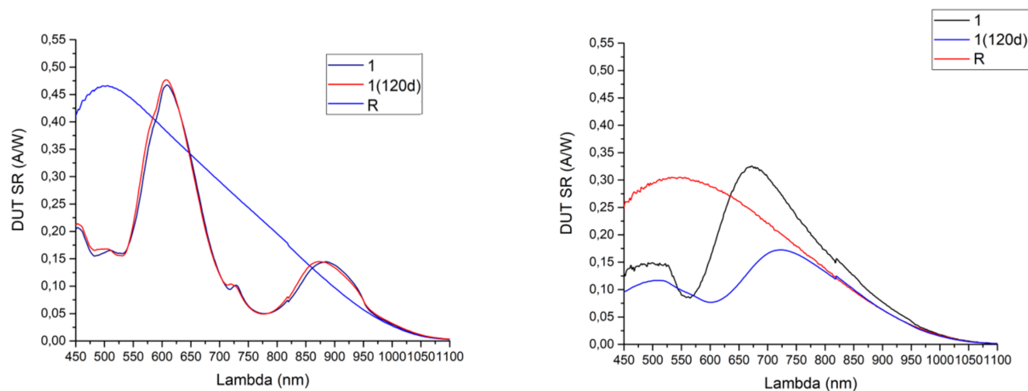


**Figure 5.4:** Responsivity measurements of photodetector n°1 and a "naked" reference of W5.02 (left) and W8D (right). While the performance of W5.02 does not change after four months, the unprotected W8D drastically decreases in responsivity.

Measuring the performance of the enhanced photodiodes after 120 days shows us that the PMMA capping is efficiently preventing di Ag nanodots from oxidizing (being the responsivity unchanged). This behavior is further confirmed considering the drastic decrease in responsivity of the unprotected photodiodes of W8D, whose performance falls below that of a traditional silicon photodiode.

An increase of ~50% in responsivity is very significant, but still far from the simulated values. Furthermore, observing the spectral responsivity plots, no sign of the narrow hybrid opto-plasmonic resonance can be found, except for a small "shoulder" at 950nm. If we confront the COMSOL simulations with the experimental data and another set of simulations performed using the Finite Difference Time Domani method (FDTD)[175], we find a reasonable agreement for an array structure with p ~ 540 nm, DC = 67%, hAg = 107 nm, $hSi_3N_4$ = 11 nm, hCap = 227 nm (see Figure 5.5, simulations assume 100% collection efficiency inside the depletion region and 0% outside).

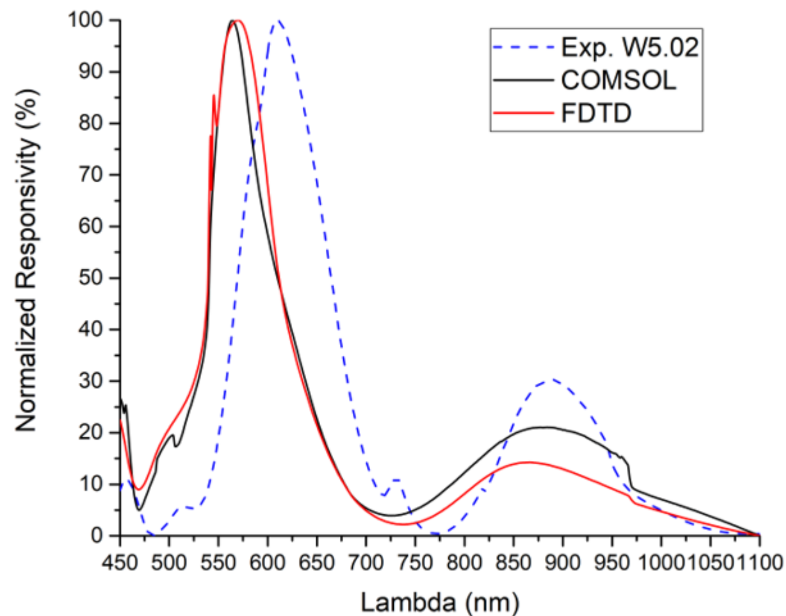


**Figure 5.5:** Comparison between the experimental responsivity curve of W5.02 (blue dashed curve), the COMSOL simulated responsivity (black curve) and the FDTD simulated responsivity (red curve).

The position of the simulated peak at ~900 nm almost perfectly fits the experimental data, however, there is a significant difference between the positions of the lowest wavelength simulated and experimental peak. This shift can be understood by studying the responsivity spectrum changes as a function of the possible array structural parameters variations.

The effect of each structural parameter on the responsivity spectrum can be seen in Figure 5.6.

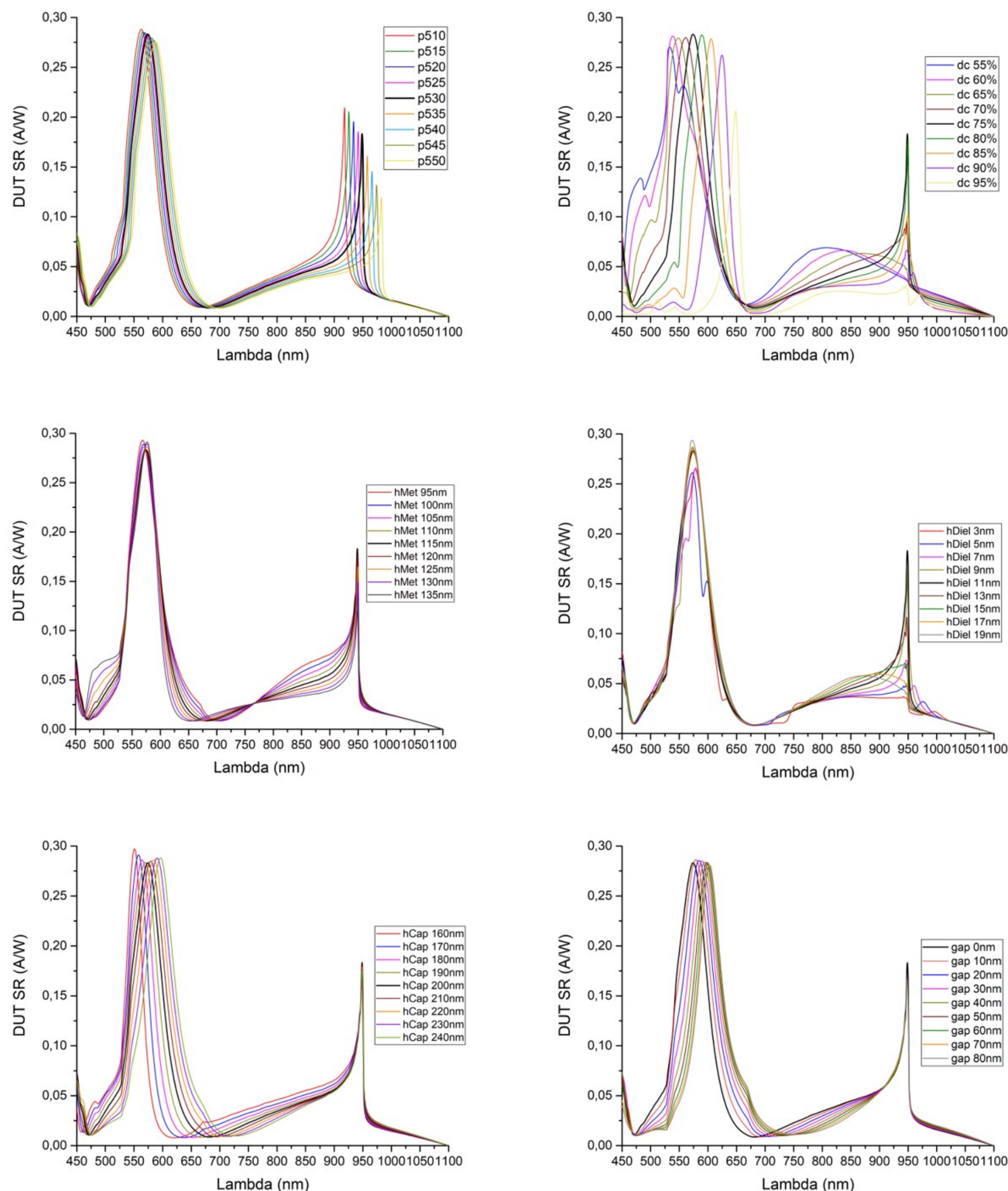


**Figure 5.6:** Changes in the spectral responsivity due to variations of each possible array structural parameter.

With "gap" we mean a small separation between the PMMA capping layer and the bottom of the Ag nanodots array apertures. If a gap exists there, it means that the PMMA is not directly in contact with the passivation layer below the silver array. This is a reasonable condition since the small apertures into which the polymer must flow during the spin-coating deposition cannot be realistically filled completely, due to the action of the adhesion and cohesion forces. Taking into consideration the possible existence of such a gap,

we can simulate again the spectral responsivity and achieve a better fitting with the experimental data (using an 80 nm gap).

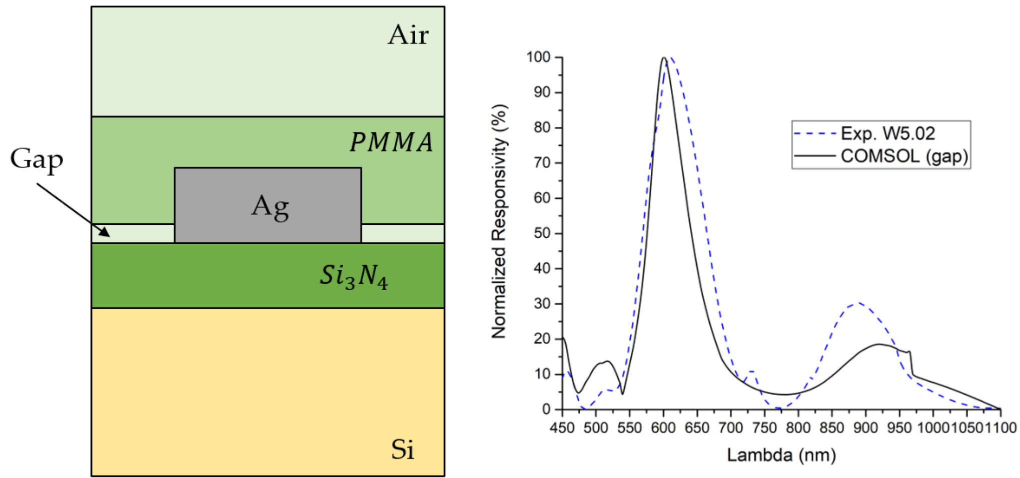


**Figure 5.7:** Schematic representation of an enhanced photodiode with a "gap" between the PMMA capping layer and the passivation layer below the nanodots array (left), and comparison between the simulated "gap" structure and the experimentally measured responsivity of W5.02 (right).

If we study the fields at different wavelengths of the simulated responsivity spectrum, we can find three interesting conditions, corresponding to the two maxima and the minimum at ~775 nm (see Figure 5.8).

The first maximum at ~600 nm corresponds to a tri-matched mode (see Chapter 3) without any hybrid resonance being excited along the lower

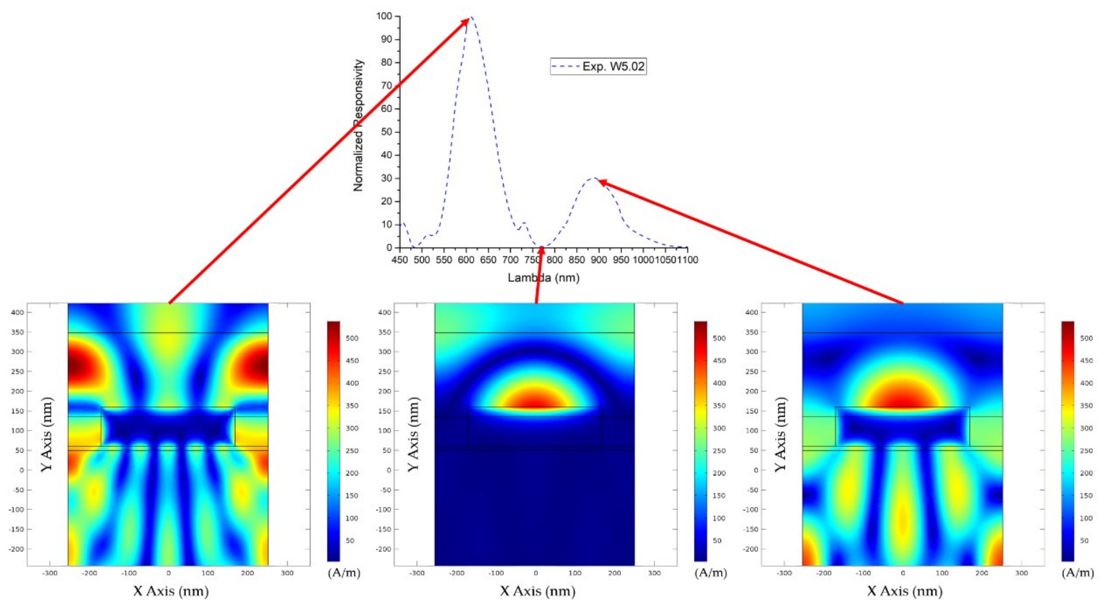


**Figure 5.8:** Magnetic field norm plots corresponding to the two maxima and the minimum of the spectral responsivity of W5.02.

interface of the array. The other maximum at ~900 nm corresponds to another tri-matched mode (the upper interface excited surface plasmon is different from that of the first maximum). Finally, the minimum at ~775 nm corresponds to the excitation of a pure surface plasmon mode on the PMMA/Ag interface (almost all the incident light is absorbed and dissipated by the plasmon and the metal, drastically reducing the light impinging on the detector active area). The vanishing of the hybrid resonance seems to be mostly due to a wrong value of DC. However, in order to be certain that the simulated structural parameters are really compatible with the actual Ag arrays, we need to carefully measure each one of them experimentally.

## 5.2 Array Structural Parameters Measurements

The easiest parameter to measure is the capping layer thickness. After spin-coating a cleaned "blank" substrate (a piece of silicon wafer) with our 1:1 A7/A2 solution at 4500 rpm for 60 s, we use an ellipsometer in order to estimate the thickness of our PMMA layer. The estimated thickness is 220 nm, which is perfectly compatible with the value required in order to achieve a proper fit between the simulated responsivity and the experimentally measured responsivity.

Next, we proceed to accurately measure the height of the evaporated silver using Secondary Ion Mass Spectroscopy (SIMS). We deposited on two $Si_3N_4$/Si substrates a silver film of 110 nm nominal thickness *via* vacuum deposition, using two different recipes: the standard recipe (StdR), with a 1.5 nm/s deposition rate, and a slow recipe (SloR), with a 0.1 nm/s deposition rate. The SIMS analysis is carried out in $MCs^+$ mode, using cesium ions ($Cs^+$) as primary ions and collecting positive secondary ions formed by the atoms of interest and the re-sputtered $Cs^+$ ions. This methodology is supposed to be less affected by matrix effects (i.e. variations of secondary ion intensity due to ion and sputtering yield changes and not linearly linked to composition). Therefore, it is particularly suited for multilayer and interface characterization, especially in cases where the precise composition is unknown. The main drawback is the relatively poor detection limit. Primary ion impact energy, intensity and rastering area are optimized to have an adequate depth resolution and data density. The measurements are carried out using the Zalar rotation (the sample rotates around an axis normal to the surface and centered on the sputtered crater). This approach is expected to reduce the ion beam-induced roughness during the analysis. In order to measure the deposited Ag thickness, the Ag sputtering rate (SR) is estimated by stopping the SIMS analysis at the Ag/$Si_3N_4$ interface and then measuring the crater depth *via* a mechanical stylus profilometer. We do not apply any correction for the expected different sputtering rates inside the $Si_3N_4$ layer and

the Si substrate, since these portions of the depth profile are not relevant to the aim of the analysis. The adopted experimental conditions are:

- Primary Beam: $Cs^+$
- Source Potential: 8 kV
- Primary Beam Impact Energy: 1 keV
- Primary Beam Intensity: 21 nA
- Secondary Ion Polarity: (+)
- Monitored Species: $^{133}Cs^{14}N^+$, $^{133}Cs^{16}O^+$, $^{133}Cs^{28}Si^+$ and $^{133}Cs^{107}Ag^+$
- Sample Bias: 5 kV
- Rastered Area: 350x350 $\mu m^2$
- Sputtering Rate: 0.11 nm/s
- Analyzed Area: 80x80 $\mu m^2$
- Mass Resolution: 400
- Rotating Stage: ON (20 rpm) and OFF
- Chamber Pressure: ~$10^9$ mbar

Figure 5.9.A shows two profiles obtained on a SloR sample with identical beam conditions but with (continuous lines) or without (dashed lines) rotation during sputtering. It is evident that the use of rotation during the SIMS sputtering improves the quality of the measurements at the interface between Ag and $Si_3N_4$. In fact, the interface is less wide and better defined. This means that the sample rotation significantly reduces the roughness induced by the action of the ion beam. However, the silicon nitride film itself does not appear as well defined. This is probably mainly due to the metal film topography (the rotation during the analysis probably reduces it but without eliminating it). A better estimation of the $Si_3N_4$ layer quality can be obtained by SIMS analysis of a reference sample, simply made of nitride on silicon (see Figure 5.9.B).

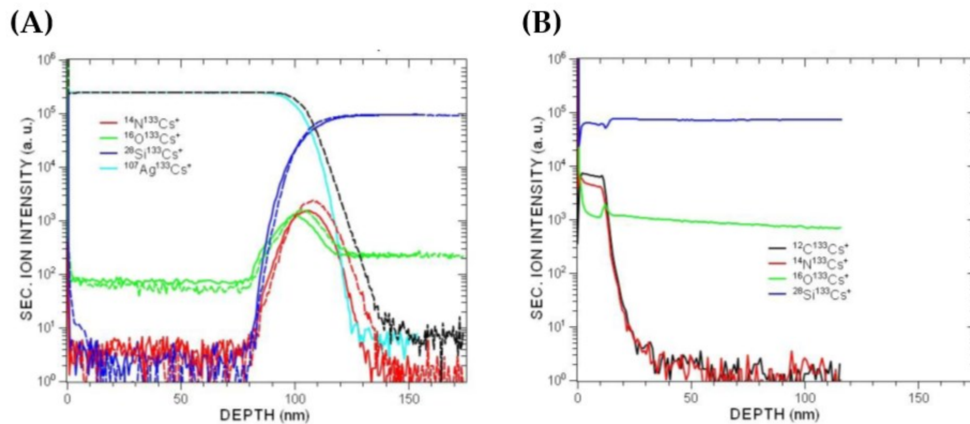


**Figure 5.9:** (A) SIMS profile of a SloR sample, obtained with (continuous curves) or without (dashed curves) rotating the sample holder. (B) SIMS profile of a $Si_3N_4$/Si reference sample.

We can prove the good reproducibility of the measurement by repeating the SIMS analysis another time, obtaining the same profile as the first time (see Figure 5.10). Repeating the measurement also helps us identify an interesting superposition between O- and N-related peaks inside the nitride region, probably due to partial surface oxidation of the original $Si_3N_4$ layer.

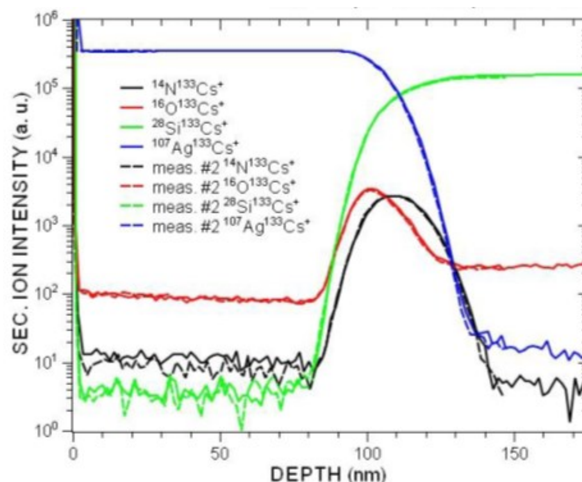


**Figure 5.10:** SIMS profile of a SloR sample, measured two times in order to verify the reproducibility of the SIMS analysis.

A similar analysis is carried out on the StdR sample, obtaining a very similar element distribution profile. The main difference arises from the $^{133}Cs^{107}Ag^{+}$ profile.

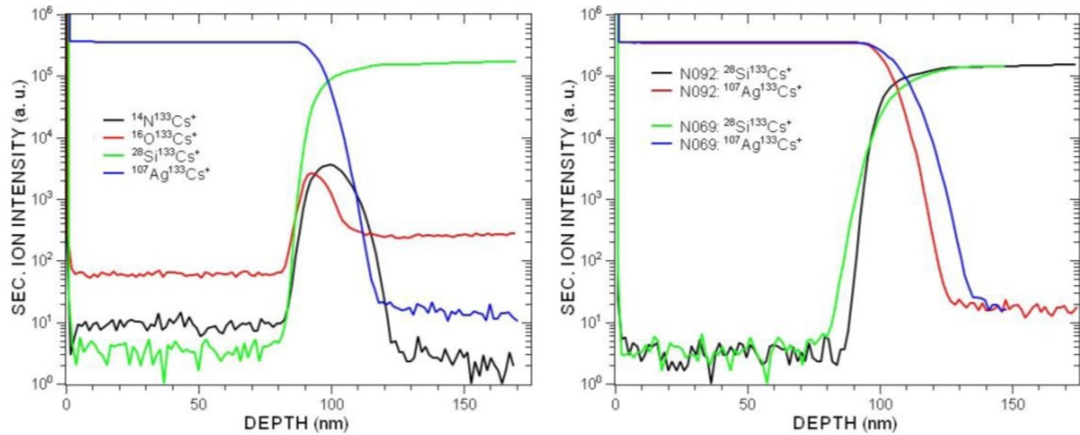


**Figure 5.11:** SIMS profile of a StdR sample (left) and comparison between the SloR and StdR $^{133}Cs^{107}Ag^+$ and $^{133}Cs^{28}Si^+$ profiles (right).

Estimating the Ag thickness using the $^{133}Cs^{107}Ag^+$ signal at 50% intensity over multiple (2-3) SIMS measurements, leads us to:

- StdR Ag thickness: (99±5) nm
- SloR Ag thickness: (105±6) nm

The wider interface for the SloR sample can be associated with a rougher crater bottom, probably due to higher initial surface roughness. This hypothesis can be confirmed directly measuring the root mean square roughness *via* AFM. The rms roughness of StdR and SloR are ~1.5 nm and ~5.5 nm.

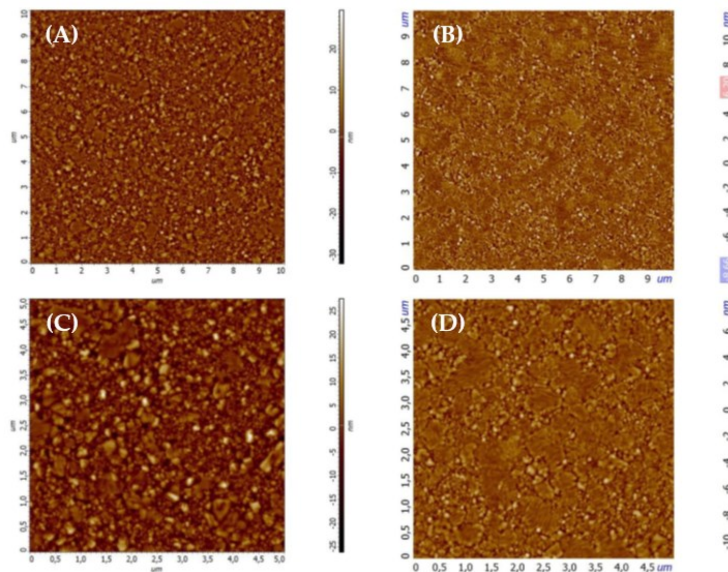


**Figure 5.12:** Comparison between surface topographies of the SloR sample (A) and StdR sample (B), measured *via* AFM over a 10x10μm² area. The same comparison, but over a scanned area of 5x5μm², is reported below (C-D). Note the z-scale difference between the two samples, being much larger for the SloR.

From these results, we can say that an average over-estimation of ~10 nm should be expected for our enhanced photodiodes samples, which had the silver layer evaporated using the StdR recipe. Again, like with the capping layer thickness, the measured Ag thickness seems to be compatible with the simulated thickness.

The last two structural parameters that we need to measure are DC and *p*. Both can be estimated by SEM analysis of the W5.02 enhanced photodiodes. From this analysis (using Gwyddion™ as the measurement software), the average DC and period of W5.02 photodiodes seem to be:

- (X-axis) p = (540±2) nm , DC = (74±1) %
- (Y-axis) p = (530±3) nm , DC = (75±1) %

As previously mentioned, the array appears to be slightly asymmetrical (*p* and DC are different along the two in-plane perpendicular axes). This asymmetry complicates the comparison between the measured data and the simulated values (at the moment, not enough computational power is at our disposal to perform 3-D simulations with different x and y periodicities with a sufficiently fine mesh). Having a structure with two different periodicities, also means that there are different coupling conditions to be satisfied in order to successfully excite a Type 2 Wood's anomaly along the two perpendicular axes. This could translate into a potentially severe destructive interference between the two anomalies. While we can acknowledge a degree of compatibility regarding the *p* values (especially considering that the larger x-axis period probably has a big role in the measured performance reduction), the measured DC cannot really be considered compatible with the simulated 67% DC.

# 5.3 Doped Silicon Versus Intrinsic Silicon

Another possible cause for the reduced performance enhancement of the patterned photodiodes could be the discrepancy between the complex refractive index of intrinsic silicon, considered during the simulations, and that of the p-doped silicon of the p-i-n diodes, near the surface of the active area. From the literature, we know that, for highly doped silicon ($N_{dop} \approx 10^{20}$), as in the case of shallow p-doped region of the photodiode, we can say that "free-carriers effects" are the cause for any change in the silicon dielectric function (both real and imaginary part) within the visible[176] (~495-830 nm) and IR[177–179] (~1200-20.000 nm) wavelengths ranges (assuming completely ionized dopants[179]). Hypothesizing that this behavior can be extended also up to ~1000 nm, change in the silicon dielectric function within a range of 500-1000 nm can be described in terms of the Drude equation[172-175]:

$$\varepsilon_{dop}(\omega) = \varepsilon_{Si}(\omega) - \frac{\omega_p^2}{\omega(\omega + i\gamma)} \tag{5.1}$$

where $\varepsilon_{Si}$ is the dielectric function of intrinsic silicon, $\omega_p$ is the plasma frequency and $\gamma = e/m^*\mu$. Dividing Eq. 5.1 into its real and imaginary parts, we obtain:

$$\varepsilon_{1\,dop}(\omega) = \varepsilon_{1\,Si}(\omega) - \frac{Ne^2}{\varepsilon_0 m^*(\frac{e^2}{\mu^2 m^{*2}} + \omega^2)} \tag{5.2.1}$$

$$\varepsilon_{2\,dop}(\omega) = \varepsilon_{2\,Si}(\omega) + \frac{Ne^3}{\varepsilon_0 m^{2*}\omega\mu(\frac{e^2}{\mu^2 m^{*2}} + \omega^2)} \tag{5.2.2}$$

where *N* is the dopants density, *e* is the electron charge, $m^*$ is the effective mass of the main carriers (holes, for p-doped silicon) and $\mu$ is the carrier mobility. At high doping levels, the holes effective mass is $m^* \cong 0.37m_0$ ($m_0$ is the holes standard mass)[177–180], while the holes' mobility is $\mu \cong 40\ \mathrm{cm^2/Vs}$[179,181]. From Eq. 5.2.1 and Eq. 5.2.2 we can estimate the complex refractive index of the doped silicon:

$$n_{dop}(\omega) = Re\left(\sqrt{\varepsilon_{dop}(\omega)}\right) \tag{5.3.1}$$

$$k_{dop}(\omega) = Im\left(\sqrt{\varepsilon_{dop}(\omega)}\right) \tag{5.3.2}$$

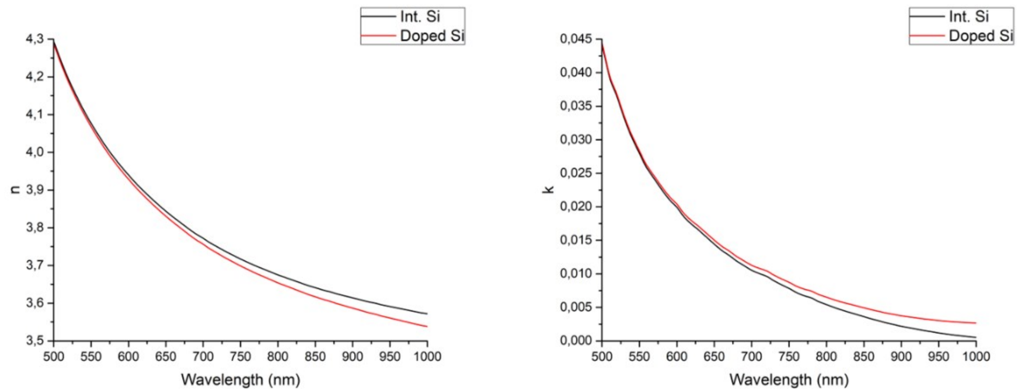


**Figure 5.13:** Comparison between the refractive index (left) and extinction coefficient (right) of intrinsic silicon and p-doped silicon.

Figure 5.14 shows the comparison between the original simulated and experimental spectral responsivities of Figure 5.7, and the simulated responsivity spectrum using p-doped silicon as the photodiode active area.

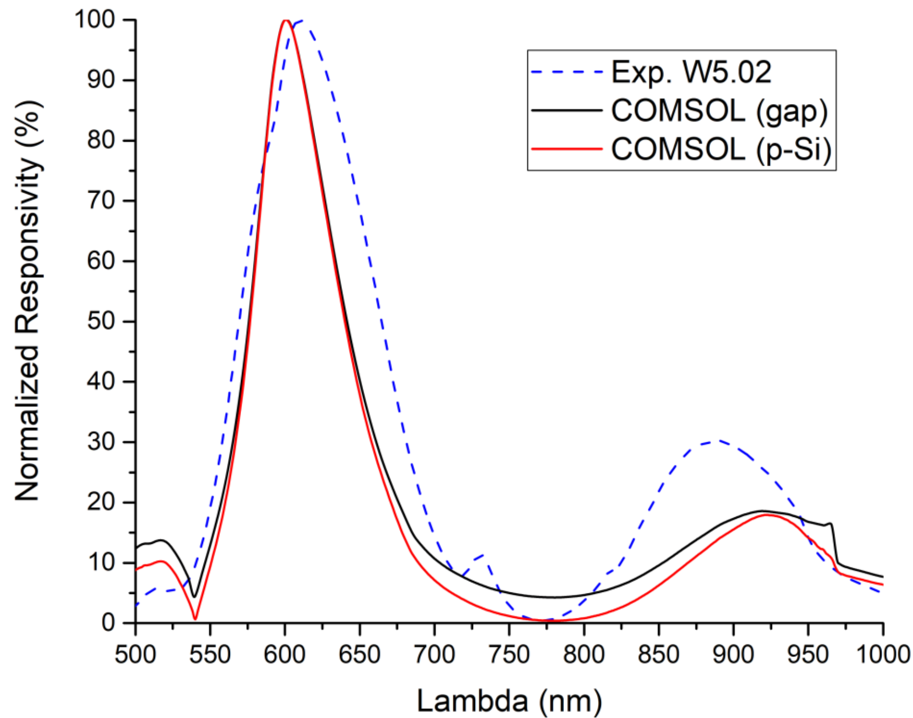


**Figure 5.14:** Comparison between the experimental W5.02 data (blue dashed curve), the COMSOL simulation with intrinsic silicon (black curve) and the COMSOL simulation with p-doped silicon (red curve).

The overall spectrum profile seems to become more fitting with the experimental data considering a p-doped silicon layer of ~200 nm, both in terms of normalized responsivity (especially the responsivity minima) and peak shape (at ~900 nm). Since the real doping profile consists of ~100 nm of highly doped Si plus ~300-400 nm of moderately doped Si, our simulation seems to be a decent approximation of the real device silicon. It is, however, clear that this effect alone does not account for all the discrepancies between the expected enhancement and the real increase in performance. Some other, more complex, behaviors must exist inside our devices that can more effectively manipulate both the resonances and the spectral responsivity. Further studies are needed in order to achieve a further increase in performance.

# Chapter 6

# Nonlinear Optical Detection

In this chapter, we present our designed multi-modal microscope, capable of performing simultaneously TPM and HG without any kind of compromise thanks to two, separate, individually optimized laser sources with axial chromatic aberration compensation. In §6.1 we briefly introduce a few key concepts for nonlinear optical microscopy and label-free microscopy, and we describe in detail our custom setup. Then, in §6.2 we talk about the applications of our setup to the examination of a plethora of ex vivo samples in order to prove its capabilities and the significant advantages of a multi-modal approach. Finally, in §6.3 we describe the materials and methods used during our experiments with the multi-modal microscope.

## 6.1 Introduction and Setup Description

Multiphoton Microscopy (MPM) is a Laser-Scanning Microscopy technique based on a non-linear, strongly localized excitation of fluorescence. The "non-linear" nature of the process derives from the dependence of the absorption rate on a higher power of the illumination intensity. MPM does not have its optical sectioning capabilities severely limited by the fluorescence contributions from outside the depth of focus of the objective (as in Wide-Field Microscopy) and, therefore, represents one of the best non-invasive techniques to achieve imaging in deep explanted tissues or in living animals[182,183]. The most common MPM variation is the Two-Photon Microscopy (TPM), which takes advantage of the quasi-simultaneous absorption of two photons by a molecular receptor, in a single quantum event. This phenomenon was theoretically predicted by Maria Goeppert-Mayer in 1931[184] but could be experimentally verified only after the advent of mode-locked lasers. Furthermore, the physical phenomenon of Two-Photon laser Excitation (TPE) laid dormant until Denk et al. devised a practicable Two-Photon Laser-Scanning fluorescence Microscope[178]. The TPE rate depends on the second power of the incident light intensity and is ~$10^{-14}$ times smaller than the Single-Photon Absorption rate; hence, the successful implementation of TPM imaging requires very high photon fluxes, which in practice translates into the use of mode-locked laser sources with pulse durations below 1ps and frequencies of ~100 MHz. Despite the need for very intense light sources, TPM

presents several advantages over the classical single-photon techniques. For example, the wavelengths used in TPM, which usually range from Near-IR to Mid-IR, are significantly less prone to scattering and absorption from thick specimens (with respect to visible light) and, therefore, exhibit longer penetration depths. Furthermore, due to the small TPE focal volume generated by the high photon fluxes required to achieve Two-Photon Absorption[178], TPM has an inherent capability of performing axial sectioning and confines the photo-bleaching effect inside a very limited volume[185]. The lateral resolution of TPM scales (for high numerical aperture objectives) as:

$$R_{MP}(NA > 0.7) = \frac{0.383\lambda_{ex}}{NA^{0.91}} \tag{6.1}$$

where $\lambda_{ex}$ is the excitation wavelength and $NA$ is the objective numerical aperture. Despite the obvious benefits of TPM, there are cases where it cannot (or should not) be applied. When specimens are very susceptible to photo-bleaching and photo-damage, even with NIR excitation wavelengths, or when any staining process must be avoided in order to preserve the specimens in their original conditions (e.g. in case of multi-techniques examinations), the use of another non-linear light/matter interaction based technique, known as Harmonic Generation (HG), is preferable. HG retains the intrinsic optical sectioning capabilities of TPM but, usually, does not involve the absorption of the excitation light, producing very little heat and resulting in a much less photo-toxic approach. Furthermore, HG does not require the use of molecular probes in order to generate and detect signals from a specific biological feature: any structure that satisfies the prerequisites for at least one order of Harmonic Generation can produce a detectable HG signal, thus drastically reducing the specimen preparation requirements and induced alterations. The most commonly used orders of Harmonic Generation are the Second Harmonic Generation (SHG) and Third Harmonic Generation (THG), which, respectively, doubles and triples the incident light frequency and produce a narrow band at half and one-third of the excitation wavelength. SHG has a quadratic dependence on the input laser intensity and originates only from media without inversion symmetry (e.g. tissues made of chiral molecules[186–188]), while THG has a cubic dependence on the input intensity (higher average powers required) but, in principle, can be elicited from any material to a varying degree. However, from a practical point of view, a detectable THG signal originates mainly from interfaces between media with a significant difference between their refractive indexes, like lipids immersed in aqueous fluids[189–191], cellular membranes[192,193] and protein aggregates[193,194]. The resulting signals scale as follow[195]:

$$SHG \propto \frac{(p \cdot \chi_2)^2}{\tau} \quad ; \quad THG \propto \frac{(p \cdot \chi_3)^3}{\tau^2} \tag{6.2}$$

where p is the input power, $\chi_2$ and $\chi_3$ are the susceptibility coefficients of the second and third order, and $\tau$ is the laser pulse width. Both SHG and THG are very sensitive to external factors (e.g. temperature, medium ionic strength, pH, etc.) that can alter, even slightly, the molecular structures from which the signal originates[191]. Therefore, careful optimization of the experimental parameters must be performed on a sample basis in order to achieve the best possible HG experimental conditions. Here, we report on the design and realization of a multi-modal microscope capable of performing both TPM and HG simultaneously thanks to two separate laser sources that can be independently optimized for one technique or the other. We also report on the use of our microscope for the study of several thin and thick ex vivo samples, in order to show the quality and quantity of complementary information that can be extracted through a multi-modal approach.

The main laser source is a mode-locked Ti:Sapphire pulsed laser (Chameleon Ultra II, Coherent Inc.), with pulses of ~140 fs at 80 MHz and tunable emission wavelength of 700–900 nm, which also serves as a pump for the second laser source, an Optical Parametric Oscillator (Compact OPO, APE) with tunable emission wavelength in the 1000–1550 nm range. Both lasers pass through a pair of Pockels Cells, voltage-controlled wave plates that combined with a polarizer can modulate the laser beam power with up to 100 kHz frequency (360-80 and 350-80, ConOptics Inc.). Two mechanical shutters are used as hard beam-blocking devices (SH05/M, Thorlabs Inc.). A couple of silver-coated mirrors (PF10-03-P01, Thorlabs Inc.) deflect them to the recombination area, where they are spatially overlapped by means of another silver mirror (PF10-03-P01, Thorlabs Inc.) and a dichroic mirror (DMSP1000, Thorlabs Inc.) mounted on piezo-controlled kinematic mirror mounts (POLARIS-K1PZ, Thorlabs Inc.). Two telescopes (#59-134, Edmund Optics) are used for the axial chromatic aberration compensation. Both telescopes have a 3x magnification in order to increase the diameter of the beams from 2.5 mm to 7.5 mm. The larger diameter, in combination with another 3x magnification from the scanning unit optics, allows for a slight overfill of the objective back-aperture (22 mm). From the recombination area, the beams enter the scanning head (Bergamo Series, Thorlabs Inc.), equipped with a scan lens/tube lens couple (SL50-2P2 and TL200-2P2, AR coating and color correction range 680-1600 nm) and a Galvo/Resonant scanner (8 kHz scanning rate) and arrive on the sample through a water-immersion objective (XLPLN25XWMP2, Olympus, NA 1.05, water immersion, color corrected up to 1300 nm). The polarization state of both laser beams can be controlled independently by two achromatic $\lambda/4$ Wave Plates preceded by two achromatic $\lambda/2$ Wave Plates (AHWP05M-600/-980 and AQWP05M-600/-980, Thorlabs Inc.), which can compensate the polarization variations induced by the optical components in the scanning head in order to achieve the desired polarization state before the

objective back-aperture with an high grade of purity. The light scattered or emitted from the sample is collected in epi-direction and, thanks to a longpass dichroic mirror (705 nm cutoff, Semrock), is diverted to the detection module. This module consists of 4x GaAsP PMT detectors (H7422-40, Hamamatsu), with bandpass filters (395/25 nm Chroma, 460/50 nm Chroma, 525/40 nm Semrock, 625/90 nm Semrock) spectrally separated by 3x dichroic mirrors (425 nm Chroma, 495 nm Chroma, 565 nm Chroma). The transmitted light can be collected by a condenser lens (D-CUO Achr-Apl, 1.4 NA, Nikon) and detected by a biased InGaAs detector (DET20C, Thorlabs Inc.) positioned below the sample holder. We keep a constant laser power across all experiments of 10mW for the pump and 15 mW for the OPO (measured on the objective back-aperture). A schematic representation of our setup can be seen in Figure 6.1.

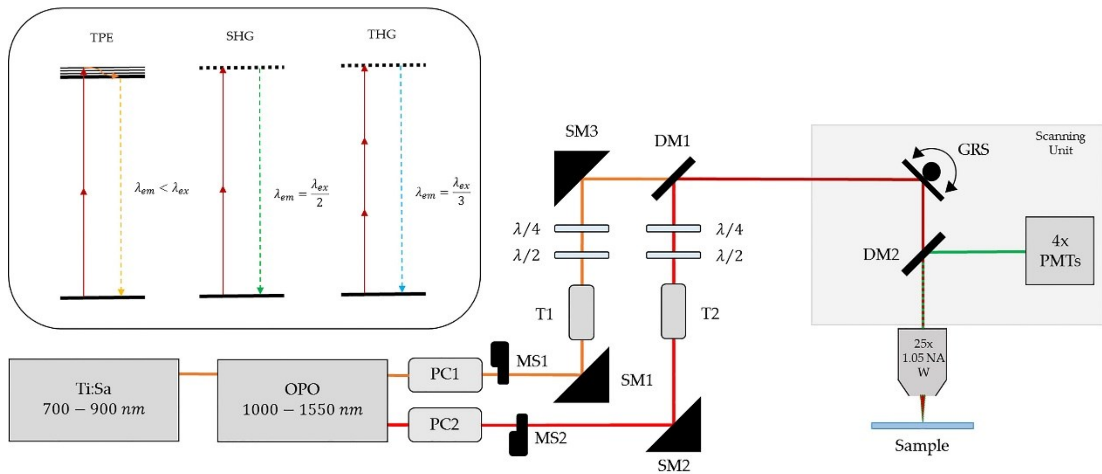


**Figure 6.1:** Schematic representation of the setup. Both laser beams coming from the Ti:Sa laser and the OPO are modulated in intensity by two Pockels Cells (PC1,PC2), circularly polarized by a couple of Half-Wave Plates and Quarter-Wave Plates ($\lambda/2$,$\lambda/4$), spatially overlapped by means of a silver mirror (SM3) and a dichroic mirror (DM1) mounted on piezo-controlled kinematic mirror mounts, and finally focused on the sample through a 25x Objective. The fluorescence and HHG signals are detected in epi-direction and sent to four GaAsP PMT detectors thanks to another dichroic mirror inside the scanning unit (DM2). Two telescopes (T1, T2) are used for the axial chromatic aberration compensation. Two mechanical shutters are used as hard beam-blocking devices (SH05/M, Thorlabs Inc.). Two silver mirrors (SM1, SM2) deflect the beams to the recombination area.

In order to optimize the polarization state for both laser beams and achieve the best possible quality of image, we position a polarization analyzer (SK010PA-NIR, Schäfter+Kirchoff) under the scanning-head of the microscope to measure the polarization before the back-aperture of the objective and we rotate a couple of $\lambda/2$ Wave Plate and $\lambda/4$ Wave Plate (AHWP05M-600/-980 and AQWP05M-600/-980, Thorlabs Inc.), setting the polarization of both lasers to circular. A circular polarization ensures the highest signal for the Auto-

Fluorescence emission due to the generally random orientation of the intrinsic fluorophores' dipole axis[196] while also maximizing the SHG signal for randomly oriented collagen fibers. If the collagen structures of some samples happen to have a preferred orientation, the polarization state can be easily switched to a linear polarization and aligned to be at 45° from the fibers, which is the orientation of maximum SHG signal generation[197,198]. The polarization state is then checked using a commercial calibration sample (F24630, Thermofisher), following the procedure described by X. Chen et al.[199]. The depolarizing effect of the objective seems to be not significantly affecting the circular polarization state on the sample plane, at least for our purposes. In case of high precision measurements, specific interest over slight variations of the polarization state or 3D-polarization imaging, a much more precise control would be needed, requiring complete mapping of in-and-out polarization[200,201].
A known major issue of dual-wavelength excitation is chromatic aberration. In order to fully compensate for the axial chromatic aberration, we choose an objective with a reported color correction up to 1300 nm (XLPLN25XWMP2, Olympus), as well as a pair of scan lens/tube lens (SL50-2P2 and TL200-2P2) color corrected in the 680-1600 nm range, and we adopt a procedure commonly used in STED Microscopy, where perfect overlapping of two beams focal volumes is a strictly required condition[202–204]. Following the STED procedure, we fine-tune the axial aberration via a couple of telescopes (#59-134, Edmund Optics) positioned right before the Wave Plates in the beams optical paths, which allow us to shift the two focal volumes along the z-axis by slightly changing the curvature radii of the two beams, thus obtaining a high precision superposition. We also correct the lateral focal volumes displacement by carefully superimposing the two Point Spread Functions (PSFs) via a silver mirror (PF10-03-P01, Thorlabs Inc.) and a dichroic mirror (DMSP1000, Thorlabs Inc.) mounted on piezo-controlled kinematic mirror mounts (POLARIS-K1PZ, Thorlabs Inc.). We measure the two PSFs by imaging a sample of PbS Quantum Dots (average diameter 70 nm, up to ~1300 nm 2p-Absorption, ~650 nm Emission) dispersed in a sol-gel $ZrO_2$ matrix. We check the status of the axial chromatic aberration and the lateral displacement iteratively through the analysis of several z-stack of the PSFs using a custom-developed software (see Figure 6.2).

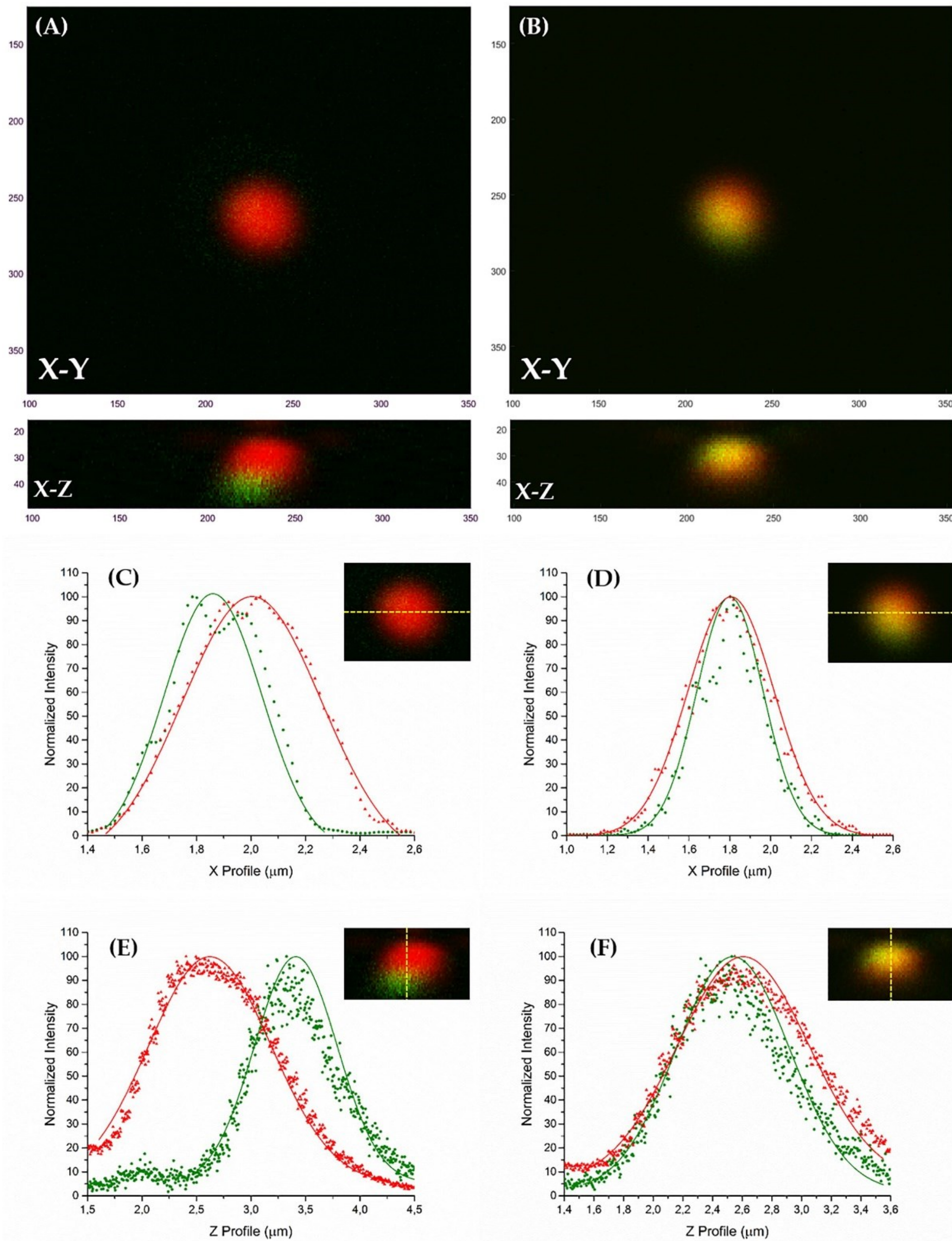


**Figure 6.2:** PSFs displacement comparison before and after correction. (A) PSFs displacement in the X-Y (top) and X-Z (bottom) planes before fine-tuning. (B) PSFs displacement in the X-Y (top) and X-Z (bottom) planes after fine-tuning. (C) and (E) show the X and Z profiles of the two PSFs before fine-tuning, while (D) and (F) show their profiles after fine-tuning (the insets show qualitatively the direction of the profiles). The final lateral displacement is (5 ± 7) nm, thus negligible, while the residual axial displacement is (112 ± 48) nm, well below the minimum requirements for simple Multiphoton Microscopy. Axis scales express coordinates in pixels (4.17 nm/pixel X and Y, 100 nm/pixel Z).

The software controls two mechanical shutters (SH05/M, Thorlabs Inc.) via an Arduino microcontroller board (Arduino MEGA, Arduino) connected to the shutters' controllers (KSC101, Thorlabs Inc.). The open/close cycles of the shutters are synchronized with the z-stack acquisition process in order to perform simultaneously two z-stack at two different wavelengths, minimizing any possible mechanical drift contribution to the determination of the PSFs relative position, achieving very high precision. The synchronization is done by registering 60 separate frames for every z-plane of a z-stack that extended about 2 μm below and above the approximate position of the two PSFs (z-plane separation of 0.4 μm) and timing the aperture/closure of the mechanical shutters in order to have 20 frames of background signal (both shutters closed), 20 frames of a PbS QD illuminated by one beam and 20 frames of the same PbS QD illuminated by the other beam. Afterward, we can import the frames of a z-stack inside the software, selecting properly the ranges associated with the background and the two beams, and obtain a highly precise 3D representation of the relative position of the two PSFs. After careful fine-tuning, we achieve a full 3D PSFs superimposition, with a negligible residual lateral displacement and an axial displacement of < 200 nm, near the minimum requirement for STED applications[205]. Through the previously described procedure, we can fully compensate for the axial chromatic aberration; however, a recent study[206] showed that there is a non-negligible contribution to image degradation also from the transverse chromatic aberration, which varies within the field of view, up to ≈ 1.5 μm at the edge of the field of view (FOV 484x484 μm). We do not compensate for this type of chromatic aberration; however, we are planning to do so in future works.

## 6.2 Label-Free Analysis of Biomedical Samples

In order to test the quality of the obtainable images after the polarization calibration, we image mice heart cryosections at 800 nm and 1200 nm, using both laser beams (see Figure 6.3). The cryosections show an overall high signal intensity and very good S/N ratio for both Auto-Fluorescence Emission and Harmonic Generation (SHG/THG). Many different features can be observed in cardiac cryosections without any labeling procedure. Remarkably, sarcomeres' myosin, as well as collagen deposits surrounding the coronary vessel, are clearly distinguishable due to their strong SHG signal from both 800 nm and 1200 nm excitation wavelengths. We evaluate the intensity profile of the SHG signal produced by the sarcomeres: it has a very good S/N ratio (Figure 6.3.D) and, in line with the previous reports[197], appears to arise from the myosin of thick filaments. Moreover, elastin can be visualized simultaneously by TPE. The excitation wavelength of 1200 nm does not show some of the sample features that are clearly visible from the Auto-Fluorescence

signal excited with 800 nm, proving the dual-laser imaging approach more information-rich than the common single-wavelength TPM. We also consider the possibility of photo-thermal damages due to intrinsic fluorophore absorption. Adopting a simple model for the 3-D energy distribution around the focal plane in case of TPA and high numerical aperture[207], the temperature rise is given by:

$$T_{3D} = \frac{P_{abs}}{\omega_0 4\pi k_T}\left[1 - \sqrt{\frac{2\tau_c}{2\tau_c + 3t}}\right] \tag{6.3}$$

where $P_{abs}$ is the total absorbed power, $\omega_0$ is the beam waist, $\tau_c$ is the thermal time constant and $k_T$ is the thermal conductivity.

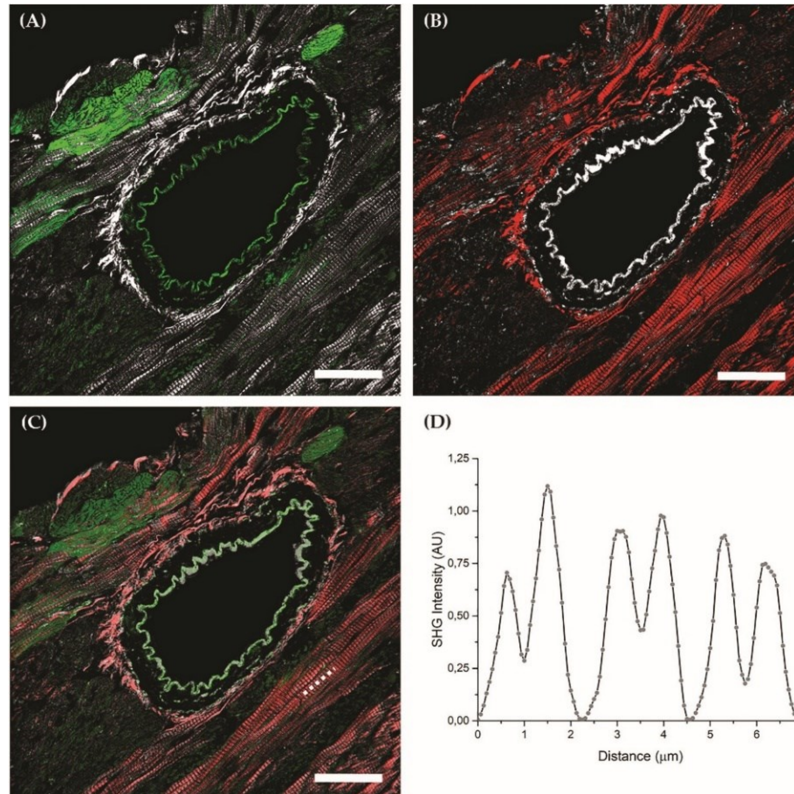


**Figure 6.3:** Simultaneous TPE and HG images of cardiac cryosections. (A) Cardiac cryosection imaged with 800 nm laser wavelength shows TPE Auto-Fluorescence (Green, $\lambda_{em}$ ~ 500 nm) and SHG signal (White, $\lambda_{em}$ = 400 nm). (B) The same field of view imaged with 1200 nm laser wavelength shows SHG (Red, $\lambda_{em}$ = 600 nm) and THG (White, $\lambda_{em}$ = 400 nm). (C) Superposition of the same field imaged with 800 nm and 1200 nm. The SHG produced by the two different laser beams, as well as the elastin Auto-Fluorescence and its THG signal, perfectly superimpose, testifying the excellent spatial alignment of the lasers. The Auto-Fluorescence excited with 800 nm also highlight some features that are not visible with the 1200 nm excitation wavelength, proving the dual-laser imaging approach more information-rich than the common single-wavelength TPM. (D) A portion of the SHG intensity profile of the dotted line in (C) shows the characteristic double-band of sarcomeres morphology. Scale bars 50 μm.

Given that $k_T \approx 0.55$ WK$^{-1}$m$^{-1}$ for most of the biological tissues[208], $\omega_0$ (800 nm) ≈ 249 nm and $\omega_0$ (1200 nm) ≈ 374 nm for 1.05 NA, and the volumetric heat capacity of biological tissues[209] is $\rho \approx 3.6$ MJm$^{-3}$K$^{-1}$, $\tau_c$ can be calculated from:

$$\tau_c = \frac{\omega_0^2 \rho}{4k_T} \tag{6.4}$$

Since both $\tau_c$ (800 nm) = 144 ns and $\tau_c$ (1200 nm) = 233 ns are much longer than the inter-pulse interval of our laser source ($I_I$ = 12 ns), the incremental temperature rise during a single pulse can be considered roughly equal to the steady-state temperature rise $T_{3D}$ (t = ∞) divided by a factor $\tau_c I_I$. Therefore, the heating inside the focal volume for high-repetition-rate lasers can be treated like CW illumination and, since for a typical fluorophore $P_{abs} \approx 10^{-5} P_{avg}$ (average incident power), appears to be negligible at our working 2PM parameters. In addition to intrinsic biological fluorophores, such as myosin, collagen, and elastin, that report solely on structural information, nicotinamide adenine dinucleotide (NADH) also emits a strong TPE signal[210] that is related to the metabolic state of the imaged cells. We thus apply our setup to study skeletal muscle cryosections, in order to discriminate glycolytic and oxidative muscle fibers depending on their NADH/mitochondria content[211]. As shown in Figure 6.4, two consecutive gastrocnemius muscle cryosections display fibers with higher TPE signal corresponding to those with higher Succinate Dehydrogenase (SDH) intensity in standard histology, consistently with the NADH origin of the TPE Auto-Fluorescence. Oxidative fibers show stronger SDH activity upon staining, corresponding to fibers having a larger number of mitochondria, more oxidative capacity, and a smaller cross-sectional area. Upon repeated investigations of several cryosections (Figure 6.4.D), we confirm the strict correlation between TPE and SDH intensity (Figure 6.4.E), thus confirming Label-Free TPE as a possible candidate for NADH quantification studies[212,213]. Furthermore, we confirm that the more oxidative fibers, having higher average TPE signal per encircled area, are those with the smaller cross-sectional area (Figure 6.4.F). From the same cryosection, we can obtain additional information on collagen content (via SHG signal) without the need for additional staining. We perform a Hematoxylin/Eosin staining in the consecutive cryosection of the same muscle (Figure 6.4.C) in order to verify that the SHG signal really gives the same information about collagen as the conventional, widely used, staining method.

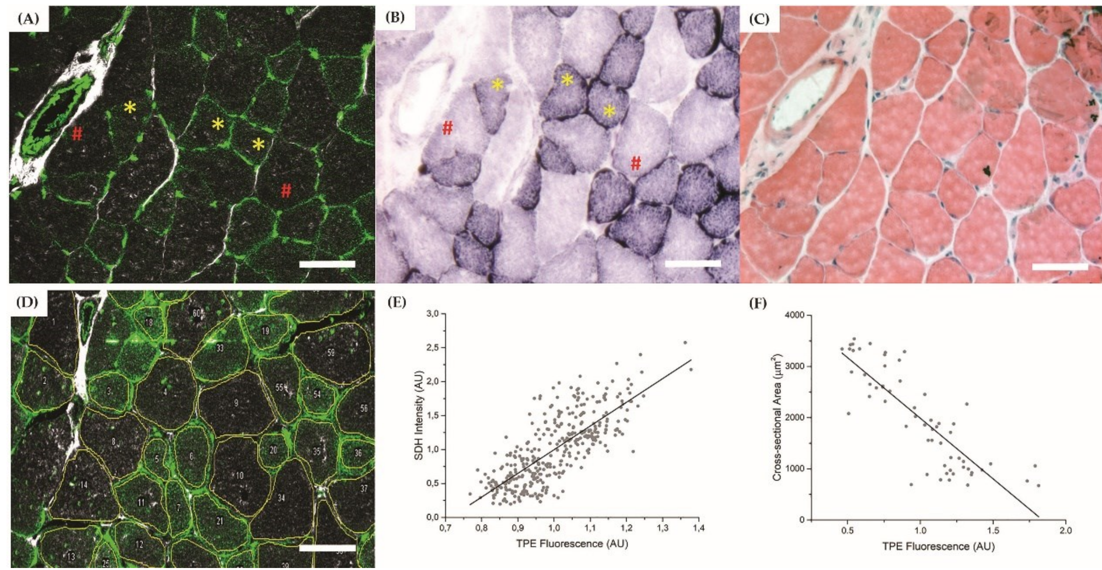


**Figure 6.4:** TPE of NADH in muscle cryosections. (A) TPE (Green, $\lambda_{em}$ ~ 500 nm) and SHG (White, $\lambda_{em}$ = 400 nm) signals from gastrocnemius muscles cryosection. (B) SDH staining of the consecutive cryosection from the same muscle. (C) Hematoxylin/Eosin staining of the consecutive cryosection from the same muscle. (D) ROI analysis of the fibers within a muscle cryosection. (E) Correlation analysis of TPE and SDH signal intensity from the same fiber (N = 4 cryosections, n =350 fibers). Pearson correlation coefficient P > 0.75. Yellow (*) and red (#) highlight corresponding fibers, oxidative and glycolytic respectively. (F) Cross-sectional area plotted against TPE fluorescence intensity highlight the higher mitochondria content of smaller fibers. Pearson correlation coefficient P > 0.85. Scale bars 100 µm.

We proceed to examine freshly excised, unstained mouse lungs, as a good example of a challenging thick sample. As can be seen in Figure 6.5, exciting with 800 nm produces an SHG signal that enables us to easily recognize the collagen fibrillary structure of the lungs, and a green Auto-Fluorescence signal from the intrinsic fluorophores that highlights the nuclei of several cells, as well as many lipid bodies scattered inside the lungs tissue. All features remain perfectly sharp and distinguishable even at relatively high zoom level, without any sign of photo-bleaching from collagen SHG, limited Auto-Fluorescence bleaching, and no photo-thermal damages, confirming the strength of a properly optimized Label-Free setup. Illuminating the specimen with 1200 nm light allows us to simultaneously image collagen fibrils (SHG) and lipid bodies, which are confirmed a strong source of Third Harmonic Generation (THG) signal as was shown before[189], without any detectable Auto-Fluorescence from other features, easing the study of these important organelles[214,215] inside their native collagen matrix in a totally Label-Free environment.

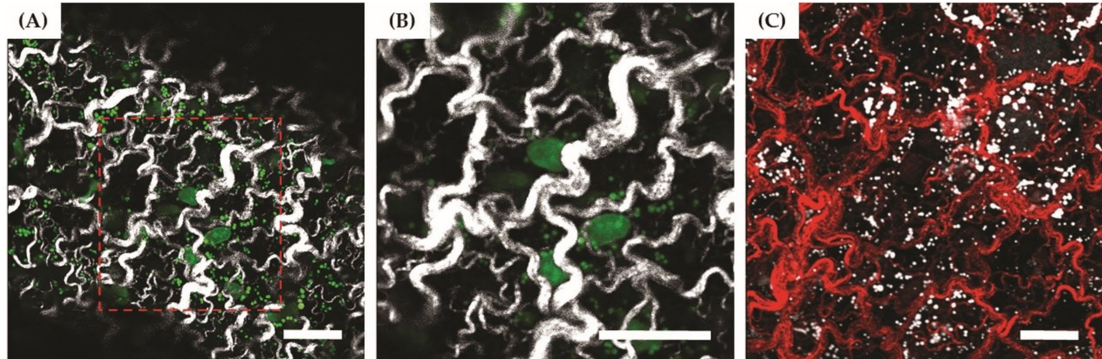


**Figure 6.5:** TPE/SHG and SHG/THG images of ex-vivo lung tissue. (A) TPE and SHG signals imaged at 800 nm. Cells nuclei and lipid bodies can be recognized by their TPE Auto-Fluorescence Emission (Green, $\lambda_{em}$ ~ 500 nm) while the coarse collagen fibers produce a strong SHG signal (White, $\lambda_{em}$ = 400 nm). (B) Magnification of the area inside the red box. (C) SHG from collagen fibers and THG from lipid bodies are simultaneously excited by a 1200 nm wavelength without any Auto-Fluorescence background. The image shows a different section of the same sample as (A). Scale bars 20 μm.

The main advantage of using a microscopy setup with two independent laser sources is that we can achieve the optimal illumination conditions for two distinct features without any compromise on signal strength or excitation efficiency. This is particularly useful for a Label-Free imaging technique, where, usually, the detected signals are significantly lower than the average fluorescence signal coming from commercial fluorophores and the requirements needed to obtain a good S/N ratio are more stringent. In order to prove what our multi-modal setup can achieve when applied to a biologically relevant specimen, we image a portion of decellularized bovine pericardium using both laser sources simultaneously (see Figure 6.6). The sample is primarily made of collagen fibrils, thus one of the laser sources is entirely dedicated to the optimization of the SHG emission from the bundles. Another significant part of the sample consists of elastin, which has its Auto-Fluorescence Excitation maximum at 425 nm[216], thus requiring a Two-Photon Excitation beam tuned around 800 nm in order to achieve the highest signal strength. However, collagen shows a significant absorption of blue photons[216] which competes with the Two-Photon Excitation of the elastin Auto-Fluorescence and the detection of the SHG signal coming from the collagen itself (due to Auto-Absorption) resulting in a lower S/N ratio at a given excitation power and a lower SHG penetration depth. We solve this problem tuning one laser source to 800 nm and the other to 1200 nm: the first beam is optimized for the imaging of elastin Auto-Fluorescence while the second beam is optimized for maximum SHG excitation efficiency. At 1200 nm, no significant elastin excitation is measured, the SHG signal is significantly

stronger (due to lack of competing processes) and the penetration depth inside the tissue is of a few hundreds of microns, thus enabling 3D reconstruction studies on optically thick samples. Z-stacks performed on thick tissue show that the SHG signal could be detected without any problem up to 200 μm deep inside the sample (Figure 6.6.C).

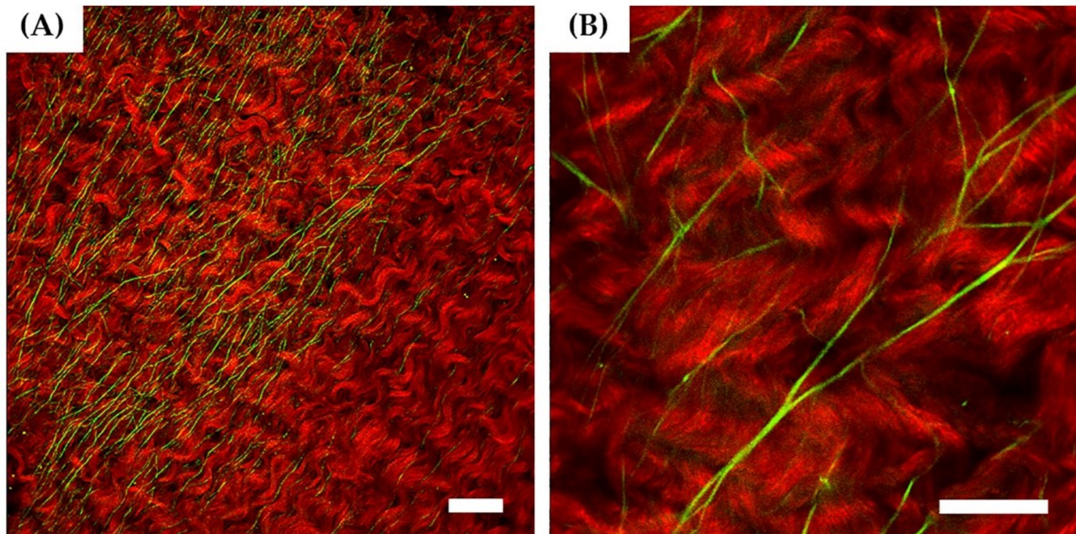


**Figure 6.6:** Simultaneous TPE and SHG images of the decellularized pericardium. (A) SHG signal from collagen bundles imaged with 1200nm wavelength (Red, $\lambda_{em}$ = 600 nm) and elastin Auto-Fluorescence excited with 800nm wavelength (Green, $\lambda_{em}$ ~ 500 nm). (B) Details of the elastin and the collagen structure. Scale bars 50 μm.

# 6.3 Materials and Methods

All experimental procedures are performed according to the European Commission guidelines and have been approved by the local ethical committee and the Italian authority (Ministero della Salute), in compliance of Italian Animal Welfare Law (Law n. 116/1992 and subsequent modifications).

- **Heart Cryosections:** Mice were sacrificed by cervical dislocation and hearts were quickly harvested and cut in two portions in the transverse direction and processed as described elsewhere[217]. Blood clots were carefully removed, and the heart was fixed to maintain structural integrity with 1% paraformaldehyde in phosphate buffered saline (PBS 1X: 137 NaCl, 2.7 KCl, 10 $Na_2HPO_4$, 1.8 $KH_2PO_4$, in mM) at room temperature for 15 minutes. After 3 washes of 5 minutes with PBS 1X, hearts could dehydrate in sucrose 30% (w/v in distilled water) at 4 °C overnight. The following day, hearts were embedded in OCT freezing medium (Optimal Cutting Temperature, Kaltec) and carefully frozen in

liquid nitrogen vapor. Frozen samples were maintained at -80 °C. Frozen hearts were cut in 10 μm slices using a cryostat (Leica CM1850, Leica Microsystems GmbH, Wetzlar, Germany) and placed on superfrost glass slides (Vetrotecnica) maintained at -80 °C until use.

- **Gastrocnemius Muscle and SDH Staining:** Gastrocnemius muscles were harvested from mice and immediately frozen in liquid nitrogen, maintained at -80 °C and used within a few days, to minimize NADH fluctuations. Ten-micron cryosections were cut with a cryostat (Leica CM1850, Leica Microsystems GmbH, Wetzlar, Germany), maintaining the same slicing angle for all the sections. Some slices were stained with Succinate dehydrogenase (SDH) activity while others were directly observed in 2PM. SDH cryosections were also examined under a fluorescence microscope (Olympus BX60), as described elsewhere[218].

- ***Ex Vivo* Lungs:** Mice were sacrificed by cervical dislocation and lungs were quickly harvested and carefully washed with ice-cold PBS to avoid blood clotting. Lungs were then transferred to a petri dish filled with PBS. To prevent curling and movement, lungs were held down by a home-made platinum holder.

- **Decellularized Bovine Pericardium:** Bovine pericardia were collected from the local slaughterhouse and decellularized using a method based on alternated hypo- and hypertonic solutions, detergents (Triton X-100 and sodium cholate, Sigma-Aldrich, Saint Louis, MO, USA) and non-specific endonucleases (Benzonase, Sigma-Aldrich)[219,220]. Following the decellularization procedure, samples of 1 $cm^2$ were placed into plastic embedding devices (Bio Optica, Milano, Italy) and covered by a thin layer of 4% low melting agarose solution prepared in PBS (Sigma-Aldrich).

- **Statistical Analysis:** Images were processed in Fiji using the ROI Manager plug-in in order to obtain mean ROI intensities and area values for every single hand-drawn region of interest, delimiting the exposed fibers cross-sections. Pearson correlation coefficient was evaluated in OriginPro™ 2016 and data were fitted by linear regression.

# Chapter 7

# Conclusions

We successfully designed and developed a working prototype of our hybrid resonance enhanced silicon photodiode. The measured increase in responsivity at 950 nm is ~50%, with respect to a traditional silicon photodiode, used as substrate. The enhancement does not reach the maximum predicted theoretical value of ten times the original responsivity, but it is still a significant increase, which put our device above any non-enhanced silicon-based detector (considering an equal active area thickness). There are multiple possible reasons that could account for the difference between the real and theoretical enhancement. It is known that working with Wood's anomalies of the second type is quite a difficult task since their excitation usually requires a high degree of control over all the structural and experimental parameters. In our case, the two most probable causes for the lack of an efficient anomaly excitation are the relatively high "lateral roughness" of the silver nanodots and the complete lack of control over the light incident angle during the electro-optical characterization process.

It has been shown before that a roughness above ~7 nm can completely damp the resonance peak of a Wood's anomaly[221]. Our silver nanodots have really good roughness levels on the top surface, as discussed in the previous chapter, with a root mean square value between 2-5 nm, depending on the metal deposition recipe. However, due to the polycrystalline nature of the deposited Ag, their "lateral roughness" (the roughness of the lateral surfaces) appears to be quite substantial. From an SEM analysis, its root mean square seems to be ~10-15 nm, which is high enough to be a reasonable candidate for the anomaly peak dampening. A possible solution to this problem could be trying to reduce the later roughness *via* thermal treatment of the nanodots array. Preliminary experiments show us that thermal annealing at 220 °C for 60 min (in $N_2$ atmosphere) can help to reduce the lateral surfaces' roughness of the dots (see Figure 7.1), but further studies are needed.

A related problem arises from the difference measured between the array period along the tow in-plane axis, the x-axis and the y-axis. Having a structure with two (slightly) different periodicities equals to having two different Rayleigh singularities, thus two different coupling conditions to be satisfied in order to successfully excite a Type 2 Wood's anomaly along the two perpendicular axes. This means that our prototype performance could be severely dampened by destructive interference between the two anomalies.

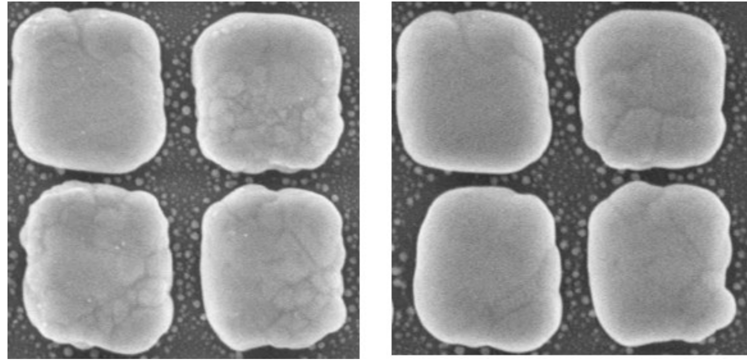

**Figure 7.1:** Comparison between a few silver nanodots before (left) and after (right) thermal annealing at 220 °C for 60 min in nitrogen atmosphere. There seems to be an improvement of the lateral roughness and a decrease in the average number of grains inside a single dot.

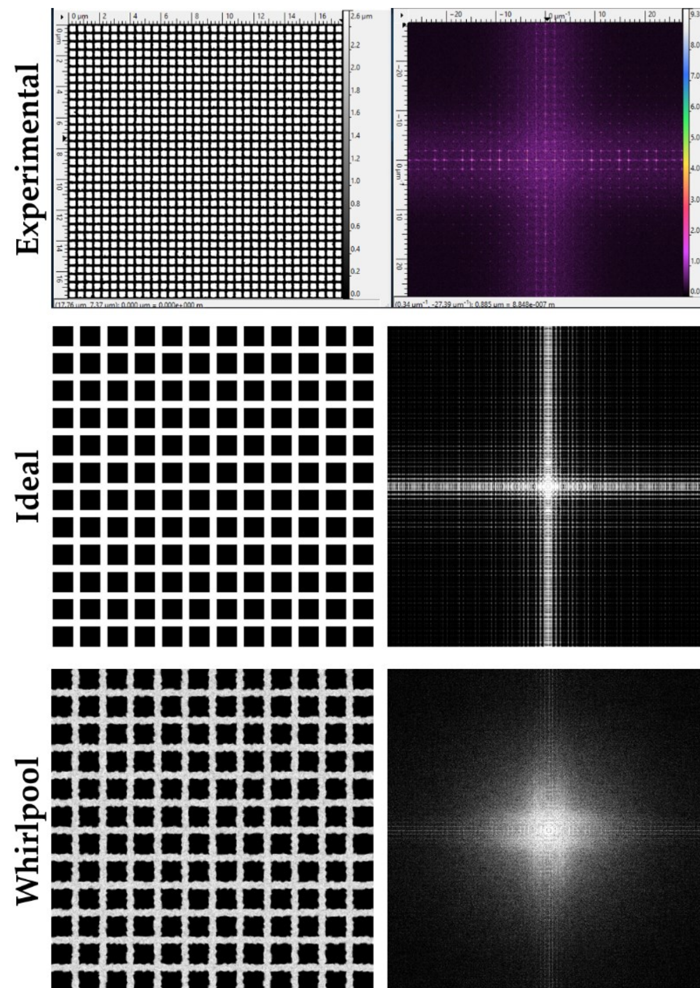


**Figure 7.2:** Fourier transform analysis of an array SEM image (top) compared to the Fourier transform of an ideal array (center) and the Fourier transform of an array of dots with a high degree of lateral roughness (bottom). The similarities between the experimental image transform and the last transform analysis are clearly visible. This "disorder" can be the main cause for the vanishing of the anomaly peak.

Christ et al. also showed that the angle of incidence of the light impinging on the device is crucial for correctly exciting and measuring an anomaly resonance[222,223]. Light striking a structure designed for normal incidence with an angle greater than ~12° completely fails to excite the anomaly. Furthermore, a high degree of angle resolution (within 1°) is necessary in order to properly measure the resonance peak. Our electro-optical characterization setup lacks control over both these conditions because the light exiting from the monochromator is highly divergent and, at present, cannot be collimated and the angle of incidence cannot be chosen. A better setup is needed in order to produce more controlled and precise results.

We have also presented our multi-modal microscope with two laser sources, capable of performing TPM and HG simultaneously by fine-tuning a specific source for one or the other. Our approach combines the best traits of both imaging techniques (e.g. intrinsic optical sectioning, reduced photo-bleaching, Label-Free capabilities) while avoiding any compromise on image quality, signal strength, time investment and with a significantly reduced need for post-processing corrections with respect to common sequential multi-wavelength approaches[189]. This is particularly relevant for HG, where the signal intensity is extremely sensitive to many external factors and the need for careful optimization of the experimental parameters on a sample basis is stringent. We showed that after a calibration of the lasers polarization states, the microscope can acquire images with a very high signal intensity and good S/N ratio for both TPE and HG and enables the simultaneous Label-Free imaging of different structures on which several studies can be successfully performed in order to obtain biologically relevant information without significantly altering the samples. We also proved that all the capabilities of our setup remain unchanged while studying thick ex vivo samples, detecting significantly strong signals up to 200 μm deep in the sample. We fully took advantage of the dual laser configuration while examining decellularized bovine pericardium, achieving an optical penetration depth of hundreds of microns and performing 3D reconstructions from z-stacks of optically thick samples without the need of any molecular probe labeling. Using Label-Free techniques preserves the samples as similar as possible to their original conditions, even after several hours and many imaging sessions, maximizing the repeatability and the feasibility of multi-techniques examinations. As a final remark, we want to emphasize the high upgradability of our dual-laser setup, in which more complex Label-Free Microscopy methods, like Coherent Anti-Stokes Raman Spectroscopy (CARS) and Stimulated Raman Spectroscopy (SRS) Microscopy, could easily be integrated. The possibility of expanding our setup also in the direction of Two-Photon Excitation STimulated Emission Depletion (2P-STED) Nanoscopy is currently being examined, as well as the use of adaptive optics to control more precisely the beams overlapping and the aberration-correction procedure[224].

# Appendix A

# Simulations on SOI substrate

It is possible to design an all-optical structure capable of theoretically enhance the absorption efficiency of our silicon photodetector similarly, if not better than the plasmonic nanodots array, using a dielectric diffraction grating made of silicon nitride. Dielectric diffraction gratings have several advantages over plasmonic gratings, mostly related to their fabrication process and structural parameters control, therefore making them an interesting alternative for the enhancement of traditional photodetectors. However, such a structure requires a silicon-on-insulator (SOI) substrate, instead of the simpler $Si/Si_3N_4$ photodiode (see Figure A.1), as was previously shown by Ghioni et al. for cavity-resonance enhanced SPADs[225,226]. Assuming an active area 1μm thick and a working wavelength of 950 nm, all the simulation methods previously described in Chapter 3 can be applied also to this device.

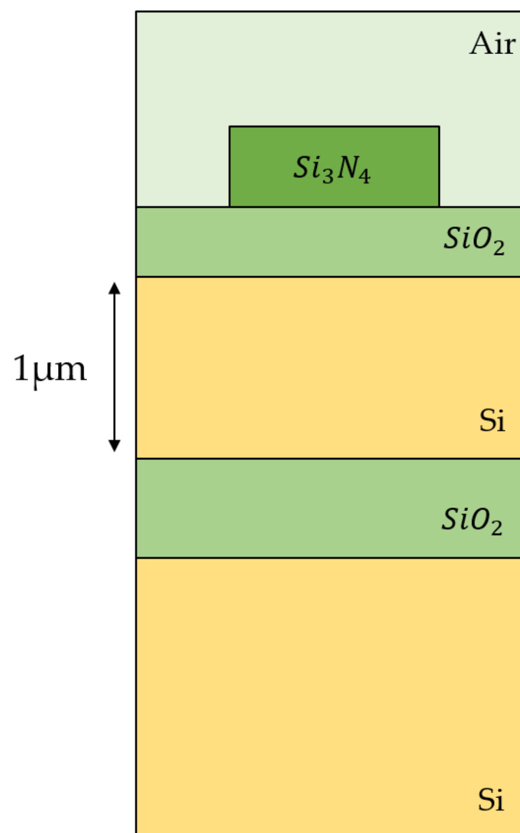


**Figure A.1:** Schematic representation of an all-optical absorption enhancement structure with a silicon nitride diffraction grating and a SOI substrate photodetector.

Using a TM incident light, after structural optimization we find two distinct resonances at p ~ 560 nm and p ~ 650 nm. From a quick examination of the simulated electromagnetic fields, both resonance peaks appear to be related to two guided modes inside the relatively thin slab of active silicon (see Figure A.2), however, while the p ~ 560nm peak is extremely tall and narrow (up to $P_{abs}$ ~ 80% for a full-width half maximum of ~ 5 nm), the other peak is much broader and shorter. This difference probably arises from a significant variation of coupling efficiency between the impinging light and the two resonances.

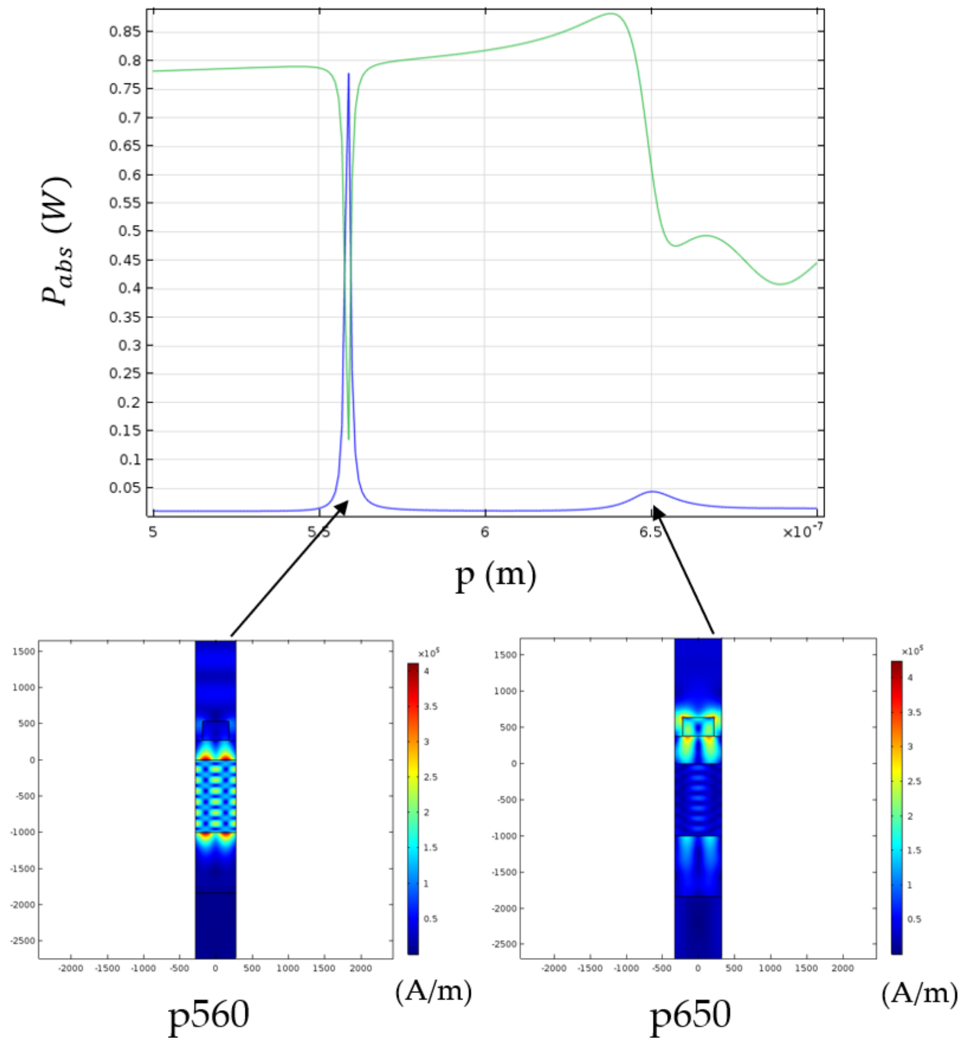


**Figure A.2:** Simulated power absorbed inside the active silicon slab (blue curve) and reflectance spectrum (green curve) of a theoretical all-optical enhanced device illuminated with TM light. As can be clearly seen from the magnetic field norm plots, both resonance peaks are related to one (or more) guided mode inside the active slab, but the coupling efficiency is much higher in the case of the p560 resonance.

Switching to a TE incident light, we can find yet again another guided mode resonance peak at p ~ 675 nm (unlike the plasmonic array case, where only TM modes can be supported in a 2-D environment) very much like the hybrid resonance peak described for the nanodots array, in terms of strength and FWHM ($P_{abs}$ ~ 20% and FWHM ~ 20 nm). Its reasonable width makes this peak the best candidate for future applications in realistic cases.

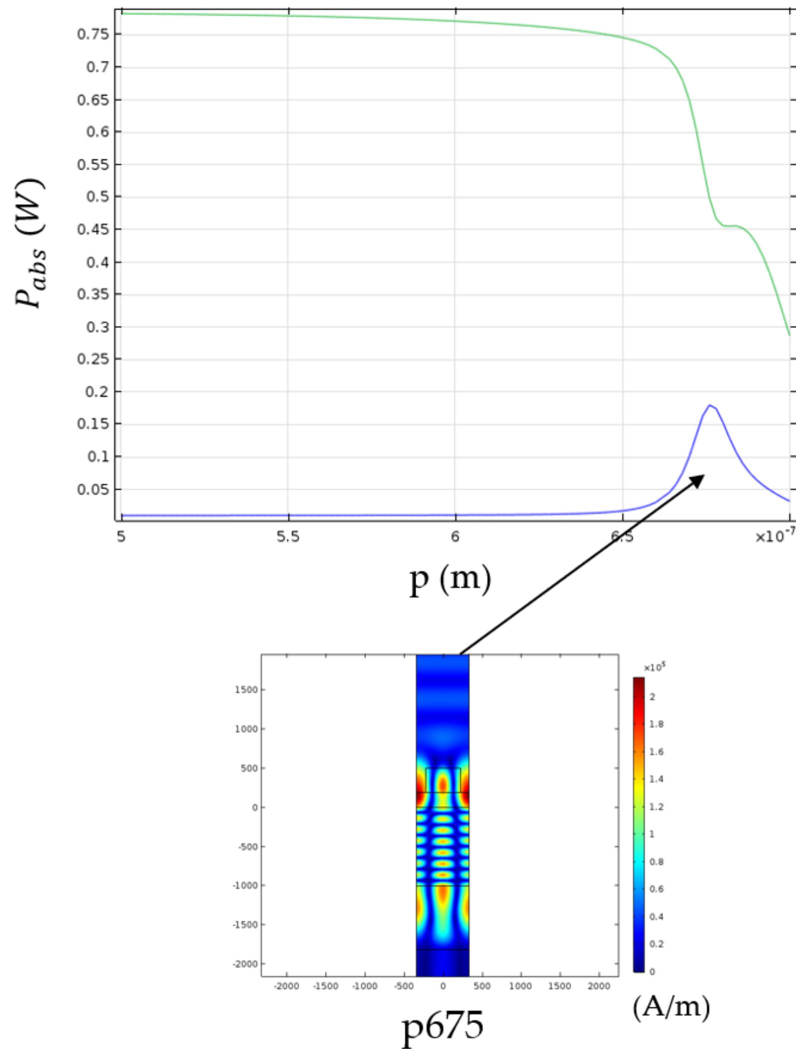


**Figure A.3:** Simulated power absorbed inside the active silicon slab (blue curve) and reflectance spectrum (green curve) of a theoretical all-optical enhanced device illuminated with TE light. As can be clearly seen from the magnetic field norm plot, the resonance peak is related to one (or more) guided mode inside the active slab, traveling along the silicon nitride slits.

Finally, exploring the pitch/wavelength maps of both TM and TE illumination modes shows that the TE p675 resonance can be excited and stays wider than the stronger TM p560 resonance up until ~ 970 nm (incident wavelength), then it completely disappears, while the TM p560 persists. This behavior leaves us with a choice to make: exploit the broader, more reasonable but less strong, TE resonance and accept its limited operative wavelength range, or choose the incredibly strong but much narrower TM resonance for its wider operative range potential? There probably is no absolute right choice, but it depends on the specific applications and the achievable degree of control over all the fabrication process parameters.

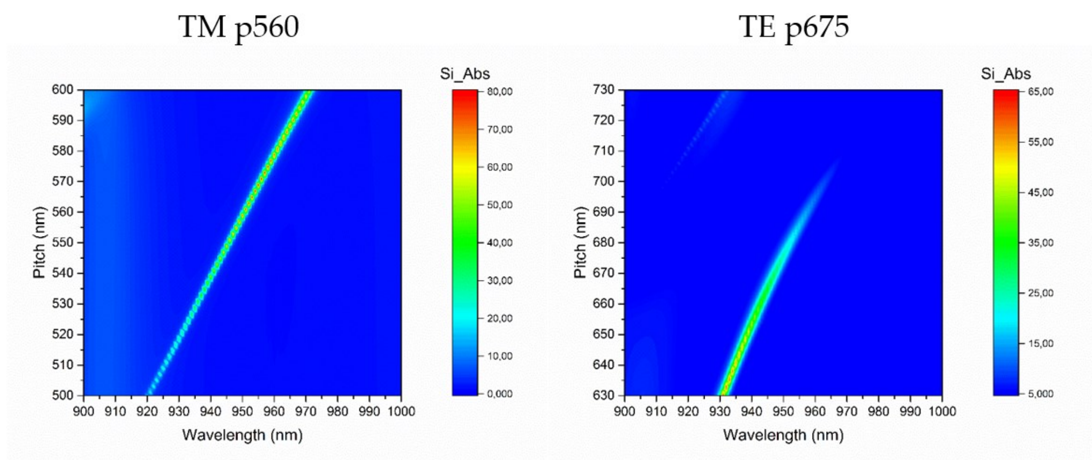


**Figure A.4:** Pitch/wavelength maps of the TM p560 resonance (left) and the TE p675 resonance (right). The TE resonance is much wider than the TM resonance, however it cannot be excited above ~ 970 nm.

# Bibliography


1. Rieke, G. H. & Rubin, L. G. Detection of Light: From the Ultraviolet to the Submillimeter. *Phys. Today* **48**, 70–71 (1995).

2. Geis, M. W. *et al.* CMOS-compatible all-Si high-speed waveguide photodiodes with high responsivity in near-infrared communication band. *IEEE Photonics Technol. Lett.* **19**, 152–154 (2007).

3. Elgala, H., Mesleh, R. & Haas, H. Indoor optical wireless communication: Potential and state-of-the-art. *IEEE Commun. Mag.* **49**, 56–62 (2011).

4. Waxman, A. M. *et al.* Color night vision: Opponent processing in the fusion of visible and IR imagery. *Neural Networks* **10**, 1–6 (1997).

5. Stuart, B. H. *Infrared Spectroscopy: Fundamentals and Applications*. *Infrared Spectroscopy: Fundamentals and Applications* (2005). doi:10.1002/0470011149

6. Meledin, D. V. *et al.* A 1-THz superconducting hot-electron-bolometer receiver for astronomical observations. *IEEE Trans. Microw. Theory Tech.* **52**, 2338–2343 (2004).

7. Weissleder, R., Tung, C. H., Mahmood, U. & Bogdanov, A. In vivo imaging of tumors with protease-activated near-infrared fluorescent probes. *Nat. Biotechnol.* **17**, 375–378 (1999).

8. Huang, X., El-Sayed, I. H., Qian, W. & El-Sayed, M. A. Cancer cell imaging and photothermal therapy in the near-infrared region by using gold nanorods. *J. Am. Chem. Soc.* **128**, 2115–2120 (2006).

9. Konstantatos, G. & Sargent, E. H. Nanostructured materials for photon detection. *Nature Nanotechnology* **5**, 391–400 (2010).

10. Soci, C. *et al.* Nanowire Photodetectors. *J. Nanosci. Nanotechnol.* **10**, 1430–1449 (2010).

11. Zia, R., Schuller, J. A., Chandran, A. & Brongersma, M. L. Plasmonics: the next chip-scale technology. *Mater. Today* **9**, 20–27 (2006).

12. Schuller, J. A. *et al.* Plasmonics for extreme light concentration and manipulation. *Nature Materials* **9**, 193–204 (2010).

13. Atwater, H. A. & Polman, A. Plasmonics for improved photovoltaic devices. *Nat. Mater.* **9**, 205–13 (2010).

14. Kawano, Y., Fuse, T., Toyokawa, S., Uchida, T. & Ishibashi, K. Terahertz photon-assisted tunneling in carbon nanotube quantum dots. *J. Appl. Phys.* **103**, (2008).

15. Komiyama, S. Single-photon detectors in the Terahertz range. *IEEE J. Sel. Top. Quantum Electron.* **17**, 54–66 (2011).

16. Zheng Wei Pan, Zu Rong Dai & Zhong Lin Wang. Nanobelts of semiconducting oxides. *Science (80-. ).* **291**, 1947–1949 (2001).

17. Iijima, S. Helical microtubules of graphitic carbon. *Nature* **354**, 56–58 (1991).

18. Koppens, F. H. L. *et al.* Photodetectors based on graphene, other two-dimensional materials and hybrid systems. *Nature Nanotechnology* **9**, 780–793 (2014).

19. Irvin, P. *et al.* Rewritable nanoscale oxide photodetector. *Nat. Photonics* **4**, 849–852 (2010).

20. Roy, K. *et al.* Graphene-MoS 2 hybrid structures for multifunctional photoresponsive memory devices. *Nat. Nanotechnol.* **8**, 826–830 (2013).

21. Yang, F. *et al.* Saliva microbiomes distinguish caries-active from healthy human populations. *ISME J.* **6**, 1–10 (2012).

22. Hodgkinson, J. & Tatam, R. P. Optical gas sensing: A review. *Measurement Science and Technology* **24**, (2013).

23. Yang, Z. *et al.* CdS/ZnO Core/Shell nanowire-built films for enhanced photodetecting and optoelectronic gas-sensing applications. *Adv. Opt. Mater.* **2**, 738–745 (2014).

24. Gogurla, N., Sinha, A. K., Santra, S., Manna, S. & Ray, S. K. Multifunctional Au-ZnO plasmonic nanostructures for enhanced UV photodetector and room temperature NO sensing devices. *Sci. Rep.* **4**, (2014).

25. Bie, Y. Q. *et al.* Self-powered, ultrafast, visible-blind UV detection and optical logical operation based on ZnO/GaN nanoscale p-n junctions. *Adv. Mater.* **23**, 649–653 (2011).

26. Barnes, W. L., Dereux, A. & Ebbesen, T. W. Surface plasmon subwavelength optics. *Nature* **424**, 824–30 (2003).

27. Homola, J. Surface plasmon resonance sensors for detection of chemical and biological species. *Chemical Reviews* **108**, 462–493 (2008).

28. Ebbesen, T. W., Genet, C. & Bozhevolnyi, S. I. Surface-plasmon circuitry. *Phys. Today* **61**, 44–50 (2008).

29. Berini, P. Surface plasmon-polariton amplifiers and lasers. *Nat. Photonics* 1–9 (2011). doi:10.1038/nPhoton.2011.285

30. Daboo, C. *et al.* Surface-plasmon-enhanced photodetection in planar AuGaAs schottky junctions. *Thin Solid Films* **189**, 27–38 (1990).

31. Derov, J., Teng, Y. Y. & Karakashian, A. S. Angular scan spectrum of a surface plasma excitation on a Schottky diode. *Phys. Lett. A* **95**, 197–200 (1983).

32. Torosian, K. M., Karakashian, A. S. & Teng, Y. Y. Surface plasma-enhanced internal photoemission in gallium arsenide Schottky diodes. *Appl. Opt.* **26**, 2650 (1987).

33. Derov, J., Teng, Y. Y. & Karakashian, A. S. Angular scan spectra in the visible of surface plasma excitation on a Schottky photodiode. *Appl. Opt.* **26**, 4038 (1987).

34. Cazeca, M. J., Chang, C. C. & Karakashian, A. S. A model calculation for surface plasma-enhanced internal photoemission in Schottky-barrier photodiodes. *J. Appl. Phys.* **66**, 3386–3391 (1989).

35. Daboo, C., Baird, M. J., Hughes, H. P., Apsley, N. & Emeny, M. T. Improved surface plasmon enhanced photodetection at an AuGaAs schottky junction using a novel molecular beam epitaxy grown Otto coupling structure. *Thin Solid Films* **201**, 9–27 (1991).

36. Tamm, I. R. *et al.* Analysis of surface plasmon polariton enhancement in photodetection by Al-GaAs Schottky diodes. *Solid State Electron.* **36**, 1417–1427 (1993).

37. Tamm, I. R., Dawson, P., Pate, M. A., Grey, R. & Hill, G. Photosignal enhancement in Al-GaAs diodes due to surface plasmons and guided wave modes. *J. Appl. Phys.* **74**, 7481–7487 (1993).

38. Dawson, P., Cairns, G. F. & O'Prey, S. M. Prism coupler with variable coupling gap. *Rev. Sci. Instrum.* **71**, 4208–4212 (2000).

39. Sellai, A. & Dawson, P. Quantum efficiency in GaAs Schottky photodetectors with enhancement due to surface plasmon excitations. *Solid. State. Electron.* **46**, 29–33 (2002).

40. Soole, J. B. D., Lamb, R. N., Hughes, H. P. & Apsley, N. Surface plasmon enhanced photoconductivity in planar metal-oxide-metal tunnel junctions. *Solid State Commun.* **59**, 607–611 (1986).

41. Hayashi, S., Kozaru, K. & Yamamoto, K. Enhancement of photoelectric conversion efficiency by surface plasmon excitation: A test with an organic solar cell. *Solid State Commun.* **79**, 763–767 (1991).

42. Kume, T., Hayashi, S. & Yamamoto, K. Enhancement of photoelectric conversion efficiency in copper phthalocyanine solar cell by surface plasmon excitation. *Jpn. J. Appl. Phys.* **32**, 3486 (1993).

43. Kume, T., Hayashi, S., Ohkuma, H. & Yamamoto, K. Enhancement of photoelectric conversion efficiency in copper phthalocyanine solar cell: White light excitation of surface plasmon polaritons. *Jpn. J. Appl. Phys.* **34**, 6448–6451 (1995).

44. Brueck, S. R. J., Diadiuk, V., Jones, T. & Lenth, W. Enhanced quantum efficiency internal photoemission detectors by grating coupling to surface plasma waves. *Appl. Phys. Lett.* **46**, 915–917 (1985).

45. Collin, S., Pardo, F. & Pelouard, J.-L. Resonant-cavity-enhanced subwavelength metal–semiconductor–metal photodetector. *Appl. Phys. Lett.* **83**, 1521–1523 (2003).

46. Sellai, A. Resonant-cavity Schottky photodetectors with a grating profiled surface. in *Nuclear Instruments and Methods in Physics Research, Section A: Accelerators, Spectrometers, Detectors and Associated Equipment* **504**, 170–176 (2003).

47. Collin, S., Pardo, F., Teissier, R. & Pelouard, J.-L. Efficient light absorption in metal–semiconductor–metal nanostructures. *Appl. Phys. Lett.* **85**, 194–196 (2004).

48. Crouse, D. Numerical modeling and electromagnetic resonant modes in complex grating structures and optoelectronic device applications. *IEEE Trans. Electron Devices* **52**, 2365–2373 (2005).

49. Panoiu, N. C. & Osgood, Jr., R. M. Enhanced optical absorption for photovoltaics via excitation of waveguide and plasmon-polariton modes. *Opt. Lett.* **32**, 2825 (2007).

50. Okamoto, D., Fujikata, J., Nishi, K. & Ohashi, K. Numerical study of near-infrared photodetectors with surface-plasmon antenna for optical communication. *Jpn. J. Appl. Phys.* **47**, 2921–2923 (2008).

51. Yoon, J. W., Park, W. J., Lee, K. J., Song, S. H. & Magnusson, R. Surface-plasmon mediated total absorption of light into silicon. *Opt. Express* **19**, 20673 (2011).

52. Guo, X., Zhang, R., Cao, J. & Liu, H. Surface plasmon-enhanced absorption in metal grating coupled terahertz quantum well photodetectors. *IEEE J. Quantum Electron.* **48**, 1113–1119 (2012).

53. Genevet, P., Lin, J., Kats, M. A. & Capasso, F. Holographic detection of the orbital angular momentum of light with plasmonic photodiodes.

*Nat. Commun.* **3**, (2012).

54. Glass, A. M., Liao, P. F., Olson, D. H. & Humphrey, L. M. Optical metal–oxide tunnel detectors with microstructured electrodes. *Opt. Lett.* **7**, 575 (1982).

55. Kroo, N., Szentirmay, Z. & Felszerfalvi, J. Internal photoeffect in periodically corrugated MOM structures. *Phys. Lett. A* **101**, 235–238 (1984).

56. Berthold, K., Höpfel, R. A. & Gornik, E. Surface plasmon polariton enhanced photoconductivity of tunnel junctions in the visible. *Appl. Phys. Lett.* **46**, 626–628 (1985).

57. Pala, R. A., White, J., Barnard, E., Liu, J. & Brongersma, M. L. Design of Plasmonic Thin-Film Solar Cells with Broadband Absorption Enhancements. *Adv. Mater.* **21**, 3504–3509 (2009).

58. Sefunc, M. A., Okyay, A. K. & Demir, H. V. Volumetric plasmonic resonator architecture for thin-film solar cells. *Appl. Phys. Lett.* **98**, (2011).

59. Tang, L. *et al.* C-shaped nanoaperture-enhanced germanium photodetector. *Opt. Lett.* **31**, 1519 (2006).

60. Yu, Z., Veronis, G., Fan, S. & Brongersma, M. L. Design of midinfrared photodetectors enhanced by surface plasmons on grating structures. *Appl. Phys. Lett.* **89**, (2006).

61. Bhat, R. D., Panoiu, N. C., Brueck, S. R. & Osgood, R. M. Enhancing the signal-to-noise ratio of an infrared photodetector with a circular metal grating. *Opt. Express* **16**, 4588 (2008).

62. Shackleford, J. A., Grote, R., Currie, M., Spanier, J. E. & Nabet, B. Integrated plasmonic lens photodetector. *Appl. Phys. Lett.* **94**, (2009).

63. Tang, L., Latif, S. & Miller, D. A. B. Plasmonic device in silicon CMOS. *Electron. Lett.* **45**, 706 (2009).

64. Dunbar, L. A. *et al.* Enhanced transmission from a single subwavelength slit aperture surrounded by grooves on a standard detector. *Appl. Phys. Lett.* **95**, (2009).

65. Zheng, G. & Yang, C. Improving weak-signal identification via predetection background suppression by a pixel-level, surface-wave enabled dark-field aperture. *Opt. Lett.* **35**, 2636 (2010).

66. Das, N. *et al.* Analysis of nano-grating-assisted light absorption enhancement in metal-semiconductor-metal photodetectors patterned

using focused ion-beam lithography. *Opt. Commun.* **284**, 1694–1700 (2011).

67. Ren, F. F. *et al.* Split bull's eye shaped aluminum antenna for plasmon-enhanced nanometer scale germanium photodetector. *Nano Lett.* **11**, 1289–1293 (2011).

68. Karar, A. *et al.* High-responsivity plasmonics-based GaAs metal-semiconductor-metal photodetectors. *Appl. Phys. Lett.* **99**, (2011).

69. Min, C., Yang, L. & Veronis, G. Microcavity enhanced optical absorption in subwavelength slits. *Opt. Express* **19**, 26850 (2011).

70. Fathauer, R. W., Iannelli, J. M., Nieh, C. W. & Hashimoto, S. Infrared response from metallic particles embedded in a single-crystal Si matrix: The layered internal photoemission sensor. *Appl. Phys. Lett.* **57**, 1419–1421 (1990).

71. Fathauer, R. W., Ksendzov, A., Iannelli, J. M. & George, T. Controllable surface-plasmon resonance in engineered nanometer epitaxial silicide particles embedded in silicon. *Phys. Rev. B* **44**, 1345–1348 (1991).

72. Stuart, H. R. & Hall, D. G. Island size effects in nanoparticle-enhanced photodetectors. *Appl. Phys. Lett.* **73**, 3815–3817 (1998).

73. Schaadt, D. M., Feng, B. & Yu, E. T. Enhanced semiconductor optical absorption via surface plasmon excitation in metal nanoparticles. *Appl. Phys. Lett.* **86**, 1–3 (2005).

74. Hägglund, C., Zäch, M. & Kasemo, B. Enhanced charge carrier generation in dye sensitized solar cells by nanoparticle plasmons. *Appl. Phys. Lett.* **92**, (2008).

75. Ferry, V. E., Munday, J. N. & Atwater, H. A. Design considerations for plasmonic photovoltaics. *Adv. Mater.* **22**, 4794–4808 (2010).

76. Hyun, J. K. & Lauhon, L. J. Spatially resolved plasmonically enhanced photocurrent from Au nanoparticles on a Si nanowire. *Nano Lett.* **11**, 2731–2734 (2011).

77. Lee, Y. K. *et al.* Surface plasmon-driven hot electron flow probed with metal-semiconductor nanodiodes. *Nano Lett.* **11**, 4251–4255 (2011).

78. Green, M. A. & Pillai, S. Harnessing plasmonics for solar cells. *Nat. Photonics* **6**, 130–132 (2012).

79. Senanayake, P. *et al.* 3D Nanopillar optical antenna photodetectors. *Opt. Express* **20**, 25489 (2012).

80. Sakat, E. *et al.* Guided mode resonance in subwavelength

metallodielectric free-standing grating for bandpass filtering. *Opt. Lett.* **36**, 3054 (2011).

81. Sakat, E. *et al.* Free-standing guided-mode resonance band-pass filters: from 1D to 2D structures. *Opt. Express* **20**, 13082 (2012).

82. Collin, S. Nanostructure arrays in free-space: Optical properties and applications. *Reports on Progress in Physics* **77**, (2014).

83. Lodari, M. *et al.* Plasmon-enhanced Ge-based metal-semiconductor-metal photodetector at near-IR wavelengths. *Opt. Express* **27**, 20516 (2019).

84. Bozhevolnyi, S. I., Nikolajsen, T. & Leosson, K. Integrated power monitor for long-range surface plasmon polaritons. *Opt. Commun.* **255**, 51–56 (2005).

85. Ditlbacher, H. *et al.* Organic diodes as monolithically integrated surface plasmon polariton detectors. *Appl. Phys. Lett.* **89**, (2006).

86. Fujikata, J. *et al.* Waveguide-integrated Si nano-photodiode with surface-plasmon antenna and its application to on-chip optical clock signal distribution. in *2008 5th International Conference on Group IV Photonics, GFP* 176–178 (2008).

87. Zhu, S., Lo, G. Q., Yu, M. B. & Kwong, D. L. Low-cost and high-gain silicide Schottky-barrier collector phototransistor integrated on Si waveguide for infrared detection. *Appl. Phys. Lett.* **93**, (2008).

88. Neutens, P., Van Dorpe, P., De Vlaminck, I., Lagae, L. & Borghs, G. Electrical detection of confined gap plasmons in metal-insulator-metal waveguides. *Nat. Photonics* **3**, 283–286 (2009).

89. Falk, A. L. *et al.* Near-field electrical detection of optical plasmons and single-plasmon sources. *Nat. Phys.* **5**, 475–479 (2009).

90. Scales, C., Breukelaar, I. & Berini, P. Surface-plasmon Schottky contact detector based on a symmetric metal stripe in silicon. *Opt. Lett.* **35**, 529 (2010).

91. Goykhman, I., Desiatov, B., Khurgin, J., Shappir, J. & Levy, U. Locally-oxidized silicon surface-plasmon Schottky detector for telecom wavelengths. in *IEEE International Conference on Group IV Photonics GFP* 231–233 (2011).

92. Berini, P., Olivieri, A. & Chen, C. Thin Au surface plasmon waveguide Schottky detectors on p-Si. *Nanotechnology* **23**, (2012).

93. Ly-Gagnon, D. S. *et al.* Routing and photodetection in subwavelength

plasmonic slot waveguides. *Nanophotonics* **1**, 9–16 (2012).

94. Zang, K. *et al.* Silicon single-photon avalanche diodes with nano-structured light trapping. *Nat. Commun.* **8**, (2017).

95. Shockley, W. The Theory of p-n Junctions in Semiconductors and p-n Junction Transistors. *Bell Syst. Tech. J.* **28**, 435–489 (1949).

96. Sah, C. T., Noyce, R. N. & Shockley, W. Carrier Generation and Recombination in P-N Junctions and P-N Junction Characteristics. *Proc. IRE* **45**, 1228–1243 (1957).

97. Moll, J. L. The Evolution of the Theory for the Voltage-Current Characteristic of P-N Junctions. *Proceedings of the IRE* **46**, 1076–1082 (1958).

98. Sze, S. M. & Kwok, K. Ng. *Physics of Semiconductor Devices: Third Edition* (John Wiley & Sons, Inc., 2006).

99. Neupane, B., Chen, F., Sun, W., Chiu, D. T. & Wang, G. Tuning donut profile for spatial resolution in stimulated emission depletion microscopy. *Rev. Sci. Instrum.* **84**, 043701 (2013).

100. Stillman, G. E. & Wolfe, C. M. Avalanche Photodiodes. in *Semiconductors and Semimetals* 291–393 (1977).

101. Smith, R. G. & Personick, S. D. Receiver design for optical fiber communication systems. in 89–160 (2012).

102. Gärtner, W. W. Depletion-layer photoeffects in semiconductors. *Phys. Rev.* **116**, 84–87 (1959).

103. Maier, S. A. *Plasmonics: Fundamentals and applications* (2007).

104. Economou, E. N. Surface plasmons in thin films. *Phys. Rev.* **182**, 539–554 (1969).

105. Sarid, D. Long-Range Surface-Plasma Waves on Very Thin Metal Films. *Phys. Rev. Lett.* **47**, 1927–1930 (1981).

106. Burke, J. J., Stegeman, G. I. & Tamir, T. Surface-polariton-like waves guided by thin, lossy metal films. *Phys. Rev. B* **33**, 5186–5201 (1986).

107. Yang, F., Sambles, J. R. & Bradberry, G. W. Long-range surface modes supported by thin films. *Phys. Rev. B* **44**, 5855–5872 (1991).

108. Kretzschmann, E. & Raether, H. Radiative decay of non-radiative surface plasmons by light. *Z. Naturforsch* **23**, 2135 (1968).

109. Otto, A. Excitation of nonradiative surface plasma waves in silver by the method of frustrated total reflection. *Zeitschrift für Phys.* **216**, 398–

410 (1968).

110. Quail, J. C., Rako, J. G. & Simon, H. J. Long-range surface-plasmon modes in silver and aluminum films. *Opt. Lett.* **8**, 377 (1983).

111. Fano, U. The Theory of Anomalous Diffraction Gratings and of Quasi-Stationary Waves on Metallic Surfaces (Sommerfeld's Waves). *J. Opt. Soc. Am.* **31**, 213 (1941).

112. Wood, R. W. On a remarkable case of uneven distribution of light in a diffraction grating spectrum. *Proc. Phys. Soc. London* **18**, 269–275 (1901).

113. Cowan, J. J. & Arakawa, E. T. Dispersion of surface plasmons in dielectric-metal coatings on concave diffraction gratings. *Zeitschrift für Phys.* **235**, 97–109 (1970).

114. Ibach, H. & Lüth, H. *Solid-state physics: An introduction to principles of materials science* (2010).

115. Warren, B. E. *X-ray diffraction* (Dover Publications, 1990).

116. Park, S., Lee, G., Song, S. H., Oh, C. H. & Kim, P. S. Resonant coupling of surface plasmons to radiation modes by use of dielectric gratings. *Opt. Lett.* **28**, 1870 (2003).

117. Offerhaus, H. L. *et al.* Creating focused plasmons by noncollinear phasematching on functional gratings. *Nano Lett.* **5**, 2144–2148 (2005).

118. Devaux, E., Ebbesen, T. W., Weeber, J.-C. & Dereux, A. Launching and decoupling surface plasmons via micro-gratings. *Appl. Phys. Lett.* **83**, 4936–4938 (2003).

119. Hooper, I. R. & Sambles, J. R. Dispersion of surface plasmon polaritons on short-pitch metal gratings. *Phys. Rev. B* **65**, (2002).

120. Ditlbacher, H., Krenn, J. R., Schider, G., Leitner, A. & Aussenegg, F. R. Two-dimensional optics with surface plasmon polaritons. *Appl. Phys. Lett.* **81**, 1762–1764 (2002).

121. Jin, J. M. *The Finite Element Method in Electromagnetics, 3rd edition*. (2014).

122. Green, M. A. Self-consistent optical parameters of intrinsic silicon at 300 K including temperature coefficients. *Sol. Energy Mater. Sol. Cells* **92**, 1305–1310 (2008).

123. Raut, H. K., Ganesh, V. A., Nair, A. S. & Ramakrishna, S. Anti-reflective coatings: A critical, in-depth review. *Energy and Environmental Science* **4**, 3779–3804 (2011).

124. McPeak, K. M. *et al.* Plasmonic films can easily be better: Rules and recipes. *ACS Photonics* **2**, 326–333 (2015).

125. Waterman, P. C. Matrix Formulation of Electromagnetic Scattering. *Proc. IEEE* **53**, 805–812 (1965).

126. Waterman, P. C. Symmetry, unitarity, and geometry in electromagnetic scattering. *Phys. Rev. D* **3**, 825–839 (1971).

127. Mishchenko, M. I., Travis, L. D., Lacis, A. A. & M. Mishchenko, L. Travis, A. L. *Scattering, Absorption and Emission of Light by Small Particles* (2002).

128. Zakharova, N. T., Videen, G. & Khlebtsov, N. G. Comprehensive T-matrix reference database: A 2009-2011 update. *J. Quant. Spectrosc. Radiat. Transf.* **113**, 1844–1852 (2012).

129. Palik, E. D. *Handbook of optical constants of solids* (2012).

130. Johnson, P. B. & Christy, R. W. Optical constants of the noble metals. *Phys. Rev. B* **6**, 4370–4379 (1972).

131. Nash, D. J. & Sambles, J. R. Surface plasmon-polariton study of the optical dielectric function of copper. *J. Mod. Opt.* **42**, 1639–1647 (1995).

132. Jiang, Y., Pillai, S. & Green, M. A. Re-evaluation of literature values of silver optical constants. *Opt. Express* **23**, 2133 (2015).

133. Jiang, Y., Pillai, S. & Green, M. A. Realistic Silver Optical Constants for Plasmonics. *Sci. Rep.* **6**, 30605 (2016).

134. Tompkins, H. G. & Irene, A. E. *Handbook of Ellipsometry* (2005).

135. Ebbesen, T. W., Lezec, H. J., Ghaemi, H. F., Thio, T. & Wolff, P. A. Extraordinary optical transmission through sub-wavelenght hole arrays. *Nature* **391**, 667–669 (1998).

136. Jackson, J. D. *Classical Electrodynamics, 3rd Edition* (1998).

137. Bethe, H. A. Theory of diffraction by small holes. *Phys. Rev.* **66**, 163–182 (1944).

138. Bouwkamp, C. J. On Bethe's theory of diffraction by small holes. *Philips Res. Reports* **5**, 321–332 (1950).

139. Bouwkamp, C. J. On the diffraction of electromagnetic waves by small circular disks and holes. *Philips Res. Reports* **5**, 401–422 (1950).

140. Lezec, H. J. *et al.* Beaming light from a subwavelength aperture. *Science* **297**, 820–822 (2002).

141. Van Der Molen, K. L. *et al.* Role of shape and localized resonances in extraordinary transmission through periodic arrays of subwavelength holes: Experiment and theory. *Phys. Rev. B - Condens. Matter Mater. Phys.* **72**, 1–9 (2005).

142. Coe, J. V., Heer, J. M., Teeters-Kennedy, S., Tian, H. & Rodriguez, K. R. Extraordinary Transmission of Metal Films with Arrays of Subwavelength Holes. *Annu. Rev. Phys. Chem.* **59**, 179–202 (2008).

143. Sobhani, A. *et al.* Narrowband photodetection in the near-infrared with a plasmon-induced hot electron device. *Nat. Commun.* **4**, 1643 (2013).

144. Jung, L. S., Campbell, C. T., Chinowsky, T. M., Mar, M. N. & Yee, S. S. Quantitative Interpretation of the Response of Surface Plasmon Resonance Sensors to Adsorbed Films. *Langmuir* **14**, 5636–5648 (1998).

145. de Bruijn, H. E., Altenburg, B. S. F., Kooyman, R. P. H. & Greve, J. Determination of thickness and dielectric constant of thin transparent dielectric layers using surface plasmon resonance. *Opt. Commun.* **82**, 425–432 (1991).

146. Saleh, B. E. A. & Teich, M. C. *Fundamentals of Photonics , 2nd Edition* (John Wiley & Sons, 2007).

147. Hessel, A. & Oliner, A. A. A New Theory of Wood's Anomalies on Optical Gratings. *Appl. Opt.* **4**, 1275 (1965).

148. Luk'Yanchuk, B. *et al.* The Fano resonance in plasmonic nanostructures and metamaterials. *Nat. Mater.* **9**, 707–715 (2010).

149. Inoue, D. *et al.* Polarization independent visible color filter comprising an aluminum film with surface-plasmon enhanced transmission through a subwavelength array of holes. *Appl. Phys. Lett.* **98**, (2011).

150. Shrestha, V. R., Lee, S. S., Kim, E. S. & Choi, D. Y. Aluminum plasmonics based highly transmissive polarization-independent subtractive color filters exploiting a nanopatch array. *Nano Lett.* **14**, 6672–6678 (2014).

151. Cheng, C.-W. *et al.* Wide-angle polarization independent infrared broadband absorbers based on metallic multi-sized disk arrays. *Opt. Express* **20**, 10376 (2012).

152. Lindquist, N. C., Luhman, W. A., Holmes, R. J. & Oh, S. H. Plasmonic nanocavity arrays for enhanced efficiency in organic photovoltaic cells. in *Conference Proceedings - Lasers and Electro-Optics Society Annual Meeting-LEOS* 413–414 (2008).

153. Ke, S., Wang, B. & Lu, P. Plasmonic absorption enhancement in

periodic cross-shaped graphene arrays. in *2015 IEEE MTT-S International Microwave Workshop Series on Advanced Materials and Processes for RF and THz Applications, IEEE MTT-S IMWS-AMP 2015 - Proceedings* (2015).

154. Feynman, R. There's plenty of room at the bottom. in *Feynman and Computation* (2018).

155. Newman, T. H. High resolution patterning system with a single bore objective lens. *J. Vac. Sci. Technol. B Microelectron. Nanom. Struct.* **5**, 88 (1987).

156. Scriven, L. E. Physics and Applications of DIP Coating and Spin Coating. *MRS Proc.* **121**, (1988).

157. Wiederrecht, G. *Handbook of Nanofabrication* (Academic Press, 2010).

158. Mattox, D. M. Vacuum Evaporation and Vacuum Deposition. in *Handbook of Physical Vapor Deposition (PVD) Processing* 288–342 (2009).

159. Frey, H. & Khan, H. R. *Handbook of Thin-Film Technology* (2015).

160. Pépin, A., Studer, V., Decanini, D. & Chen, Y. Exploring the high sensitivity of SU-8 resist for high resolution electron beam patterning. in *Microelectronic Engineering* **73–74**, 233–237 (2004).

161. Grigorescu, A. E., van der Krogt, M. C., Hagen, C. W. & Kruit, P. 10 nm lines and spaces written in HSQ, using electron beam lithography. *Microelectron. Eng.* **84**, 822–824 (2007).

162. Ma, S., Con, C., Yavuz, M. & Cui, B. Polystyrene negative resist for high-resolution electron beam lithography. *Nanoscale Res. Lett.* **6**, 1–6 (2011).

163. Foulds, I. G., Johnstone, R. W. & Parameswaran, M. Polydimethylglutarimide (PMGI) as a sacrificial material for SU-8 surface-micromachining. *J. Micromechanics Microengineering* **18**, (2008).

164. Golden, J., Miller, H., Nawrocki, D. & Ross, J. Optimization of Bi-layer Lift-Off Resist Process. in *CS MANTECH Conference* (2009).

165. McCullough, A. W., Vidusek, D. A., Legenza, M. W., de Grandpre, M. & Imhof, J. Polydimethylglutarimide (PMGI) Resist - A Progress Report. in *Advances in Resist Technology and Processing III* **0631**, 316 (2012).

166. Mao, A., Schaper, C. D. & Karlicek, R. F. Nanopatterning using a simple bi-layer lift-off process for the fabrication of a photonic crystal nanostructure. *Nanotechnology* **24**, (2013).

167. Naka, M., Kubo, M. & Okamoto, I. Wettability of silicon nitride by aluminium, copper and silver. *J. Mater. Sci. Lett.* **6**, 965–966 (1987).

168. Sexton, B. A., Feltis, B. N. & Davis, T. J. Characterisation of gold surface plasmon resonance sensor substrates. *Sensors Actuators, A Phys.* **141**, 471–475 (2008).

169. Habteyes, T. G. *et al.* Metallic adhesion layer induced plasmon damping and molecular linker as a nondamping alternative. *ACS Nano* **6**, 5702–5709 (2012).

170. Kim, W. M., Kim, S. H., Lee, K. S., Lee, T. S. & Kim, I. H. Titanium nitride thin film as an adhesion layer for surface plasmon resonance sensor chips. *Appl. Surf. Sci.* **261**, 749–752 (2012).

171. Chang, T. H. P. Proximity effect in electron-beam lithography. *J. Vac. Sci. Technol.* **12**, 1271–1275 (2002).

172. Kyser, D. F. & Viswanathan, N. S. Monte Carlo simulation of spatially distributed beams in electron-beam lithography. *J. Vac. Sci. Technol.* **12**, 1305–1308 (2002).

173. Kratschmer, E. Verification of a proximity effect correction program in electron-beam lithography. *J. Vac. Sci. Technol.* **19**, 1264–1268 (2002).

174. Kern, D. A novel approach to proximity effect correction. in *Proceedings of the Ninth International Conference on Electron and Ion Beam Science and Technology* (MO: Electrochemical Society, St. Luois, pp. 326-339, 1980).

175. Kane Yee. Numerical solution of initial boundary value problems involving maxwell's equations in isotropic media. *IEEE Trans. Antennas Propag.* **14**, 302–307 (1966).

176. Aspnes, D. E., Studna, A. A. & Kinsbron, E. Dielectric properties of heavily doped crystalline and amorphous silicon from 1.5 to 6.0 eV. *Phys. Rev. B* **29**, 768–779 (1984).

177. Marquier, F., Joulain, K., Mulet, J. P., Carminati, R. & Greffet, J. J. Engineering infrared emission properties of silicon in the near field and the far field. *Opt. Commun.* **237**, 379–388 (2004).

178. Chen, Y. B. & Zhang, Z. M. Heavily doped silicon complex gratings as wavelength-selective absorbing surfaces. *J. Phys. D. Appl. Phys.* **41**, (2008).

179. Basu, S., Lee, B. J. & Zhang, Z. M. Infrared Radiative Properties of Heavily Doped Silicon at Room Temperature. *J. Heat Transfer* **132**, 023301 (2009).

180. Miyao, M., Motooka, T., Natsuaki, N. & Tokuyama, T. Change of the electron effective mass in extremely heavily doped n-type Si obtained by ion implantation and laser annealing. *Solid State Commun.* **37**, 605–608 (1981).

181. Sy, H. K. & Ong, C. K. Electron mobility in heavily doped silicon. *Solid State Commun.* **52**, 881–883 (1984).

182. Denk, W., Strickler, J. H. & Webb, W. W. Two-photon laser scanning fluorescence microscopy. *Science (80-. ).* **248**, 73–76 (1990).

183. Zipfel, W. R., Williams, R. M. & Webb, W. W. Nonlinear magic: multiphoton microscopy in the biosciences. *Nat. Biotechnol.* **21**, 1369–77 (2003).

184. Göppert-Mayer, M. Über Elementarakte mit zwei Quantensprüngen. *Ann. Phys.* **401**, 273–294 (1931).

185. Centonze, V. E. & White, J. G. Multiphoton excitation provides optical sections from deeper within scattering specimens than confocal imaging. *Biophys. J.* **75**, 2015–2024 (1998).

186. Freund, I., Deutsch, M. & Sprecher, A. Connective tissue polarity. Optical second-harmonic microscopy, crossed-beam summation, and small-angle scattering in rat-tail tendon. *Biophys. J.* **50**, 693–712 (1986).

187. Guo, Y., Ho, P. P., Tirksliunas, A., Liu, F. & Alfano, R. R. Optical harmonic generation from animal tissues by the use of picosecond and femtosecond laser pulses. *Appl. Opt.* **35**, 6810–3 (1996).

188. Guo, Y. *et al.* Second-harmonic tomography of tissues. *Opt. Lett.* **23**, 733 (1998).

189. Débarre, D. *et al.* Imaging lipid bodies in cells and tissues using third-harmonic generation microscopy. *Nat. Methods* **3**, 47–53 (2006).

190. Watanabe, T. *et al.* Characterisation of the dynamic behaviour of lipid droplets in the early mouse embryo using adaptive harmonic generation microscopy. *BMC Cell Biol.* **11**, (2010).

191. Tserevelakis, G. J. *et al.* Label-free imaging of lipid depositions in C. elegans using third-harmonic generation microscopy. *PLoS One* **9**, (2014).

192. Aptel, F. *et al.* Multimodal nonlinear imaging of the human cornea. *Investig. Ophthalmol. Vis. Sci.* **51**, 2459–2465 (2010).

193. Rehberg, M., Krombach, F., Pohl, U. & Dietzel, S. Label-free 3D visualization of cellular and tissue structures in intact muscle with

second and third harmonic generation microscopy. *PLoS One* **6**, (2011).

194. Weigelin, B., Bakker, G.-J. & Friedl, P. Intravital third harmonic generation microscopy of collective melanoma cell invasion. *IntraVital* **1**, 32–43 (2012).

195. Friedl, P., Wolf, K., Harms, G. & von Andrian, U. H. Biological Second and Third Harmonic Generation Microscopy. in *Current Protocols in Cell Biology* (2007).

196. Valeur, B. & Berberan-Santos, M. N. *Molecular Fluorescence: Principles and Applications, Second Edition* (2012).

197. Plotnikov, S. V., Millard, A. C., Campagnola, P. J. & Mohler, W. A. Characterization of the myosin-based source for second-harmonic generation from muscle sarcomeres. *Biophys. J.* **90**, 693–703 (2006).

198. Nadiarnykh, O. & Campagnola, P. J. Retention of polarization signatures in SHG microscopy of scattering tissues through optical clearing. *Opt. Express* **17**, 5794 (2009).

199. Chen, X., Nadiarynkh, O., Plotnikov, S. & Campagnola, P. J. Second harmonic generation microscopy for quantitative analysis of collagen fibrillar structure. *Nat. Protoc.* **7**, 654–69 (2012).

200. Samim, M., Prent, N., Dicenzo, D., Stewart, B. & Barzda, V. Second harmonic generation polarization properties of myofilaments. *J. Biomed. Opt.* **19**, 056005 (2014).

201. Samim, M., Krouglov, S., James, D. F. & Barzda, V. Characterization of heterogeneous media using nonlinear Stokes–Mueller polarimetry. *J. Opt. Soc. Am. B* **33**, 2617 (2016).

202. Leutenegger, M., Eggeling, C. & Hell, S. W. Analytical description of STED microscopy performance. *Opt. Express* **18**, 26417–26429 (2010).

203. Galiani, S. *et al.* Strategies to maximize the performance of a STED microscope. *Opt. Express* **20**, 7362 (2012).

204. Rodriguez, P. F. G., Wu, Y., Singh, H. & Zhao, H. Building a fast scanning stimulated emission depletion microscope: a step by step guide. *Curr. Microsc. Contrib. to Adv. Sci. Technol.* 791–800 (2012).

205. Tønnesen, J., Nadrigny, F., Willig, K. I., Wedlich-Söldner, R. & Nägerl, U. V. Two-color STED microscopy of living synapses using a single laser-beam pair. *Biophys. J.* **101**, 2545–52 (2011).

206. Mahou, P. *et al.* Metrology of Multiphoton Microscopes Using Second Harmonic Generation Nanoprobes. *Small* **13**, (2017).

207. Denk, W., Piston, D. W. & Webb, W. W. Multi-photon molecular excitation in laser-scanning microscopy. in *Handbook of Biological Confocal Microscopy: Third Edition* (2006).

208. Bhattacharya, A. & Mahajan, R. L. Temperature dependence of thermal conductivity of biological tissues. *Physiol. Meas.* **24**, 769–83 (2003).

209. Sugiyama, M., Kanayama, H. & Akiyama, I. Measurement of volumetric heat capacity of biological tissues heated by ultrasound exposure. *J. Acoust. Soc. Am.* **140**, 3372–3372 (2016).

210. Zipfel, W. R. *et al.* Live tissue intrinsic emission microscopy using multiphoton-excited native fluorescence and second harmonic generation. *Proc. Natl. Acad. Sci.* **100**, 7075–7080 (2003).

211. Rothstein, E. C., Carroll, S., Combs, C. A., Jobsis, P. D. & Balaban, R. S. Skeletal muscle NAD(P)H two-photon fluorescence microscopy in vivo: Topology and optical inner filters. *Biophys. J.* **88**, 2165–2176 (2005).

212. Skala, M. C. *et al.* In vivo multiphoton fluorescence lifetime imaging of protein-bound and free nicotinamide adenine dinucleotide in normal and precancerous epithelia. *J. Biomed. Opt.* **12**, 024014 (2007).

213. Zhuo, S. *et al.* Label-free monitoring of colonic cancer progression using multiphoton microscopy. *Biomed. Opt. Express* **2**, 615 (2011).

214. Murphy, D. J. The biogenesis and functions of lipid bodies in animals, plants and microorganisms. *Progress in Lipid Research* **40**, 325–438 (2001).

215. Martin, S. & Parton, R. G. Caveolin, cholesterol, and lipid bodies. *Seminars in Cell and Developmental Biology* **16**, 163–174 (2005).

216. Pu, Y., Wang, W., Tang, G. & Alfano, R. R. Changes of collagen and nicotinamide adenine dinucleotide in human cancerous and normal prostate tissues studied using native fluorescence spectroscopy with selective excitation wavelength. *J. Biomed. Opt.* **15**, 049801 (2010).

217. Castaldi, A. *et al.* MicroRNA-133 modulates the β1-adrenergic receptor transduction cascade. *Circ. Res.* **115**, 273–283 (2014).

218. Milan, G. *et al.* Regulation of autophagy and the ubiquitin-proteasome system by the FoxO transcriptional network during muscle atrophy. *Nat. Commun.* **6**, (2015).

219. Spina, M. *et al.* Isolation of intact aortic valve scaffolds for heart-valve bioprostheses: Extracellular matrix structure, prevention from calcification, and cell repopulation features. *J. Biomed. Mater. Res. - Part A* **67**, 1338–1350 (2003).

220. Iop, L. *et al.* The influence of heart valve leaflet matrix characteristics on the interaction between human mesenchymal stem cells and decellularized scaffolds. *Biomaterials* **30**, 4104–4116 (2009).

221. Zhu, Y., Hu, X., Huang, Y., Yang, H. & Gong, Q. Fast and Low-Power All-Optical Tunable Fano Resonance in Plasmonic Microstructures. *Adv. Opt. Mater.* **1**, 61–67 (2013).

222. Christ, A., Tikhodeev, S. G., Gippius, N. A., Kuhl, J. & Giessen, H. Waveguide-plasmon polaritons: Strong coupling of photonic and electronic resonances in a metallic photonic crystal slab. *Phys. Rev. Lett.* **91**, 1–4 (2003).

223. Christ, A. *et al.* Optical properties of planar metallic photonic crystal structures: Experiment and theory. *Phys. Rev. B - Condens. Matter Mater. Phys.* **70**, 1–15 (2004).

224. Samim, M., Sandkuijl, D., Tretyakov, I., Cisek, R. & Barzda, V. Differential polarization nonlinear optical microscopy with adaptive optics controlled multiplexed beams. *Int. J. Mol. Sci.* **14**, 18520–18534 (2013).

225. Ghioni, M. *et al.* Resonant-cavity-enhanced single-photon avalanche diodes on reflecting silicon substrates. *IEEE Photonics Technol. Lett.* **20**, 413–415 (2008).

226. Ghioni, M. *et al.* Resonant-cavity-enhanced single photon avalanche diodes on double silicon-on-insulator substrates. *J. Mod. Opt.* **56**, 309–316 (2009).